Investigating Topological Properties of Floquet Quasi-One-Dimensional Systems

THESIS

Submitted in the partial fulfillment
of the requirement for the degree of

DOCTOR OF PHILOSOPHY

by

Aayushi Agrawal

ID No. 2017PHXF0415P

Under the supervision of

Prof. Jayendra Nath Bandyopadhyay

and

Co-supervision of

Prof. Tapomoy Guha Sarkar

BIRLA INSTITUTE OF TECHNOLOGY & SCIENCE, PILANI

2023

BIRLA INSTITUTE OF TECHNOLOGY & SCIENCE PILANI-333031 (RAJASTHAN) INDIA

CERTIFICATE

This is to certify that the thesis titled **"Investigating Topological Properties of Floquet Quasi-One-Dimensional Systems"**, submitted by **Aayushi Agrawal**, ID.No. **2017PHXF0415P** for the award of Ph.D. of the Institute embodies original work done by her under my supervision.

Signature of the Supervisor

. . . . . .

Dr. Jayendra Nath Bandyopadhyay

Professor

Department of Physics

BITS-Pilani, Pilani Campus.

Signature of the Co-Supervisor

. . . . . .

Dr. Tapomoy Guha Sarkar

Professor

Department of Physics

BITS-Pilani, Pilani Campus.

Date: . . . . . .

Dedicated to My Parents Mrs. Sita Agrawal and Mr. Dinesh Chandra Agrawal . . .

Acknowledgements

First and foremost, I express my gratitude to Prof. Jayendra Nath Bandyopadhyay, whose guidance, unwavering support, and encouragement have been invaluable throughout my research journey. Without his guidance and inspiration, this work would have been unattainable. My every discussin with him motivates me to remain dedicated and active in this field. I also want to offer my gratitude to my co-supervisior Prof. Tapomoy Guha Sarkar for his insightful discussion.

I extend special gratitude to Khushboo, She is a special kind of topological invariant that remains same irrespective whether the contour of my life undergoes some continous or discontinuous deformation. She never hesitates to stand by my side.

I also thank my Floquet group members Rashmi, Shaina, Srinidhi and Harshita. I really enjoyed all the formal and informal long discussions with all of you.

I would like to thank my entire football team for the for the exhilarating and stress-relieving games, as well as the enjoyable tea time moments. I want to thank all my Lab members, friends, and all my seniors in the Physics Department friends Pradeep, Arghya, Shivani, Nikita, Ram, Shiva, Shital, Shweta, CC and Nikhil.

I would like to offer special gratitude to the members of my Doctoral Advisory Committee, Prof. Biswanath Layek and Prof. Amol R. Holkundkar, for their support, and suggestions during the progress review and to review my draft thesis. I sincerely thank Prof. Rakesh Choubisa, Head of Department and Prof. ManjulaDevi V as DRC Convener, for their persistent support. Also, I wish to express my gratitude to all the past HODs, DRC conveners, and faculty members of the physics department for their kind support time-to-time. The technical staff of the department, Rajeev Ji, Srikant Ji & Kundan are also gratefully thanked for their help.

I would humbly express my regards to the Vice-Chancellor, Director and Deans of Birla Institute of Technology & Science (BITS), Pilani for providing me with the opportunity to pursue my doctoral studies by providing necessary facilities and financial support. I am also grateful to DST-SERB for providing funding during the initial two years of this endeavor.

I express my gratitude to all the present and past Deans and Associate Deans of AGSRD for their constant official support in organizing my research work. All other staff members of AGSRD are also gratefully thanked for their help.

Last but not least, I would like to thank my father Dinesh Chandra, my mother Sita Agrawal, my brother Aman and my sister Tarushi for their encouragement, continuous support and immense love. Without their love and support, this journey would not be possible.

Aayushi Agrawal . . .

Abstract

Photonics plays a pivotal role in advancing the field of topological insulators by enabling the synthetic preperation of these materials, which may not exist naturally. The quasi-one-dimesioanl (quasi-1D) systems which can be fabricated through photonics can show more exotic propeties in the presence of a time-dependent periodic driving. These periodically driven systems are studied within the Floquet framework. The Floquet formalism influences the static system by breaking certain system's symmetries and induces new topological propeties in the static systems. This thesis emphasizes on the theoretical study of quasi-1D systems formed via the simplest 1D topological insulator, Su-Schrieffer-Heeger model (SSH).

In the beginning of the thesis, we provide an introduction to topology, topological insulators, their applications and the quasi-1D model followed by the methodology to calculate the effective Hamiltonian and topological invariants. In this thesis, we analyzed two different quasi-1D models. The first quasi-1D model is called the extended SSH model or E-SSH model, where all the hopping amplitudes of the SSH chain along with the next nearest neighbor hopping are modulated by a cyclic parameter. This cyclic parameter is considered as a synthetic dimension, and the E-SSH model is treated as a two-dimensional model; hence the Chern number is the topological invariant to determine the topological phases. We study this model by applying a continuous sinusoidal driving both in the nearest neighbor and the next nearest neighbor and compute the effective Hamiltonian using the Floquet replica method. The Floquet E-SSH model is cherished by the topological phases with the high Chern number.

Then, we study another quasi-1D model which is constructed by arranging SSH chains in the y-direction and becomes a 2D weak topological insulator. The E-SSH model can be turned into the stacked geometry by promoting the cyclic parameter to another actual momentum. We allow hopping so that this N stacked SSH model preserves all three

fundamental symmetries (chiral, time-reversal and particle-hole). For this undriven model, we catalog the topological phases by systematic breaking of these symmetries where breaking of the symmetries in the system is introduced by allowing different hopping in the system.

This is followed by a study of the periodically driven N stacked SSH model. We use circularly polarized light as a time-dependent periodic drive. Again, we use the Floquet replica method to derive the effective Hamiltonian. In the presence of driving, this model also exhibits the topological phases with the high Chern number. The role of the linearly polarized light along $x-$ and y-directions are also investigated. We also study this model with an elliptical periodic drive. Finally, we conclude this thesis with a summary and some future directions.

Preface

About the thesis

This thesis presents a study on the exotic topological properties of quasi-1D systems. The quasi-1D systems which are constructed from the 1D topological insulators. The new topological properties can be induced in the system either via breaking some of the system symmetries or by applying an external time-dependent periodic driving which eventually leads to the breaking of the system's symmetries. The time-dependent periodically driven systems are known as Floquet systems. The Floquet formalism is a theoretical framework to compute the effective Hamiltonian which is a time-independent Hamiltonian. The trade-off to obtain this time-independent Hamiltonian is that now one has to solve an infinite dimensional matrix. The Floquet replical method facilitates us to work in high frequency regime as well as in the low frequency regime. We choose quasi-1D model beacuse only a few investigations has been done on these models. This thesis presents two quasi-1D models : extended Su-Schrieffer-Heeger (E-SSH) and N stacked SSH model. The first model E-SSH model is constructed by modulating all the nearest neighbor and next nearest neighbor hopping amplitudes by a cyclic parameter which plays the role of another but synthetic dimension. This thesis studied the E-SSH model with a continous sinusoidal driving. In this study, we obtain exotic Floquet topological phases with the high Chern number. The other model, N stacked SSH model is constructed by stacking N number of SSH chains in the vertical direction. This model is studied by systematic breaking of symmetries and by application of a laser field of the form circularly polarized light. The first study focuses on how topological phases are affected with the systematic breaking of the symmetries. The latter study reveals the effect of the laser field of the form circularly and linearly polarized light on the topological phases of the N stacked SSH model. This thesis also includes the effect of elliptical polarized light on the N stacked SSH model that clarifies which

phase angle of the laser field can induce more exotic topological properties for this model.

To the reader

This thesis will hopefully provide an overview to prepare a system with rich topological properties. This thesis shines light on the theoretical study of Floquet topological insulators. Those who are attracted to the field of Qunatum Hall effect, topology will like to hold this thesis. The area of the research of this thesis is theoretical condensed matter physics.

Thesis Outline

Thesis consists of seven Chapters. The first Chapter includes the introduction and motivation behind this thesis work. The second Chapter has all the mathematical tools which are further used in the thesis. The last four Chapters discuss different results of the thesis. This thesis is organized as follows :

- In Chapter 1, an introductory part with the qualitative discussion of an overview of the topological insulators, their properties, classification of the topological insulators, quasi-1D systems. A discussion on the motivation behind this thesis work is also presented in this Chapter.

- In Chapter 2, mathematical framework for all the formulation and methods are presented. It includes a mathematical description on the topology, topological invariants, 1D topological insulator : SSH model and the Floquet formalism with the Floquet replica method and perturbative schemes.

- In Chapter 3, Floquet topological phases with the high Chern number of the periodically driven E-SSH model is discussed. This Chapter use the monochromatic continous sinusoidal driving. A detailed analysis is also shown for the topological phases with the high Chern number.

- In Chapter 4, another quasi-1D model and 2D weak topological insulator, called N stacked SSH model is studied. This Chapter cataloges all the topological phases of this model by systematic breaking of the symmetries. This Chapter is divided into three parts. In the first part, the model is discussed by preserving all three fundamental symmetries. In the second part, the model is studied with the broken chiral symmetry and in the third part, models with broken chiral and time-reversal symmetry are studied. Finally, it discusses a interplay between the broken particle hole and inversion symmetry which exhibits a topological phase transition.

- In Chapter 5, the model discussed in the previous Chapter is analysed with the application of a periodically driving. This study shows the emergence of the laser indduced Floquet topological phases with the high Chern number. This Chapter also includes an investigation after applying linearly polarized light on the N stacked SSH model.

- In Chapter 6, again the N stacked SSH model is investigated but in the presence of elliptical polarized light. This study clarifies which laser field is more efficient to prepare a 2D weak topological insulator with rich topological phases.

- Chapter 7, sheds light on the final remarks of this thesis. This Chapter also includes some of the future directions related to this thesis work.

Contents

List of Figures

List of Tables

List of Symbols

$\bar{\Omega}$	Gaussian curvature
g	genus
χ	Euler characteristics
H_{SSH}	Hamiltonian of the SSH chain
$c^{\dagger}_{A,n}\ c_{B,n}$	creation and annihilation operator in real space on one-dimensional chain
$c^{\dagger}_{A,k}\ c_{B,k}$	creation and annihilation operator in momentum space on one-dimensional chain
$\sigma_x,\ \sigma_y,\ \sigma_z$	Pauli spin matrix
$\mathcal{H}(k)$	Recciprocal space Hamiltonian
C	Chiral symmetry operator
$\mathcal{P}$	Particle-hole symmetry operator
$\mathcal{T}$	Time-reversal symmetry operator
C	Chern number
w	Winding number
$\|u_n(t)\rangle$	Floquet modes
$\|\psi_n(t)\rangle$	Floquet states
$U(t_0, t_0+T)$	Floquet time-evolution operator
ϵ_n	Quasi energy
$\mathcal{H}_F$	Flqouet Hamiltonian
H_m	Fourier component
H_0	Undriven Hamiltonian
H^{vV}_{eff}	van Vlech effcetive Hamiltonian
$\Omega,\ \omega$	Driving frequency

H_{E-SSH}	Hamiltonian of the E-SSH model
$\mathcal{F}$	Berry curvature
$A_{k/\theta}$	Berry connections
Z_k	2D Zak phase
$\mathbb{H}$	Hibert space
$\mathbb{T}$	space of square integarble time-periodic functions
H_{N-SSH}	Hamiltonian of the N stacked SSH model

List of Abbreviations

IQHE	**I**nteger **Q**uantum **H**all **E**ffect
QSH	**Q**uantum **S**pin **H**all
TI	**T**opological **I**nsulator
NNN	**N**ext **N**earest **N**eighbor
TR	**T**ime **R**eversal
SSH	**S**u-**S**chrieffer-**H**eeger
PH	**P**article **H**ole
FTI	**F**loquet **T**opological **I**nsulator
E-SSH	**E**xtenede **S**u-**S**chrieffer-**H**eeger
WTI	**W**eak **T**opological **I**nsulator
BZ	**B**rillouin **Z**one
TDSE	**T**ime **D**ependent **S**chr*ö*dinger **E**quation
vV	**v**an **V**lech
BW	**B**rillouin **W**igner
QAH	**Q**uantum **A**nomalous **H**all
TSM	**T**opological **S**emi **M**etal
TCI	**T**opological **C**rystalline **I**nsulator
CPL	**C**ircularly **P**olarized **L**ight
LPL	**L**inearly **P**olarized **L**ight
EPL	**E**llipticaly **P**olarized **L**ight
FBZ	**F**loquet **B**rillouin **Z**one

1

Introduction

1.1 Historical background of topology in condensed matter physics

Topology is a branch of mathematics that has recently found immense applications in condensed matter physics. Notably, its application in studying a class of materials known as topological insulators (TIs) is very important. The TIs are a promising class of materials that have the potential for different technological applications because they allow current to flow without dissipation at the edges (in 2D materials) and at the surfaces (in 3D materials), keeping the bulk part insulating [1–4]. Historically, topology was first applied in condensed matter physics when von Klitzing discovered the so-called quantum Hall effect (QHE) in 1989 [5]. The classical version of the Hall effect, or simply the Hall effect, has been known to humanity for a long time when, in 1879, Edwin H. Hall discovered that a magnetic field applied perpendicular to the direction of a current flow through an electrical conductor generates a potential difference, known as the Hall

voltage, transverse to the current flow as well as the direction of the applied magnetic field. On the other hand, in the case of the QHE, von Klitzing observed that the Hall conductivity (ratio of the Hall voltage and the applied current) got quantized in the units of fundamental constants e^2/h when electrons are flowing in a 2D sample at very low temperature and in the presence of strong magnetic field where e is the charge of an electron and h is the Planck's constant. The quantized transverse Hall conductivity is defined as follows:

$$\sigma_{xy} = C\frac{e^2}{h}.$$

It was observed that the Hall conductivity σ_{xy} shows multiple plateaus when plotted as a function of the magnetic field. Moreover, when σ_{xy} jumps from one plateau to another one, the longitudinal Hall conductivity σ_{xx} shows peaks.

Since the discovery of the QHE, a mathematical formulation for the quantization of the Hall conductivity has been proposed by Thouless, Kohmoto, Nightingale, and den Nijs, and they connected this quantization with a topological invariant, which is now known as the TKNN invariant [6]. Later, in 1983, a connection between the TKNN invariant and Chern number was identified and found that essentially they refer to the same topological invariant [7–10]. Mathematically, the topological invariant is an integer that remains the same for a particular topological phase. In topology, two objects are called topologically equivalent if one can get an object from another by a continuous deformation without cutting or stitching. During this continuous deformation, the topological phase of the objects remains unchanged, and the topological invariant identifies this. In condensed matter, two materials are considered topologically equivalent if one gets the energy bands of one material from the other by continuous variation of a system parameter without closing or opening any energy bands [11].

After von Klitzing's discovery of the QHE, Haldane proposed a model that exhibits the QHE-like behavior without any external magnetic field [12]. In this model, Haldane

introduced a complex next-nearest neighbor (NNN) hopping term in a graphene-like hexagonal lattice, simulating a magnetic field-like effect in the system. Like the magnetic field, NNN hopping also breaks the time-reversal (TR) symmetry and exhibits topological phases with nonzero Chern numbers. The next question was how to generate topological systems with TR symmetry preserved. A new kind of Hall effect was proposed, called the quantum spin Hall effect (QSHE). The QSHE was observed in a single layer of graphene with spin-orbit interaction term [13, 14]. In the QSH systems, the TR symmetry is preserved, and the spin-orbit interaction term generates a magnetic field-like effect. The chiral edge modes are again along the opposite directions and related to a particular spin. In the following section, we unveil the utilization and categorization of the TIs, followed by a motivation for this thesis.

1.2 Properties and applications of TIs

Topological insulators (TIs) [15–18] are intriguing semiconductor materials with wide technological applications in photonics [19], quantum computers, spintronics [20], topological electronics [21], etc. The TIs are an interesting class of materials, because these harbor following exotic properties: [22–38]. These properties are as follows

Low power dissipation: Unlike ordinary insulators with an energy band gap in the bulk, a distinct feature of the TIs is the presence of edge states in the gap that connect the valence and conduction bands. This allows electronic charges to flow along the edges or surfaces. The flow of electrons surpasses any defects in the crystal and continue their flow along the edges or surfaces. In the TIs, there is no backscattering which makes them the materials with low-power dissipation.

Topological protection of electronic states: In condensed matter, electronic states are topologically protected means that these states are immune to a perturbation that is respecting the symmetry responsible for the topological nature of the system. The

topological property of a system is measured by topological invariants like winding number, Chern numbers, etc. These invariants are calculated from the energy bands of the system. The stability of the electronic states of the topological materials have made them an ideal candidate for realizing quantum computers.

Thermoelectrical properties: The TIs are also suitable materials that exhibit thermoelectric properties. The efficiency of a thermoelectric material is given as $ZT = \frac{S^2\sigma}{\kappa}T$, where S, σ, κ, and T refer to the thermoelectric power, thermal conductivity, electric conductivity, and temperature, respectively. The main difficulty in preparing these materials is synchronizing all these strongly correlated variables. One advantage of using TIs in thermoelectric devices is that they are composed of heavy elements like Bi, Sb, and Pb, which reduce the thermal conductivity in the system. Additionally, in TIs, the electrons move on the surface even after inducing crystal defects without backscattering. Therefore, introducing many defects in a TI reduces the thermal conductivity and increases the material's electric conductivity, making it an ideal material for thermoelectric devices.

QSH state: A remarkable discovery of QSHE triggered a possibility for the TIs to be used in spintronics, the short form of "spin transport electronics". Spintronics is similar to electronics; however, it uses the intrinsic spin of electrons rather than its charge for storing and transferring information. In the QSHE, the electron spin is separated from its charge. This property is exploited in spintronics to create spin-current, which has applications in magnetic memory devices and spin-based logic gates.

1.3 Classification of topological insulators

The TIs are classified according to their dimensions and the symmetries preserved in any system. Accordingly, the TIs are classified into ten different categories and developed a periodic table for the TIs [39, 40].

Classification according to dimensions: The 2D TIs were discovered after the remarkable discovery of IQHE and QSHE, along with the phenomenal discovery of the Haldane model. The 2D and 3D TIs attracted much more attention from the community when graphene, a natural 2D TI, was extracted from bulk graphite [41]. However, extensive theoretical and experimental work has already been done on it, where some extensions to 3D have also been considered. The 3D TIs are also studied extensively [42, 43]. On the other hand, the lowest dimensional TI was added to the list of TIs when conducting properties were observed in a polyacetylene chain with doping [44, 45]. This polymer was subsequently modeled by Su-Schrieffer-Heeger (SSH) through a tight-binding Hamiltonian, leading to an eventual observation of topological properties [46]. A detailed explanation of this model of the 1D chain is provided in the next Chapter. This thesis studied different models in different contexts, but all these models comprise the SSH chains.

Classification according to symmetries : A TI can have following three fundamental symmetries

$$\mathcal{C}^{-1}\,\mathcal{H}(k)\,\mathcal{C} = -\mathcal{H}(k)$$

$$\mathcal{P}^{-1}\,\mathcal{H}(k)\,\mathcal{P} = -\mathcal{H}(-k)$$

$$\mathcal{T}^{-1}\,\mathcal{H}(k)\,\mathcal{T} = \mathcal{H}(-k)$$

Here, $\mathcal{C}$, $\mathcal{P}$, and $\mathcal{T}$ are chiral, particle-hole and time-reversal symmetries. Only the 1D TIs have the privilege to follow all three symmetries. In the periodic table, depending upon the symmetries and dimension, different topological invariants are defined as a measure of the topological phases as shown in 1.1. Recent studies have also attracted towards the quasi-1D and 2D systems which are engineered from the 1D and 2D systems. After the discovery of graphene and bilayer graphene, quasi-2D systems formed via stacking of graphene have been studied extensively [47–49]. However, quasi-1D systems

		TRS	PHS	CS	$d=1$	$d=2$	$d=3$
Standard Wigner-Dyson	A (Unitary)	0	0	0	–	$\mathcal{Z}$	–
	AI (Orthogonal)	+1	0	0	–	–	–
	AII (Sympletic)	−1	0	0	–	$\mathcal{Z}_2$	$\mathcal{Z}_2$
Chiral Sublattice	AIII (Chiral unitary)	0	0	+1	$\mathcal{Z}$	–	$\mathcal{Z}$
	BDI (Chiral orthogonal)	+1	+1	1	$\mathcal{Z}$	–	–
	CII (Chiral Sympletic)	−1	−1	1	$\mathcal{Z}$	–	$\mathcal{Z}_2$
BdG	D	0	+1	0	–	$\mathcal{Z}$	–
	C	0	−1	0	$\mathcal{Z}$	–	–
	DIII	−1	+1	1	$\mathcal{Z}_2$	$\mathcal{Z}_2$	$\mathcal{Z}_2$
	CI	+1	−1	1	–	–	$\mathcal{Z}$

TABLE 1.1: Periodic table for topological insulators and superconductors. This table is taken from the reference [39].

are still an unexplored area which we discuss extensively in the next section.

1.4 Quasi-1D topological insulators

We consistently search for an appropriate model that exhibits robust topological properties while minimizing the number of degrees of freedom. In this thesis, we study various quasi-1D systems and their associated topological properties. The quasi-1D systems are generated from the modified 1D topological insulator (TI). The SSH model is a well-known and the simplest 1D toy model of TI. As a theoretician, we select this simplest model and lay a roadmap to engineer systems with new topological properties. On the way, different techniques are used to introduce new topological properties in the system. An extensive study of quantum Hall systems, the Haldane model, and quantum spin Hall systems has opened a research direction to induce new topological phases by breaking or preserving symmetries in a given system. On the other hand, external driving can also be applied to a system to break some of its symmetries and introduce exotic topological

properties. Most studies focus on the 1D, 2D, and 3D TIs, but quasi-1D TIs attracted much less attention.

This thesis focuses on two different quasi-1D TI models. First, we consider an extended SSH or E-SSH model. This model is a 1D SSH chain with an additional NNN hopping term, where a cyclic parameter modulates all the hopping terms. This cyclic parameter plays the role of an additional synthetic dimension. The second model is constructed by promoting the synthetic dimension to an actual one. Specifically, these models are constructed by stacking N number of SSH chains. This layered structure forms a weak TI with even number of Dirac points. The quasi-1D TIs are not found naturally but can be simulated in photonic systems. We discuss these models rigorously in Chapters 3-6. In order to make these systems topologically exotic, we also study these models under time-periodic driving.

1.5 Floquet topological insulators

Periodically driven systems are studied under Flqouet theory, and therefore, these systems are known as Floquet systems. Similarly, when periodic driving induces topological property in a system by breaking its underlying symmetries, it is called a Floquet topological insulator (FTI) [50, 51]. In any undriven system, nontrivial topology is studied using energies and spatially periodic Bloch states. However, in the FTIs, along with spatial periodicity, the system also has time-periodicity, and thus, it becomes a temporal analog of Bloch systems. In the FTIs, the external driving introduces additional parameters like driving amplitude, frequency, and phase, which can be tuned to induce a new desired topological phase in a given system.

The Schrödinger equation with time-periodic Hamiltonian is solved by the Floquet theory. Following this theory, the time-periodic Hamiltonian becomes time-independent when expressed in the frequency space by Fourier transformation. A trade-off to obtain

the time-independent Hamiltonian is that one has to solve an infinite dimensional matrix, which we have discussed extensively in the next Chapter. Since periodic driving can break various symmetries in a system, the FTIs have the potential to host exotic topological properties, which may not be possible to achieve by any static drive. In the last few years, the FTIs in 1D, 2D, and 3D have been studied extensively, and remarkable nontrivial topological properties have been observed. Recently, experimentalists have found that the FTIs can be realized in photonic systems, known as photonic topological insulators [19].

In this thesis, my main focus is to study the quasi-1D systems with an external time-periodic driving which is discussed in detail in the upcoming Chapters.

1.6 Motivation

Over the past four decades, the topological insulator research area predominantly revolved around exploring various 2D and 3D TIs, but much less attention has been paid to the quasi-1D systems. These systems are 2D but engineered by stacking many 1D systems. The primary objective of this thesis is to investigate the quasi-1D TIs and scrutinize their distinct topological features. We study two kinds of quasi-1D TIs: the extended SSH model (E-SSH) and the N stacked SSH model. Both models are constructed from the 1D SSH model. This low-dimensional system exhibits the Haldane model-like phase diagram, which is a primary motivation behind selecting the E-SSH model for our study. Next, we consider a 2D weak topological insulator (WTI) engineered by stacking N number of SSH chains. This model can induce various topological phases by tuning intra and inter-chain hopping terms. Moreover, periodic driving has also been used to induce nontrivial topology in the N stacked SSH chains with all the symmetries preserved.

1.7 Organization of the thesis

This thesis contains seven Chapters, including the introduction. A brief description of these systems as follows:

Chapter 2 : In this Chapter, we discuss all the mathematical tools and formalism used in the later Chapters to derive the effective Hamiltonian and different topological invariants. We discuss the derivation of Floquet formalism and its formulations in Physics. We provide a theoretical discussion on topology, Berry phase, and topological invariants.

Chapter 3 : We investigate the periodically driven E-SSH model and observe the Floquet topological phases with the high Chern number. The E-SSH model is a 1D SSH model with nearest neighbor and NNN hopping. The hopping amplitudes are modulated by a cyclic parameter θ where this parameter θ plays the role of another synthetic dimension. The topological properties are defined by calculating the Chern number. Studies found that the low-dimensional E-SSH model possesses the same phase diagram as the Haldane model. We use sinusoidal driving as the periodic drive in NN and NNN hopping amplitudes. Under this periodic driving, we study the driven E-SSH model in the high-frequency regime as well as in the low-frequency regime. The Floquet replica method facilitates our exploration of both frequency regimes.

Chapter 4 : We study a 2D weak topological insulator constructed by stacking N number of SSH chains along the y-direction which has even number of Dirac points with edge modes along the direction of stacking. We catalog the various topological properties of the N-stacked SSH model by systematically breaking the symmetries. We construct a N stacked SSH model such that it preserves all three fundamental symmetries (chiral, TR, and PH) and named the "basic model". This basic model has topological properties with $C = 0$ and a non-zero quantized 2D Zak phase. Then, we break chiral symmetry in the system by adding A (or B) to A (or B), hopping with equal and opposite real amplitude. This model again shows zero Chern number and nontriviality is defined by non-zero

fractionalized Zak phase. Finally, we study the basic model with the breaking of chiral and TR symmetry by replacing real A (or B) to A (or B) hopping amplitudes with the imaginary hopping amplitudes. Breaking chiral and TR symmetries is essential for this N stacked SSH model to be a Chern insulator. Initially, we preserve the PH symmetry, which allows us to calculate the Chern number analytically. Using the analytical expression of the Chern number, we also show a Phase diagram. Later, we also show an interplay between the breaking of PH and inversion symmetry, which leads to a topological phase transition with the Chern number $C = \pm 1$.

Chapter 5 : We study Floquet version of N stacked SSH model. We shine the circularly polarized laser light (CPL) on the basic model. Here again, we use the Floquet replica method to calculate the effective Hamiltonian. The CPL breaks the system's TR symmetry and converts the basic model into a Chern insulator. Here, we obtain topological phases with a high Chern number in the low-frequency regime and topological phases with $C = \pm 1$ in the high-frequency regime.

Chapter 6 : In this Chapter, we study the N stacked SSH model with elliptically polarized light. Since, in the weak topological insulators, edge states can exhibit along the direction of stacking. However, for the undriven system, we found that the system breaks the chiral and TR symmetry; it exhibits edge states in both directions and behaves the same as an actual 2D model. Therefore, we investigate the effect of coupling in the N stacked SSH.

Chapter 7 : Finally, we conclude the thesis with a short discussion about the probable future directions.

2

Mathematical tools

This Chapter discusses the basic mathematical formulations which are used in this thesis.

2.1 Topology

The term topology often describes the contours of a surface or the shape of a crystal. Fundamentally, topology is a branch of mathematics that studies the objects (manifolds in the topology) that retain the same topological properties only if these objects can be transformed into each other through some continuous deformation. Independent of the geometry of an object, topology defines the global properties of the object. In this section, we provide a mathematical overview of topology.

A topological space is defined as an ordered pair (S, U) of two sets S and U, where U is a collection of the subsets of S, and the set U satisfies

1. the empty set $\emptyset$ is in U, i.e., $\emptyset \in U$,

2. the set S is in U, i.e., $S \in U$,

3. the union of any two elements of u_i and u_j of U such that $(u_i \cup u_j) \in U$,

4. the intersection of any two elements u_i and u_j of U such that $(u_i \cap u_j) \in U$,

then U is called a topology on S. This definition can be understood by a simple illustrative example. Consider a set $S = \{\text{Ball, Racket, Shuttle}\}$. Then the set $U = \{\emptyset, S, \{\text{Ball}\}\}$ will be topological. However, the set $U = \{\emptyset, S, \{\text{Ball}\}, \{\text{Shuttle}\}, \{\text{Racket, Shuttle}\}\}$ will not be topological because the union of $\{\text{Ball}\}$ and $\{\text{Shuttle}\}$ is not an element of U.

2.2 Topological invariants

We now discuss some important theorems to understand topological invariants and how these characterize a topological phase.

Gauss-Bonnet theorem: This theorem establishes a relationship to understand the interplay between geometry and topology. For any closed surface, the Gauss-Bonnet theorem defines

$$\frac{1}{2\pi}\int_s d\sigma\bar{\Omega} = 2(1-g), \tag{2.1}$$

where Ω represents the Gaussian curvature and g is a positive integer called "genus" of the surface. For example, the sphere is the surface with genus $g = 0$. Similarly, objects with one hole such as coffee mug and doughnuts have genus $g = 1$, and an object with two holes has $g = 2$ and so on. This theorem is important because it links the curvature of a surface to the topology which is given by "Euler characteristics". The Euler characteristics are determined by the following equation

$$\chi = V - E + F,$$

where V is the number of vertices, E is the number of edges, and F is the number of faces. The Euler characteristic is an integer and a topological invariant. Now, to understand how

this topological invariant changes in the system, one needs to understand the adiabatic theorem.

Adiabatic theorem: This theorem states that when a system is under a small continuous deformation, then the eigenstate of the system before and after the deformation remains identical. A system is continuously deformed into another system, provided

- the parameters are changed continuously and preserve all the symmetries,
- the band gap does not close during the transformation.

To compute the path of the revolving eigenstate under a continuous deformation, a mathematical formulation is described below.

Berry phase and Berry curvature: The Berry phase, also known as Berry's phase or geometric phase, is a concept in quantum mechanics that describes a phase shift acquired by the quantum state of a system when subjected to adiabatic (slow and continuous) changes in its parameters. Sir Michael Berry introduced this concept in 1984, and it has since become an important topic in quantum physics, condensed matter physics, and other areas of theoretical physics [52]. Pancharatnam introduced a similar geometrical phase in the context of optics [53]. In solid-state physics, the Berry phase is defined as a global phase acquired by an eigenstate when it traces the Brillouin zone (BZ) under some continuous deformation. The Berry phase is a geometric phase because it depends on the path followed by the system's Hamiltonian, or eigenstate. It does not depend on the complete details of the geometry.

We now formally define the Berry phase. Consider a quantum system with the Hamiltonian $H(\boldsymbol{R})$ depending on the parameters $\boldsymbol{R}$. These parameters vary adiabatically with time as $\boldsymbol{R} \equiv \boldsymbol{R}(t)$. The corresponding Schrödinger equation is

$$H(\boldsymbol{R})|\psi(t)\rangle = i\frac{d}{dt}|\psi(t)\rangle$$

and

$$H(\boldsymbol{R})|n,\boldsymbol{R}\rangle = E_n(\boldsymbol{R})|n,\boldsymbol{R}\rangle,$$

where $E_n(\boldsymbol{R})$ is the energy of the n^{th} eigenstate. For a closed loop, the Berry phase is defined as

$$\phi_n = \int_c A_n(\boldsymbol{R}) \cdot d\boldsymbol{R}, \tag{2.2}$$

where Berry's connection $A(\boldsymbol{R})$ is defined as

$$A_n(\boldsymbol{R}) = i\langle n,\boldsymbol{R}|\nabla_{\boldsymbol{R}}|n,\boldsymbol{R}\rangle. \tag{2.3}$$

Below, we show that the above inner product is a pure imaginary quantity:

$$\mathrm{Re}\,\langle n,\boldsymbol{R}|\nabla_{\boldsymbol{R}}|n,\boldsymbol{R}\rangle = \frac{1}{2}\left[\langle n,\boldsymbol{R}|\Big(\nabla_{\boldsymbol{R}}|n,\boldsymbol{R}\rangle\Big) + \Big(\nabla_{\boldsymbol{R}}\langle n,\boldsymbol{R}|\Big)|n,\boldsymbol{R}\rangle\right] = \nabla_{\boldsymbol{R}}\langle n,\boldsymbol{R}|n,\boldsymbol{R}\rangle = 0.$$

This result shows that Berry's connection and Berry's phase are real quantities, which is expected.

In this thesis, we use two different topological invariants: the winding number (w) and the Chern number (C). The basic difference between these two topological invariants is that the first one characterizes the topological properties of the 1D systems, while the latter one is used for characterizing the 2D systems. The winding number is defined as the number of times the phase wraps around the origin as the system parameters vary within the BZ. This topological invariant is calculated from the following formula:

$$w = \frac{1}{2\pi i}\int_{BZ} dk \frac{d}{dk}\log h(k). \tag{2.4}$$

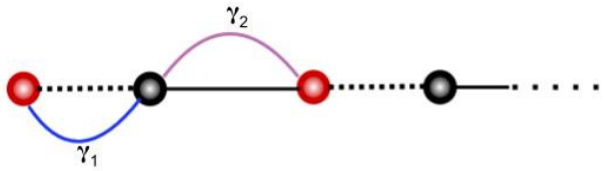

FIGURE 2.1: A schematic diagram of 1D SSH chain. Here, A and B sublattices are shown by red and black solid circles. The intra-cell hopping γ_1 is shown by blue color, whereas the intercell hopping γ_2 is shown by magenta color.

The Chern number C is calculated by integrating the Berry curvature over the first BZ, a closed 2D manifold, as:

$$C = \frac{1}{2\pi} \int_{BZ} \mathcal{F}(k_x, k_y)\, dk_x\, dk_y, \tag{2.5}$$

where the Berry curvature

$$\mathcal{F}(k_x, k_y) = \partial_{k_y} A_{k_x} - \partial_{k_x} A_{k_y}$$

and

$$A_{k_{x/y}} \equiv \langle \psi(k_x, k_y) | \partial_{k_{x/y}} | \psi(k_x, k_y) \rangle$$

are Berry's connections [52]. Here, the state $|\psi(k_x, k_y)\rangle$ is Bloch's function.

2.3 One dimensional topological insulator: Su-Schrieffer-Heeger (SSH) model

The Su-Schrieffer-Heeger (SSH) chain is an extensively studied model for a one-dimensional topological insulator. This model was first proposed to study the electrical conductivity in a polyacetylene chain, which is a polymer consisting of alternate single and double carbon bonds [54, 55]. Later, the conducting properties of the polyacetylene chain were explained through a tight binding Hamiltonian [44, 45]. The alternate single

and double carbon bonds in the polymer chain are mimicked in the tight-binding model by introducing two distinct nearest-neighbor (NN) hopping terms. Consequently, the 1D chain can be thought of as a combination of two sublattices A and B. Alternatively, one can consider that two atoms are present in every unit cell of this tight-binding model. Thus the Hamiltonian of the SSH chain can be expressed as:

$$H_{SSH} = \sum_{n} \left[\gamma_1 \, c^{\dagger}_{A,n} \, c_{B,n} \, + \gamma_2 \, c^{\dagger}_{A,n+1} \, c_{B,n} \right]. \tag{2.6}$$

Here, the parameters γ_1 and γ_2 are the NN hopping amplitudes, where γ_1 represents the strength of the intracell hopping between A to B; whereas γ_2 is the intercell hopping strength between the A and B sites of the adjacent unit cells as shown in Fig. 2.1. Since, the system is Hermitian, the strength of the hopping between A to B and B to A are the same. The SSH model becomes topologically nontrivial when the intracell hopping is weaker than the intercell one. The nontrivial topology in the system introduces edge states in the SSH chain.

A topological system also satisfies “bulk boundary correspondence", which suggests that the number of edge states in a system should be equal to its topological invariant. To investigate the bulk properties of the system, we impose periodic boundary conditions. Then the Hamiltonian of the system in the quasi-momentum space or k-space can be obtained by the Fourier transformation of the fermionic operators:

$$c_{\alpha,n} = \frac{1}{\sqrt{N}} \sum_{k} e^{ikn} \tilde{c}_{\alpha,k}.$$

Defining a Nambu spinor $\psi_k = \left(\tilde{c}_{A,k}, \tilde{c}_{B,k}\right)^T$ and substituting the above Fourier transformed operators, we can write the SSH Hamiltonian as

$$H_{SSH} = \sum_{k} \psi^{\dagger}_{k} \, \mathcal{H}_{SSH}(k) \, \psi_k,$$

where

$$\mathcal{H}_{SSH}(k) = \vec{h}(k) \cdot \vec{\sigma}.$$

The Hamiltonian in the k-space has the form

$$\mathcal{H}_{SSH}(k) = (\gamma_1 + \gamma_2 \cos k)\, \sigma_x + (\gamma_2 \sin k)\, \sigma_y. \tag{2.7}$$

In the above Hamiltonian, all three fundamental symmetries are preserved and thus this system belongs to the BDI class of the topological periodic table. For 1D systems, the winding number is the topological invariant. Here, the winding number is defined as the number of times the tip of the vector $\vec{h}(k)$ wraps the origin in the h_x-h_y plane.

2.4 Floquet formalism

A major part of this thesis has considered periodically driven systems. The most general formalism to study in any time-periodic system is the Floquet formalism. Therefore, we now present an essential features of this formalism.

This formalism was developed based on the Floquet theorem. This theorem was initially proposed in 1883 to solve linear differential equations with time-periodic coefficients. Later, this idea was extensively applied in different branches of Physics, namely quantum optics, ultracold atoms, optical lattices, etc. We start with the original proof of the Floquet theorem which was given in 1883 by G. Floquet. We consider a linear time-periodic differential equation of the form

$$\dot{\mathbf{x}} = \mathbf{A}(t)\mathbf{x}. \tag{2.8}$$

Here the coefficients matrix $\mathbf{A}(t)$ is time-periodic with the period T, i.e., $\mathbf{A}(t+T) = \mathbf{A}(t)$ and $\mathbf{x}$ is not necessarily time-periodic, but has the form $e^{\mu t}\mathbf{p}(t)$, where $\mathbf{p}(t)$ is also

periodic with period T and satisfies the relation

$$e^{\mu_1 T} e^{\mu_2 T} \dots e^{\mu_n T} = \exp\left(\int_0^T tr\,(\mathbf{A}(t'))\,dt'\right).$$

There are n possible solution of Eq. (2.8), $\mathbf{x^1}$, $\mathbf{x^2}$, ..., $\mathbf{x^n}$ which can be written in the form of a matrix $\mathbf{X}$ as

$$\mathbf{X}(t) = \left[\left[\mathbf{x^1}\right] \quad \left[\mathbf{x^2}\right] \quad \dots \quad \left[\mathbf{x^n}\right]\right] \tag{2.9}$$

Hence, $\mathbf{X}(t)$ is an $N \times N$ matrix solution of Eq. (2.8). Let, all these solutions $\mathbf{x^1}$, $\mathbf{x^2}$, ..., $\mathbf{x^n}$ are linearly dependent, then $\mathbf{X}(t)$ is non singular and fundamental matrix. For $\mathbf{X}(t_0) = \mathbb{I}$, $\mathbf{X}(t)$ is called principal fundamental matrix where $\mathbb{I}$ being the identity matrix. This fundamental matrix $\mathbf{X}(t)$ follows different assertions as given below (Only statements are given but it can be proved)

- If $\mathbf{X}(t)$ is a fundamental matrix, then $\mathbf{Y}(t)$ is another fundamental matrix of the form $\mathbf{Y}(t) = \mathbf{X}(t)\mathrm{B}$, where B is a non singular constant matrix. Here, $\mathbf{Y}(t)$ is nothing but written in terms of the linear combination of $\mathbf{X}(t)$.

- The determinant of $\mathbf{X}(t)$ is determined by the Wronskian $W(t)$ of $\mathbf{X}(t)$

$$W(t) = W(t_0) \exp\left(\int_{t_0}^{t} tr\,(\mathbf{A}(t'))\,dt'\right)$$

- If $\mathbf{X}(t)$ is a fundamental matrix, then $\mathbf{X}(t+T)$ is also a fundamental matrix and satisfies the matrix differential equation given in (2.8). There also exists a non singular constant matrix B such that

  $\rightarrow \mathbf{X}(t+T) = \mathbf{X}(t)\mathrm{B}$ for all values of t, and

  $\rightarrow \det(\mathrm{B}) = \exp\left(\int_0^T \mathrm{tr}\,(\mathbf{A}(t'))\,dt'\right)$.

  This assertion shows that the two solutions which differ by the period T can be obtained by a constant matrix.

- Let us consider that the eigenvalues of the constant matrix B are ρ_1, ρ_2, ..., ρ_n. These eigenvalues are called characteristic multipliers whereas for Eq. (2.8), μ_1, μ_2, ..., μ_n are characteristic exponents or Floquet exponents which satisfy

$$\rho_1 = e^{\mu_1 T}, \rho_2 = e^{\mu_2 T}, \ldots, \rho_n = e^{\mu_n T}.$$

  The Floquet exponents may be complex.

- There also exist a solution $\mathbf{x}(t)$ of Eq. (2.8) such that

  $\rightarrow \mathbf{x}(t+T) = \rho \mathbf{x}(t)$, and

  $\rightarrow \mathbf{x}(t) = e^{\mu t}\, \mathbf{p}(t)$, where $\mathbf{p}(t)$ is time-periodic

- If μ is replaced by $\mu + i\frac{2\pi}{T}$, then the above solution becomes

$$\mathbf{x}(t) = e^{\mu t}\mathbf{p}(t)e^{i2\pi t/T},$$

  where $e^{i2\pi t/T}$ is again periodic with period T. This shows that μ is not unique, but it does not change the result.

From here, we move to the use of this basic Floquet formalism to solve the time-periodic Schrödinger equation (TDSE).

2.4.1 Exact methods to calculate the effective Hamiltonian

The well TDSE is given as

$$i\frac{d}{dt}\,|\psi(t)\rangle = H(t)\,|\psi(t)\rangle. \tag{2.10a}$$

According to the ansatz of Floquet theory, the solution of the time-dependent Schrödinger equation (TDSE) for the periodically driven Hamiltonian will be of the form

$$|\psi_n(t)\rangle = e^{-i\epsilon_n t}\,|u_n(t)\rangle, \text{ where } |u_n(t)\rangle = |u_n(t+T)\rangle. \tag{2.10b}$$

In this equation, $|\psi_n(t)\rangle$ is the fundamental matrix which is given by $\mathbf{X}(t)$, ϵ_n is μ and $|u_n(t)\rangle$ is $\mathbf{p}(t)$ as described in the previous section. Here we set the Planck constant $\hbar = 1$ and $T = 2\pi/\omega$ as the time period. The states $|\psi_n(t)\rangle$ are known as the Floquet states [56]. The time-periodic states $|u_n(t)\rangle$ are called Floquet modes and ϵ_n represents the quasi-energy of the n-th state. The Floquet states are the temporal analogue of the Bloch states of solid-state physics [57, 58], where the Hamiltonian has the periodicity in space.

The Floquet states are the eigenstates of the time-evolution operator over one driving period, i.e.,

$$U(t_0 + T,\, t_0)\,|\psi_n(t_0)\rangle = e^{-i\epsilon_n T}\,|\psi_n(t_0)\rangle,$$

where t_0 is an arbitrary initial time. Therefore, one can obtain the Floquet states and the quasienergies, by diagonalising the time-evolution operator $U(t_0 + T,\, t_0)$, which is defined within a single time-period. The eigenvalues $e^{-i\epsilon_n T}$ and the corresponding eigenstates $|\psi_n(t_0)\rangle$ are gauge independent, but the quasienergy ϵ_n and the corresponding Floquet mode $|u_n(t)\rangle = e^{i\epsilon_n t}\,|\psi_n(t)\rangle$ are gauge dependent. By introducing an integer label $m = \pm 1, \pm 2, \ldots$, we get all the possible gauges of the quasienergies $\epsilon_{nm} = \epsilon_n + m\omega$ and the corresponding Floquet modes $|u_{nm}(t)\rangle = e^{im\omega t}\,|u_n(t)\rangle$, which give the same Floquet state $|\psi_n(t)\rangle$. Substituting, the general representation

$$|\psi_n(t)\rangle = e^{-i\epsilon_{nm} t}\,|u_{nm}(t)\rangle \tag{2.11}$$

in the TDSE [Eq. (2.10a)], we get the Floquet Hamiltonian as

$$\mathcal{H}_F : \left[i\frac{d}{dt} - H(t) \right] |u_{nm}(t)\rangle = \epsilon_{nm} |u_{nm}(t)\rangle. \tag{2.12}$$

The above relation forms an eigenvalue problem in an extended Hilbert space $\mathbb{H} \otimes \mathbb{T}$. The extended Hilbert space, also known as the Sambe's space, where $\mathbb{H}$ is the usual Hilbert space and $\mathbb{T}$ is a Hilbert space spanned by the time-periodic functions $e^{-im\omega t}$ with $m \in \mathbb{Z}$ [59]. The time-periodic property of the Hamiltonian $H(t)$ and the Floquet modes $|u_n(t)\rangle$ allow us to expand these systems in the Fourier series. This process splits the driven spectrum into an infinite number of copies of undriven Hamiltonian separated by $m\omega$. This process is called the Floquet replica method, which is analogous to the dressed atom picture of the electromagnetic field induced atomic systems [60]. Therefore m is called the photon numbers. In the Sambe space, the general representation of the Floquet Hamiltonian is:

$$\mathcal{H}_F = \begin{bmatrix} \ddots & \vdots & \vdots & \vdots & \vdots & \vdots & \iddots \\ \dots & H_0 - 2\omega & H_{-1} & H_{-2} & H_{-3} & H_{-4} & \dots \\ \dots & H_1 & H_0 - \omega & H_{-1} & H_{-2} & H_{-3} & \dots \\ \dots & H_2 & H_1 & H_0 & H_{-1} & H_{-2} & \dots \\ \dots & H_3 & H_2 & H_1 & H_0 + \omega & H_{-1} & \dots \\ \dots & H_4 & H_3 & H_2 & H_1 & H_0 + 2\omega & \dots \\ \iddots & \vdots & \vdots & \vdots & \vdots & \vdots & \ddots \end{bmatrix}, \tag{2.13a}$$

where

$$H_m = \frac{1}{T} \int_0^T H(t)\, e^{-im\omega t}\, dt. \tag{2.13b}$$

By construction/definition, the Floquet Hamiltonian is exact if one considers an infinite number of photon sectors. However, in numerics, we have to consider only a finite

number of photon sectors. The number of photon sectors is decided by the strength of the driving frequency ω. Suppose the driving frequency is of the order or smaller than the characteristic frequencies of the undriven system, one has to consider a larger number of photon sectors to get convergence in the calculation of the (dressed) Floquet bands around *zero* photon sector. On the other hand, one has to consider only a few photon sectors for a very high frequency.

2.4.2 Perturbative schemes

The replica method is an exact method which works in high frequency as well as in the low-frequency regime. However, this method has a drawback in solving a large matrix and difficult to perform any analytical calculation. There are two different perturbative schemes which work in high-frequency regimes. These perturbative schemes facilitate us to perform the analytical calculation for the effective Hamiltonian. Van vlech and Brillouin-Wigner are two perturbative methods which use an expansion series in the inverse power of driving frequency [61, 62].

Let us now consider a time-periodic Hamiltonian of the form

$$\hat{H}(t) = \hat{H}_0 + \hat{V}(t), \tag{2.14}$$

where $\hat{H}_0$ is the undriven Hamiltonian and $\hat{V}(t) = \hat{V}(t+T)$ is the external time-periodic driving. In Ref. [61], the time-evolution operator is redefined in terms of the initial time t_i and final time t_f, and this is given as

$$\begin{aligned} \hat{U}(t_i, t_f) &= \hat{U}^{\dagger}(t_f)\, e^{-iH_{\text{eff}}(t_f - t_i)}\, \hat{U}(t_i) \\ &= e^{-i\hat{K}(t_f)}\, e^{-iH_{\text{eff}}(t_f - t_i)}\, e^{i\hat{K}(t_i)}. \end{aligned} \tag{2.15}$$

Here t_i is the time when driving starts and $(t_f - t_i)$ is the time interval in which the

system evolved, and t_f is the final time of the driving. In this equation, H_{eff} is the time-independent Hamiltonian operator which does not depend on the initial and final time, whereas $\hat{K}(t)$ is a kick operator, which also describes micromotion. All the time-dependency of the system is referred to as the kick operator.

Using the following expressions, one can derive the effective Hamiltonian H_{eff} in the high-frequency regime as

$$H_{\text{eff}}^{\text{vV}} = H_0 + \frac{1}{\omega}\left[H_n, H_{-n}\right] + \frac{1}{\omega^2}\left[\left[H_0, H_n\right], H_{-n}\right] + O\frac{1}{\omega^3} \tag{2.16}$$

The higher-order terms with these two methods are very small for the high driving frequency. In the limit high frequency, i.e., $\omega \to \infty$, the effective Hamiltonian will be just H_0 and contribution from the higher order photon sector is negligible.

3

Floquet topological phases with high-Chern number in periodically driven E-SSH model

---

The contents of this Chapter has been published in Journal of Physics: Condensed Matter as Aayushi Agrawal & J.N.Bandyopadhyay (2022).

3.1 Introduction

The discovery of the integer quantum Hall (IQH) effect under a strong magnetic field [5] unveiled a new family of materials called topological insulators (TIs) [15–17]. The TIs are mostly observed in compounds made of heavy elements with strong spin-orbit coupling. Unlike in the usual insulators, the topological insulators have conducting edges or surfaces with the insulating bulk part. The topological materials are classified based on the dimension and symmetries of the systems [39, 40, 63]. The topology of a system is quantified by topological invariant, which is a constant integer and does not vary

under any continuous deformation of the energy bands (or Hamiltonian) [10]. Besides some natural solid-state materials [64, 65], the topological properties are experimentally simulated in ultra-cold atoms [61, 66], photonic systems [67], etc.

In a two-dimensional (2D) honeycomb lattice, Haldane introduced a complex next-nearest-neighbor (NNN) hopping to simulate a magnetic field-like effect. This leads to the realization of the quantum anomalous Hall (QAH) effect in the system [12]. In this 2D system, a topological phase transition from a normal insulator to a Chern insulator is observed by varying the hopping phase and the sub-lattice potential difference [12, 68, 69]. Recent investigations of realizing the Haldane model-like effect in lower-dimensional systems led to the so-called *extended* Su-Schrieffer-Heeger (E-SSH) model, which is described in one-dimension (1D). The original SSH model is the simplest possible 1D system which shows topological property [40, 46]. This model was proposed to describe the electronic properties of the poly-acetylene chain [44, 45]. Following the idea of Haldane, in the E-SSH model, in addition to a standard nearest-neighbor (NN) hopping, the NNN hopping term is introduced [70]. Furthermore, the hopping strengths are modulated by a cyclic variable that plays the role of an additional synthetic dimension. This synthetic dimension, together with the momentum, defines an effective 2D space on a real 1D space [71–73]. Consequently, instead of the winding number, one has to now calculate the Chern number as a topological invariant for this effective 2D system [74]. In the E-SSH model, if we also introduce an onsite potential, then one can map the synthetic dimension, and the momentum of this exactly with two momenta of the Haldane model [70]. Therefore, this mapping gives a clear understanding of the relation between the E-SSH model and the Haldane model. However, instead of two modulated terms (the onsite and the NNN) together with the SSH Hamiltonian, it is experimentally easier to realize the version of the E-SSH model that has only the modulated NNN term with the SSH Hamiltonian. Recently, some other versions of the E-SSH models are also

investigated [75–78].

The QAH effect is experimentally realized mostly in magnetic topological insulators [79–84] and in bilayer graphene twisted with a magic angle [85, 86]. In all these investigations, the QAH is observed only with the Chern number $C = \pm 1$. Very recently, the QAH effect is observed with a tunable Chern number up to $C = 5$ [87]. In this work, a system of multiple layers with alternating magnetic and undoped topological insulators was fabricated to observe high Chern numbers. Interestingly, the number of undoped topological layers decides the Chern number of the system. Moreover, higher topological phases with $2 \leq |C| \leq 4$ are observed in the Kitaev-Heisenberg ferromagnet with next to next nearest neighbor interaction [88]. In Harper-Hofstadter model, energy bands with $|C| > 1$ are also reported [89, 90].

Recent studies have established that the nontrivial topological properties can be ascribed to some topologically trivial systems by applying external time-periodic driving [50, 91–99]. Since the periodically driven systems are studied under Floquet theoretical framework, these synthetic topological systems are called *Floquet topological* systems. In the literature, Floquet topological system was introduced in the context of the topological aspects of quantum chaotic systems [100]. Many times, the Floquet systems show new exotic topological phases that may not be realized by any static means. For example, new Floquet topological phases in graphene illuminated by circularly polarized laser field [101, 102], higher-order topological phases in superconductor [103, 104], generating multiple Majorana modes [105], alter the native topology of the SSH model [106], etc.

Very recently, it has been observed that periodic driving can generate topological insulators with larger Chern numbers in higher dimensional (higher than 1D) systems [107–117]. Since the 1D E-SSH model can be mapped to the 2D Haldane model, a natural question is whether one can realize larger Chern numbers in the Floquet E-SSH model. The richer topological phases with higher Chern numbers are obtained when the

SSH system is periodically modulated in time [118]. Moreover, the topological phases with larger Chern numbers were reported in a Dirac delta-kicked SSH model with onsite potential [119]. Here, we have applied smooth sinusoidal drivings to the E-SSH model having the usual NN hopping of the SSH model and an additional NNN hopping to realize the topological phases with large Chern number.

3.2 Model

This section starts with the description of the E-SSH model. In this paper, we consider the same version of the *static* E-SSH model, which was originally proposed in Ref. [70]. Here we discuss the salient features of this model, and then introduce the periodically driven version of this. We also present a basic theoretical background that is needed to quantify and analyze the results.

3.2.1 Undriven E-SSH model

The original SSH model is a 1D chain that consists of two sub-lattices, represented by sites A and B in every unit cell. In this model, as shown in Fig. 3.1(a), only intra-cell hopping among A and B sites and the NN inter-cell hopping are allowed. Figure 3.1(b) shows that the same dynamics can also be described on a ladder geometry by placing each dimer vertically. For the E-SSH model, an additional NNN hopping from the A-site (B-site) of a unit cell to the A-site (B-site) of the neighboring unit cell is included. The E-SSH model can also be described as a 1D chain and a ladder. These are shown respectively in Figs. 3.1(c) and 3.1(d). Following [70], we consider the Hamiltonian of

the undriven E-SSH model as

$$\begin{aligned} H_{E-SSH} = & \underbrace{-\sum_n \left\{\gamma_1 c^\dagger_{A,n} c_{B,n} + \gamma_2 c^\dagger_{A,n+1} c_{B,n}\right\} + \text{h.c}}_{\equiv H_{SSH}} \\ & + \underbrace{\sum_n \left\{\gamma_A c^\dagger_{A,n+1} c_{A,n} + \gamma_B c^\dagger_{B,n+1} c_{B,n}\right\} + \text{h.c.}}_{\equiv H_{NNN}}, \end{aligned} \tag{3.1}$$

where H_{SSH} is the standard SSH Hamiltonian and H_{NNN} is the NNN hopping part of the Hamiltonian. The operators $c_{A,n}$ ($c_{B,n}$) and $c^\dagger_{A,n}$ ($c^\dagger_{B,n}$) are the annihilation and creation operators defined on the sub-lattice $A(B)$. Here the parameters

$$\gamma_1 = (1 + \delta\cos\theta) \text{ and } \gamma_2 = (1 - \delta\cos\theta)$$

respectively denote the intra-cell and inter-cell hopping strengths. Here the parameter δ is always set as positive. In the SSH model, the relative strengths of the hopping amplitudes decide the topological property of the system. Here we have modulated the hopping amplitudes by a single cyclic parameter θ. Therefore, the Hamiltonian becomes periodic in θ, i.e., $H_{E-SSH}(\theta) = H_{E-SSH}(\theta + 2\pi)$. The cyclic parameter θ can be considered as an additional synthetic dimension.

In the NNN hopping part, the following form of the hopping strengths are considered:

$$\gamma_A = g_A + h\cos(\theta + \phi) \text{ and } \gamma_B = g_B + h\cos(\theta - \phi),$$

where the constant parameters (g_A, g_B) and the modulation strength h are introduced to avoid the overlap between the two bands. Moreover, a parameter ϕ is introduced to observe a topological phase transition at $\phi = 0$. This phase transition is identified by the change of sign of the Chern number at this point.

In order to observe the properties of the bulk energy of the E-SSH model, periodic

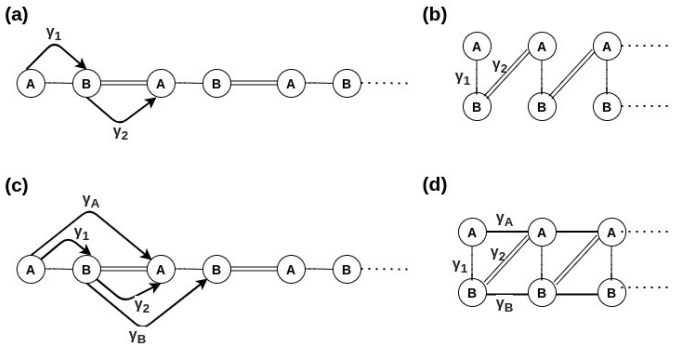

FIGURE 3.1: The original SSH model can be described by two geometrical structures: (a) a linear chain and (b) a ladder geometry. The same is shown for the E-SSH model in (c) and (d).

boundary condition (PBC) is imposed on the system. The PBC allows the transformation of the Hamiltonian from the real space to the momentum space (k-space) via Fourier transformation.

$$c_{A/B,n} = \frac{1}{\sqrt{N}} \sum_k e^{ikn}\, \tilde{c}_{A/B,k}, \tag{3.2}$$

where N is the number of sites in each sub-lattice and this number is also equal to the number of dimers. Substituting these Fourier transformed operators in Eq. (3.1) and defining Nambu spinors $\Psi_k = \left(\tilde{c}_{A,k} \;\; \tilde{c}_{B,k}\right)^T$, we write down the Hamiltonian in the k-space as

$$\begin{aligned} H_{\text{E-SSH}} &= \sum_k \Psi_k^\dagger\, \mathcal{H}_{\text{E-SSH}}(k)\, \Psi_k, \\ \text{with } \mathcal{H}_{\text{E-SSH}}(k) &= h_{k0}\mathbb{1} + \boldsymbol{h}(k)\cdot\boldsymbol{\sigma}, \end{aligned} \tag{3.3a}$$

where $\mathcal{H}_{\text{E-SSH}}(k)$ is the Bloch Hamiltonian and $\boldsymbol{\sigma} = \left(\sigma_x,\ \sigma_y,\ \sigma_z\right)$ are Pauli (pseudo) spin operators defined in the sub-lattice degrees of freedom. The parameter h_{k0} and the components of the parameter vector $\boldsymbol{h}(k) = \left(h_{kx},\ h_{ky},\ h_{kz}\right)$ are given as

$$\begin{aligned} h_{k0} &= (\gamma_A + \gamma_B)\cos k,\ \ h_{kx} = -(\gamma_1 + \gamma_2 \cos k) \\ h_{ky} &= -\gamma_2 \sin k,\ \ h_{kz} = (\gamma_A - \gamma_B)\cos k. \end{aligned} \tag{3.3b}$$

Symmetries in the system

The SSH Bloch Hamiltonian $H_{SSH}(k) \equiv \mathcal{H}_{\text{E-SSH}}(k)\big|_{\gamma_A=\gamma_B=0}$ follows three fundamental symmetries:

$$\mathcal{T}^{-1}\,\mathcal{H}_{\text{SSH}}(k)\,\mathcal{T} = \mathcal{H}_{\text{SSH}}(-k), \quad \text{(Time - reversal)} \tag{3.4a}$$

$$\mathcal{P}^{-1}\,\mathcal{H}_{\text{SSH}}(k)\,\mathcal{P} = -\mathcal{H}_{\text{SSH}}(-k), \quad \text{(Particle - Hole)} \tag{3.4b}$$

$$\mathcal{C}^{-1}\,\mathcal{H}_{\text{SSH}}(k)\,\mathcal{C} = -\mathcal{H}_{\text{SSH}}(k), \quad \text{(Chiral)}. \tag{3.4c}$$

Here, the time-reversal operator $\mathcal{T} = K$, the complex conjugation operator, and the particle-hole operator $\mathcal{P} = \sigma_z K$ are anti-unitary operators. The other symmetry operator, the chiral operator, $\mathcal{C} = \mathcal{P}\,\mathcal{T} = \sigma_z$ is a unitary operator. Even though this is a unitary symmetry, but it does not follow the standard commutation relation $\left[\sigma_z,\, \mathcal{H}_{\text{SSH}}(k)\right] = 0$, rather it follows the anti-commutation relation $\left\{\sigma_z,\, \mathcal{H}_{\text{SSH}}(k)\right\} = \sigma_z\,\mathcal{H}_{\text{SSH}}(k) + \mathcal{H}_{\text{SSH}}(k)\,\sigma_z = 0$. The chiral symmetry appears in the SSH model due to the absence of any hopping within the sub-lattices. Consequently, the parameter vector $\boldsymbol{h}(k)$ of the SSH Hamiltonian lies on the $x - y$ plane; and depending on whether the tangent of $\boldsymbol{h}(k)$ encloses the origin with the variation of k, the SSH model shows its topological property. This topological property is quantified by the winding number, which counts how many times the tangent of $\boldsymbol{h}(k)$ encircles the origin as we vary k within the Brillouin zone (BZ), i.e., $k = -\pi$ to π. Since the SSH Hamiltonian satisfies these three symmetries, this system is classified as the BDI class of the *ten-fold way of classification* of the quantum topological matters [40, 120, 121].

The addition of the NNN term H_{NNN} with the Hamiltonian H_{SSH} introduces a hopping within the sub-lattices. Consequently, this additional term breaks the chiral symmetry in the E-SSH model. Unlike the SSH case, due to the presence of σ_z in the Bloch Hamiltonian of the E-SSH model, the parameter vector $\boldsymbol{h}(k)$ does not lie on the $x-y$ plane,

and therefore the tip of this vector cannot enclose the origin. Consequently, the winding number becomes ill-defined for this system. However, in this model, the modulation parameter θ can be varied adiabatically from 0 to 2π without closing the gap between the bands for any non-zero value of the parameter ϕ. Since, the modulation parameter θ plays the role of a synthetic dimension, the E-SSH model becomes an effective 2D system defined on the periodic (k, θ)-space, which is geometrically identical to a torus. The topological property of a system higher than 1D is generally quantified by topological invariants known as Chern numbers which is defined in Chapter 2 in Eq. 2.5.

Depending upon the parameters γ_A and γ_B, symmetries of the E-SSH model changes [70]. We can see from the E-SSH Hamiltonian in Eq. (3.3), when $\gamma_A = \gamma_B$, the σ_z term vanishes in the Bloch Hamiltonian. For this case, in addition to the chiral symmetry $\mathcal{C}$, the particle-hole symmetry $\mathcal{P}$ also breaks down. This symmetry breaking results in an asymmetry in the energy bands and appearance of non-zero degenerate edge states. For $\gamma_A = -\gamma_B$ case, instead of σ_z term, now the term with the identity matrix $\mathbb{1}$ vanishes. Therefore, instead of the particle-hole symmetry, now the time-reversal symmetry $\mathcal{T}$ breaks down in the system. In this case, the energy spectrum will again be symmetric, but now the degeneracy of the non-zero edge states will be lifted. Finally, for the general case, when the parameters γ_A and γ_B do not satisfy any special relation, then the three symmetries mentioned above break down in the E-SSH model. For this case, the energy bands will be asymmetric, and the edge states will be non-zero and non-degenerate. In this paper, we consider the general case $|\gamma_A| \neq |\gamma_B|$, where none of the symmetries is preserved.

3.2.2 Periodically driven E-SSH model

We now describe the periodically driven E-SSH model which we extensively study as a prototype model for a realization of the high Chern number topological phases. The

Hamiltonian of this model is

$$\hat{H}_{E-SSH}(t) = \hat{H}_{E-SSH} + \hat{V}(t), \tag{3.5a}$$

where $\hat{H}_{E-SSH}$ is already defined in Eq. (3.3) and the time-periodic potential satisfies the condition $\hat{V}(t+T) = \hat{V}(t)$. Consequently, the total Hamiltonian is also a time-periodic $\hat{H}_{E-SSH}(t+T) = \hat{H}_{E-SSH}(t)$. The time-periodic driving part of the Hamiltonian is considered as

$$\begin{aligned}\hat{V}(t) = v_1(t) \sum_n (c^\dagger_{A,n} c_{B,n} - c^\dagger_{A,n+1} c_{B,n}) \\ + v_2(t) \sum_n (c^\dagger_{A,n+1} c_{A,n} - c^\dagger_{B,n+1} c_{B,n}) + h.c.\end{aligned} \tag{3.5b}$$

Here, the periodic driving: $v_1(t) = 2V_1 \cos\omega t$ and $v_2(t) = 2V_2 \cos(\omega t + \alpha)$, where V_1 and V_2 are the driving amplitudes, the frequency of both the driving is ω, and α is a phase factor. In the momentum space, the Bloch Hamiltonian of the time-periodic E-SSH model will be of the form

$$\begin{aligned}\mathcal{H}_k(t) = (\gamma_A + \gamma_B)\cos k\, \mathbb{1} - [(\gamma_1 + \gamma_2 \cos k) - v_1(t)(1 - \cos k)]\, \sigma_x - [\gamma_2 + v_1(t)] \sin k\, \sigma_y \\ + [\gamma_A - \gamma_B + 2v_2(t)]\, \cos k\, \sigma_z.\end{aligned} \tag{3.6}$$

The driving protocol is chosen in such a way that it introduces the time-dependent functions only with the pseudo-spin operators $\boldsymbol{\sigma}$.

Floquet analysis of the driven E-SSH model

In this paper, we need to consider maximum *eleven* photon sectors to achieve numerical convergence. Since, our driving protocol is monochromatic (absence of any harmonics

of ω), $H_m = 0$ for $|m| \geq 2$ and for the remaining values $m = 0, \pm 1$ we have in the k-space

$$\begin{aligned} H_{0,k} &= (\gamma_A + \gamma_B)\cos k\ \mathbb{1} - (\gamma_1 + \gamma_2 \cos k)\,\sigma_x \\ &\quad - \gamma_2 \sin k\,\sigma_y + (\gamma_A - \gamma_B)\cos k\,\sigma_z, \\ H_{\pm 1,k} &= V_1\left[(1-\cos k)\,\sigma_x - \sin k\,\sigma_y\right] \\ &\quad + 2V_2\, e^{\pm i\alpha}\cos k\,\sigma_z. \end{aligned} \tag{3.7}$$

Here, the Hamiltonian $H_{0,k}$, defined in $m = 0$ photon sector, is just the undriven E-SSH Hamiltonian represented in the k-space. In Sambe's space representation, the periodic driving introduces the off-diagonal blocks $H_{\pm 1}$ in the Floquet Hamiltonian, which connects different photon sectors. In the k-space, the eigenstates of H_F form Floquet-Bloch bands where both (quasi)energy and momentum are periodic. In the crystalline solid, the Bloch bands hybridize and develop bandgaps at the crossing points [57, 58]. Similarly, the crossing points between different photon sectors of the Floquet-Bloch bands open dynamical gaps [59]. The Floquet-Bloch bands are also experimentally observed on the surface of a 3D topological insulator Bi_2Se_3 [122]. Again the Chern number can be the quantifier of the topology of the Floquet-Bloch bands. For that, in Eq. (2.5), one has to replace the Bloch bands by the Floquet-Bloch bands.

3.3 Results

In this section, we present all the results. First, we discuss the Floquet (energy) band diagram of the E-SSH model and study their topological properties by calculating the Chern number. We then discuss how the Floquet topological phase transition in the system is dependent on the parameters of the undriven system. Later, we discuss the role of the driving frequency and the amplitude on the Floquet topological phase transition. Finally, we concentrate on the parameter regimes where the topological phases with

higher Chern numbers $C = 3$ and $C = 5$ are observed.

3.3.1 Floquet (energy) band diagrams of the E-SSH model and its topological property

The Floquet band diagram for the driven E-SSH model with driving frequency $\omega = 2.8$ (larger than the maximum bandgap of the undriven system i.e $\omega > 2.0$) are presented in Fig. 3.2(a)-(c) respectively for $\phi = -\pi/4$, 0 and $\pi/4$ as a function of momenta k. For the each case, the Floquet-Bloch bands are presented for three ($m = 0, \pm 1$) photon sectors. Here the synthetic dimension $\theta \in [0, 2\pi]$ plays the role of a parameter. Since the driving frequency is much larger than the maximum bandgap of the undriven system, this value of ω can be considered as a high-frequency case. Therefore, we find that the calculation with only five photon sectors ($m = 0, \pm 1, \pm 2$) is sufficient for the numerical convergence of the three central Floquet bands. In all the calculation, we set $V_1 = V_2$, the phase factor $\alpha = \pi/2$, and the dimerization constant $\delta = 0.3$. Hereafter, we replace all V_1 and V_2 by a single parameter V. For Fig. (3.2), we set $V = 0.1$ and the other parameters as $g_A = g_B = 0.1$ and $h = 0.2$. Here, we note that the bulk spectra for $\phi = \pi/4$ and $-\pi/4$ are identical. We also notice a pair of gaps between the Floquet bands at $k = \pm\pi/2$ and another pair of gaps at the BZ boundary $k = \pm\pi$. The gaps at the BZ boundary disappear at $\phi = 0$. This opening and closing of the Floquet bandgaps indicate a topological phase transition in the system.

In Fig. 3.2(d)-(f), we have presented the Floquet energy spectrum of the central three Floquet bands for the open boundary condition as a function of the cyclic parameter θ for the same values of ϕ. These show the presence of edge states in the system, a typical property of any topologically nontrivial system. Here again, Figs. 3.2(d) and (f) show the identical nature of the energy spectrum, whereas Fig. 3.2(e) shows the closing off of the *bandgap* at $\theta = \pi/2$ and $3\pi/2$.

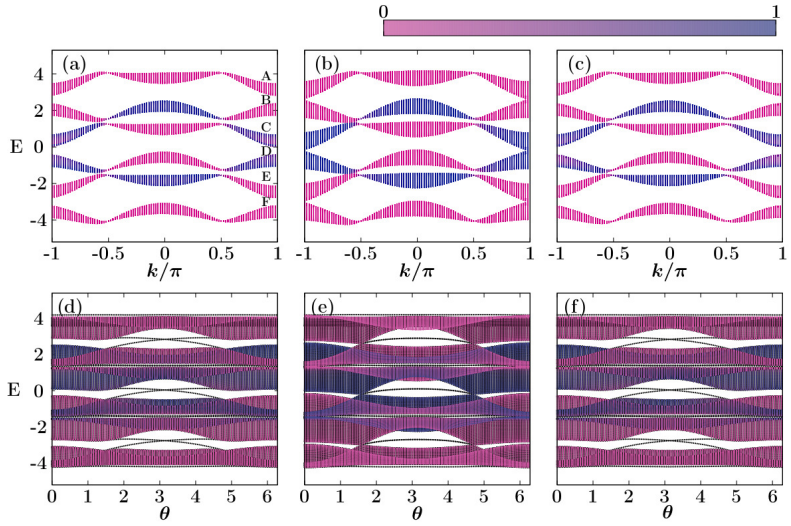

FIGURE 3.2: Floquet bands of the driven extended SSH model at the high-frequency regime. The parameters $\delta = 0.3$, $\omega = 2.8$, and $V = 0.1$ are kept fix for all the cases. In the high-frequency range, we use 5 photon sectors in the numerics and present the Floquet bands corresponding to the central three photon sectors with $m = 0, \pm 1$. The color bar represents the static weight ($|\langle u^0_\alpha | u^0_\alpha \rangle|^2$) and separates the zero photon sector from the higher photon sectors [123]. In the upper panel, E is plotted as a function of k; while in the lower panel, E is plotted against θ. We set $\phi = -\pi/4$ for the left side figures, $\phi = 0$ for middle figures, and $\phi = \pi/4$ for the right side figures. Nonzero value of ϕ induces a additional gap at $k = \pm\pi$ which is absent for $\phi = 0$. Varying ϕ, topological phase transitions are exhibited via the closing and opening of the Floquet bands. The lower panel shows the quasienergies for the open boundary condition and the edge states presence.

According to Fig. 3.2(a) and (c) or Fig. 3.2(d) and (f), the bulk spectrum for $\phi = -\pi/4$ and $\phi = \pi/4$ do not reveal different topological property of the Floquet bands. Therefore, we need to calculate the Chern number to detect the topological phase transition. We follow Ref. [124] to evaluate the Chern number. In Fig. 3.2(a), where $\phi = -\pi/4$,

$$C_\beta = \begin{cases} 1 & (\beta = B, D, F) \\ -1 & (\beta = A, C, E). \end{cases} \tag{3.8}$$

Here C_β is the Chern number of the Floquet-Bloch band β, as shown in Fig. 3.2(a). Similarly, for $\phi = \pi/4$ [Fig. 3.2(c)], we get

$$C_\beta = \begin{cases} 1 & (\beta = A, C, E) \\ -1 & (\beta = B, D, F) \end{cases} \tag{3.9}$$

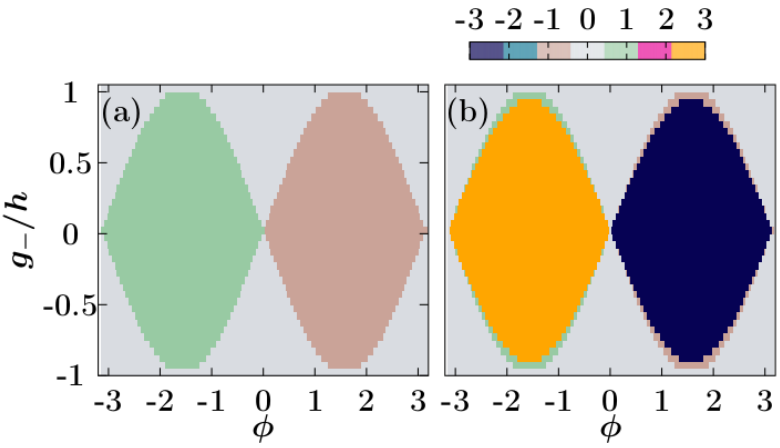

FIGURE 3.3: Phase diagram for the topological phase transition is shown via plotting the sum of the Chern numbers C_s of all the Floquet bands below $E = 0$ as a function of g_-/h and ϕ. Here, *nine* photon sectors are required to get numerical convergence. In (a) $V = 0.1$ and in (b) $V = 1.0$ are considered for a fixed $\omega = 2.8$. The color bar represents C_s.

We obtain the Chern number of opposite signs for the Floquet bands corresponding to two opposite values $\phi = \pi/4$ and $\phi = -\pi/4$. For any arbitrary nonzero values of ϕ with opposite sign, we always find $C = \pm 1$. This indicates topological phase transition at $\phi = 0$. The same results were obtained even for the undriven E-SSH model [70].

In the remaining part of this section, we explore the role of periodic driving in the topological phase transition. We particularly show the advent of Floquet-Bloch bands with higher Chern numbers due to periodic driving.

3.3.2 Phase diagram between g_-/h and ϕ

We now examine the effect of the NNN hopping and the time-periodic driving on the topological properties of the E-SSH model. In Fig. 3.3, we present a phase diagram to show the topological phase transition in the driven E-SSH model. We define a parameter $g_- = (g_A - g_B)/2$, which gives a measure of the relative strength of two intra-sublattice hopping (A to A and B to B). The parameter g_- is then scaled with respect to the modulation parameter h, where we fix $h = 0.2$. In Fig. 3.3, we consider two different driving amplitudes $V = 0.1$ and $V = 1.0$ for a fixed frequency $\omega = 2.8$. Here we plotted the sum of the Chern numbers, denoted by C_s, of all the Floquet bands below $E = 0$

as a function of g_-/h and ϕ. Since here we are considering high-frequency driving, we find that the consideration of five photon sectors is sufficient for the convergence. Nevertheless, here we have presented the results with nine photon sectors.

In Fig 3.3(a), we present the result for the driving amplitude $V = 0.1$. For this case, the phase diagram is showing three topologically distinct regions: a non-trivial region within $\phi \in [-\pi, 0)$ with $C_s = +1$; another non-trivial region within $\phi \in (0, \pi]$ with $C_s = -1$, and the rest is topologically trivial region with $C_s = 0$. If we compare the phase diagram of the driven E-SSH model with the undriven E-SSH model, discussed in Ref. [70], then we observe that the periodic driving flips the sign of the Chern number. One should also note that the phase diagram of the E-SSH model shares qualitatively similar properties with the Haldane model [12]. In Fig. 3.3(b), we consider the same phase diagram corresponding to the stronger driving field $V = 1.0$. For this case, we observe appearance of higher Chern number $C_s = \pm 3$ in the same parameter regime where we observed $C_s = \pm 1$ for the weaker driving strength $V = 0.1$. Interestingly, here we notice that $C_s = +3$ ($C_s = -3$) region is surrounded by a thin layer of $C_s = +1$ ($C_s = -1$) region. Overall these phase diagrams suggest two types of topological phase transition depending on the periodic driving strengths: for the weaker driving, the Chern number flips its sign; and for the stronger field, the Chern number not only flips its sign but also increases the magnitude.

3.3.3 Topological phase transition from a non-trivial phase to another non-trivial phase

In the previous subsection 3.3.2, we have shown two different types of topological phase transitions depending on the driving strengths at the high-frequency limit. We now explore the simultaneous role of the driving strength and the frequency on the topological phase transition in a more detail. More precisely, we study the variation of the sum of the

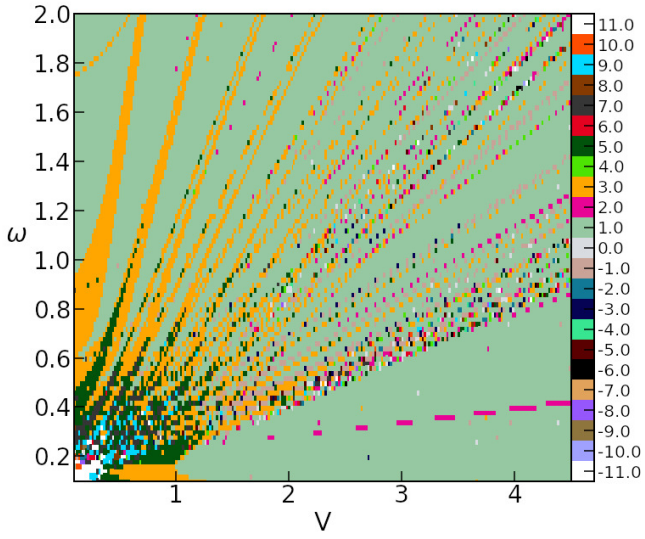

FIGURE 3.4: The summed over Chern number C_s is plotted as a function of ω and V in the low-frequency regime $\omega \leq 2$. Here twenty one photon sectors are considered for the convergence. The other parameter are set at: $\phi = -\pi/4$, $g_A = g_B = 0.1$, and $h = 0.2$. The color bar represents the Chern number C_s. For very small values of ω and V, the sum of the Chern number of the Floquet bands is very high which is shown with the white region. A major part of the phase diagram is occupied by the lower Chern number phases with $C_s = +1$. Topological phases with high Chern numbers $|C| > 1$ are demonstrated by different color coding.

Chern number C_s as a function of the driving strength V and the frequency ω. We have found that, by tuning the driving amplitude and frequency, one can get C_s of different magnitudes.

Here we cover a wide range of frequencies: from a much smaller frequency than the lowest bandgap energy of the undriven E-SSH model to a frequency much higher than the largest bandgap of the same undriven system. We present the phase diagram for the lower frequency regime ($0.1 \leq \omega \leq 2.0$) and the higher frequency range ($\omega > 2.0$) separately. Here, we set the parameter $\phi = -\pi/4$ and keep it fixed throughout this analysis. Except at $\phi = 0$, we get a qualitatively similar topological property for any other values of ϕ. We also notice that the Chern number changes sign with the sign change of ϕ.

For the lower frequency regime, the phase diagram is shown in Fig. 3.4. This phase diagram displays the sum of the Chern numbers C_s of all the Floquet bands below $E = 0$. The Chern number C_s is playing the role of the topological invariant. Here we consider the driving amplitude in the range $0.1 \leq V \leq 4.5$. In this regime, around the left-bottom

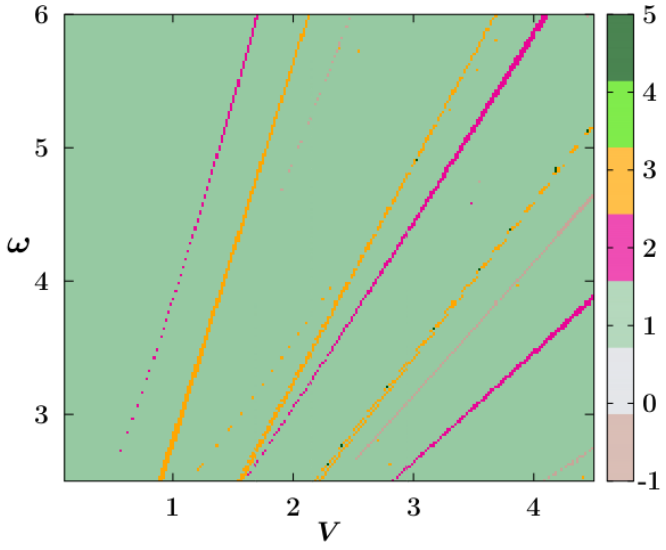

FIGURE 3.5: A similar phase diagram as the previous figure is presented in the high-frequency regime $\omega > 2$. Here, *nine* photon sectors are considered and the parameters are fixed at: $\phi = -\pi/4$, $g_A = g_B = 0.1$ and $h = 0.2$. The color bar represents the Chern number C_s.

corner of the plot marked by a white region, we observe huge values of $|C_s|$. We have marked the different regions of the phase diagram by colors only for $|C_s| \leq 10$. For smaller values of both ω and V, we see many jumps in the values of C_s which indicate rapid Floquet topological phase transition.

A major portion of this phase diagram is occupied by the topologically non-trivial phase with $C_s = 1$ (light-green color). We have found some scattered regions where $|C_s| > 1$. However, among these different higher Chern number regions, we find that the regions with $|C_s| = 2$, 3, 5, and 9 are prominent. The other values of the Chern number are observed as many tiny islands in the phase diagram, which are mostly located near the V-axis with $V \gtrsim 2$. Since here the frequency is low enough, we have to consider twenty one photon sectors to achieve convergence in our calculation. A qualitatively similar topological property was reported for the case of periodically driven honeycomb lattice [62]. However, here we observe this in a 1D system.

In Fig. 3.5, we have presented the phase diagram in the higher frequency regime ($2.0 < \omega \leq 6.0$). Here we consider the same range of driving amplitude V as earlier. Because of the high-frequency regime, we need to consider only *five* photon sectors to

get convergence. However, here we present results with *nine* photon sectors. Here again, we mostly observe a “sea" of $C_s = +1$ region, but the regions with higher values of C_s are much smaller than the low-frequency case. We can see some strips of regions with $C_s = 2$ and 3. Here, we observe islands of minuscule sizes with the Chern number $C_s = 5$, which is the highest observed value of C_s for this high-frequency regime.

The Floquet topological phase transition discussed in this subsection can be understood by investigating the Berry curvature, whose integration over the BZ gives the Chern number. We know that when a (Floquet) topological phase transition takes place, the Berry curvature localizes near the band touching points in the BZ. In Fig. 3.5, we see tiny dark-green islands with $C_s = 5$ on the orange strip with $C_s = 3$. These points are the critical points of the Floquet topological phase transitions $C_s = 3 \leftrightarrow C_s = 5$. Therefore, in the next subsection, we study in detail the cases of higher Chern numbers $C_s = 3$ and 5 at the high-frequency regime. At this regime, the interactions among different photon sectors are minimal. As a consequence, we have found that the summed over Chern number C_s is equal to the Chern number C of the lower Floquet band of the zero photon sector. This happens because each photon sector with $m < 0$ contributes a pair of Chern numbers with the same magnitude but of opposite signs. Consequently, when we sum them up, they cancel each other, and only the Chern number corresponding to the lower Floquet band of the zero photon sector survives, and thus it leads to $C_s = C$.

3.3.4 Cases of the higher Chern numbers at the high frequency limit: $C = 3$ and 5

We now focus on two cases of higher Chern numbers with $C = 3$ and 5. Here we consider the regime of high-frequencies in ω and strong driving strengths V.

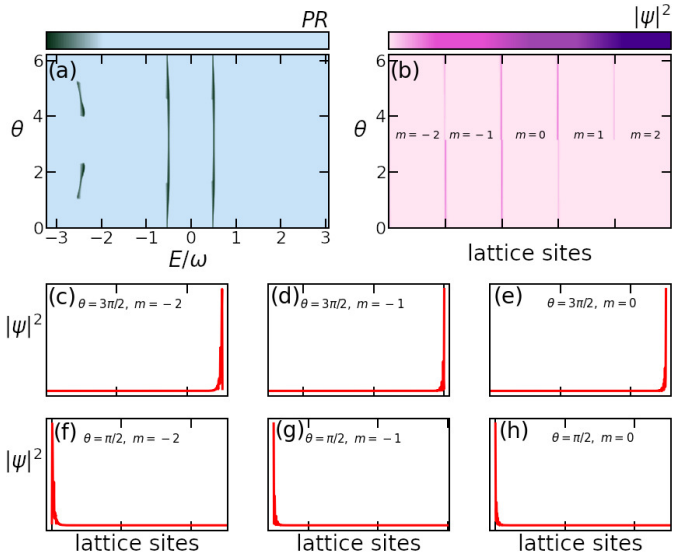

FIGURE 3.6: In (a), the density plot of the PR of all the eigenstates for $C = 3$ case are shown as a function of their eigenvalues E scaled by the external driving frequency ω (x-direction) and for different values of the parameter θ (y-direction). Here $\omega = 2.8$ and driving field strength $V = 1.0$. The darker color is identifying the localized states and the light color represents all delocalized bulk states. The localized states within $|E| < \omega$ are all edge states. However, the other localized states within $-3\omega < E < -2\omega$ are not edge states, these are localized in the bulk region. In (b), the edge states are shown. Here we see that, all the eigenstates corresponding to $E \simeq -0.6\omega$ have prominent component only at the edge in different photon sectors. In (c)-(h), we have presented a few typical edge states for two different values of θ and have shown their contribution in three photon sectors $-2 \leq m \leq 0$.

Case: $C = 3$

In Fig. 3.2, we showed the edge states for $|C| = 1$ by projecting the Floquet bands along the synthetic dimension θ for all possible values of the quasi-momentum k. Here, for $C = 3$ case, the driving amplitude is much stronger than $C = 1$ case. This stronger driving amplitude bends all the Floquet bands considerably. Consequently, the projection of the Floquet bands along θ direction hides all the edge states. Hence, to show the presence of edge states, we follow a different method by exploiting the localization property of the edge states. We calculate the participation ratio (PR) of all the eigenstates of the Floquet Hamiltonian as a measure of the (de)localized states. The PR of a state $|\psi\rangle$ in basis $\{|\phi_n\rangle\}$ is defined as: $\text{PR} = 1/\sum_n |c_l|^4$, where $|\psi\rangle = \sum_n c_n|\phi_n\rangle$. Here, the state $|\psi\rangle$ will be the eigenstates of the Floquet Hamiltonian. This calculation considers five photon sectors, sufficient for convergence since the frequency is high ($\omega = 2.8$). If $|\psi_i\rangle$

is an eigenstate of the Floquet Hamiltonian, then this state can be expanded as

$$|\psi_i\rangle = \sum_{l=1}^{L} \sum_{m=-2}^{+2} c_{lm} |l, m\rangle,$$

where $\{|l, m\rangle\}$ are the basis states with lattice sites $l = 1, \ldots, L$ and the photon sectors $-2 \leq m \leq +2$. Then the PR of the eigenstates of the Floquet Hamiltonian will be

$$\text{PR} = \left[\sum_{l=1}^{L} \sum_{m=-2}^{+2} |c_{lm}|^4 \right]^{-1}.$$

In Fig. 3.6(a), we present a density plot of the PR as a function of the energy (scaled by the driving frequency ω) and for all the values of the cyclic parameter $\theta \in [0, 2\pi]$. Here we have assigned a light-blue color to all the delocalized states with PR ≥ 30. The darker color represents the localized states. We detect localized eigenstates around $|E| = 0.6\omega$ for all values of θ. These localized states are all edge states. On the other hand, the localized states observed within $E = -2\omega$ to -3ω are not edge states; these are localized in the bulk part of the lattice.

In Fig. 3.6(b), we show the localized eigenstates with $E = -0.6\omega$ on the real lattice space for $\theta \in [0, 2\pi]$. This figure clearly shows that, for $\theta < \pi$, all these states are localized at the left edge of the lattice in photon sectors $-2 \leq m \leq 0$. Since we consider the summed over Chern number presented below $E = 0$, we have shown localized states

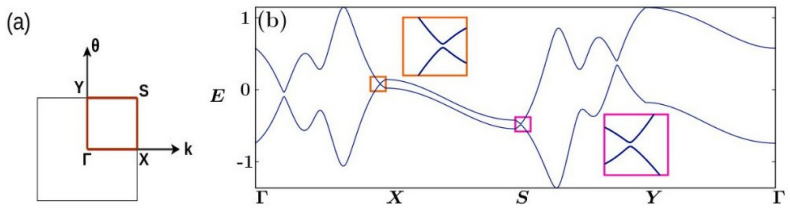

FIGURE 3.7: The Floquet bands are presented for $C = 3$ case along the high-symmetry lines. Here we set $V = 1.0$ and $\omega = 2.8$. Subfigure (a) demonstrates the high symmetry path $\Gamma - X - S - Y - \Gamma$ in the BZ. Here, in the (k, θ) coordinates, the symmetry points are at $\Gamma = (0, \pi)$, $X = (\pi, \pi)$, $S = (\pi, 2\pi)$, and $Y = (0, 2\pi)$. Subfigure (b) shows that there are many regions where Floquet bandgaps are very small. This behavior is responsible for the localization in the Berry curvature and consequently its leads to high Chern number.

only in the photon sectors $-2 \leq m \leq 0$. For $\theta > \pi$, the states are localized at the left edge of the lattice in the same photon sectors. This property is separately shown in Figs. 3.6(c)-(h). In these subfigures, we have shown two typical eigenstates with $\theta = 3\pi/2$ and $\theta = \pi/2$, and their contributions in every photon sector $-2 \leq m \leq 0$. For $\theta = 3\pi/2$ case, we see that the eigenstate is localized at the right edge in every photon sector. On the other hand, for $\theta = \pi/2$, we see that the eigenstate is localized at the left edge of every photon sector.

In the next two figures, we present the results relates to the high Chern number. Figure 3.7(a) shows a high symmetry path $\Gamma - X - S - Y - \Gamma$ by solid lines in the BZ. For a case of $C = 3$, we have then demonstrated in Fig. 3.7(b) the Floquet bands corresponding to $m = 0$ photon sector along the high symmetry path. Here we see a couple of points surrounded by the rectangles, where the Floquet bands are almost closing with tiny finite bandgaps. We have zoomed those regions to show clearly the presence of the bandgaps. The presence of gaps is allowed us to calculate the Chern number of the Floquet bands. If we tune the driving parameters (V, ω) slightly, we see band closing and reopening with a different Chern number ($C = 1$). Another interesting region is observed when we consider the high-symmetry path $X - S$. Here two bands are always nearby and varying almost parallel as we change the parameter $(\theta : \pi \longrightarrow 2\pi)$ along the $X - S$ path.

It is well known that the bandgap closing and opening are responsible for the localization of the Berry curvature in the reciprocal space. We have seen above that the bandgaps between the Floquet bands in the zero photon sectors are small at different points within the BZ. Therefore, we now investigate the effect of this behavior of the Floquet bands on the Berry curvature and its consequences in the Chern number. The results are shown in Fig. 3.8. According to our expectation, we see in Fig. 3.8(a) localization in the Berry curvature around the regions where the bandgaps are very small. Since the Chern number is obtained by integrating the Berry curvature over the BZ, we investigate the

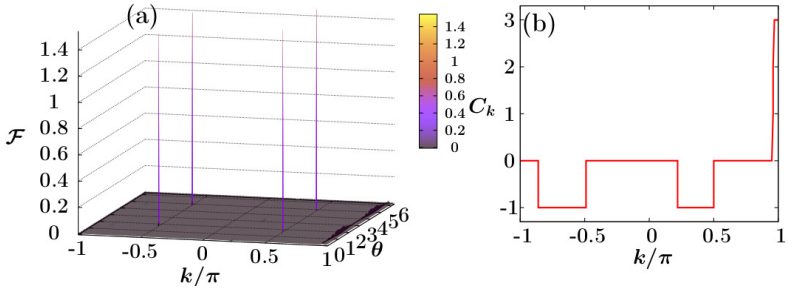

FIGURE 3.8: For $C = 3$, the Berry curvature is plotted in (a) as a function of k and θ for the lower Floquet band of the zero photon sector. The driving parameters are fixed at $V = 1.0$ and $\omega = 2.8$; and here *nine* photon sectors are considered. Fixing the parameters same as (a), C_k is plotted as a function of k in (b) to observe the contribution from the different parts of the BZ in the Chern number.

contribution of the Berry curvature from different regions of the BZ to the Chern number. For this purpose, we define a measure *local Chern number* C_k as

$$C_k = \frac{1}{2\pi} \int_{k'=-\pi}^{k} dk' \int_{\theta=0}^{2\pi} d\theta \; \mathcal{F}(k', \theta). \tag{3.10}$$

According to this definition, the Chern number and the local Chern number are related as $C = C_\pi$. In Fig. 3.8(b), we show how C_k changes with k. Here we observe transitions in C_k around those regions where the Floquet bandgaps are small. This is happening because the Berry curvature is nonzero exactly around those regions. Interestingly, except when $k \simeq \pi$, the local Chern number C_k is transitioning only within $0 \leftrightarrow (-1)$. These are happening exactly at those regions where the Floquet bandgaps are very small, as well as the bands are linearly dispersive. The transition $0 \longrightarrow 3$ at $k \simeq \pi$ can be understood by comparing the properties of the Floquet bands along the high-symmetry path $X - S$, which is defined as $\pi \leq \theta \leq 2\pi$ and $k = \pi$. Here, two Floquet bands vary in parallel, maintaining almost a fixed but small bandgap. In Fig. 3.8(a), we see the localization of the Berry curvature exactly along a line that is the same as the $X - S$ path.

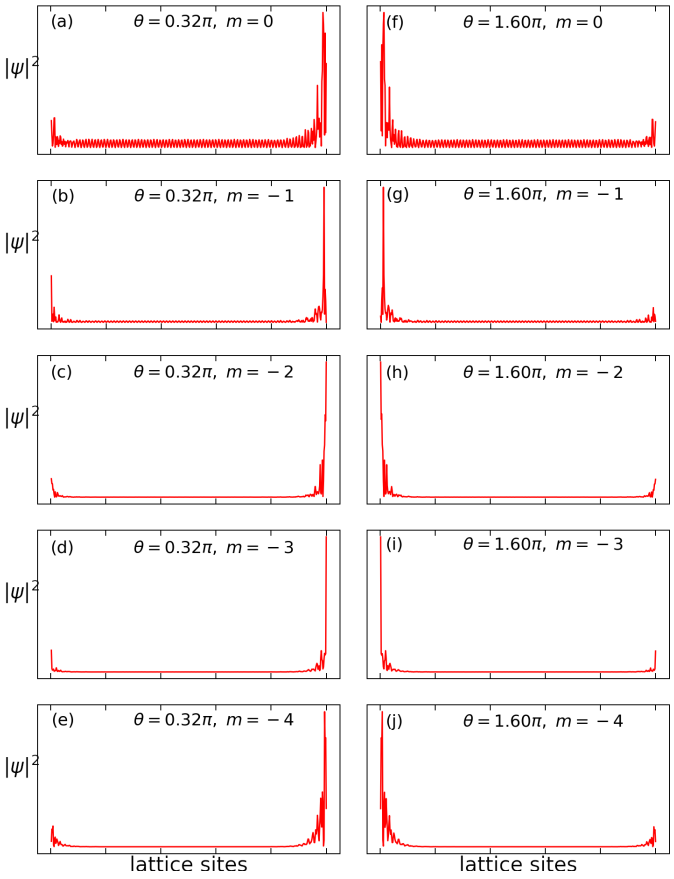

FIGURE 3.9: For $C = 5$ case, we follow exactly the same method as earlier to detect the edge states. Here we have consider the edge states for two different values of θ and has shown a typical one for each value of θ. In (a)-(e), we show an edge state corresponding to $\theta = 0.32\pi$ and its contribution in different photon sectors $-4 \leq m \leq 0$. Subfigures (f)-(j) is showing the same for $\theta = 1.60\pi$.

Case: $C = 5$

The results for this case are presented in Figs. 3.9 and 3.10. In Fig. 3.9, we once again picked up two localized eigenstates from $\theta = 0.32\pi$ and 1.60π following the same procedure as we did for $C = 3$ case. Figures 3.9(a)-(e) show the edge state corresponding to $\theta = 0.32\pi$ and its contribution in different photon sectors $-4 \leq m \leq 0$. In Figs. 3.9(f)-(j), the other localized state for $\theta = 1.60\pi$ and its contribution in different photon sectors are presented.

In Fig. 3.10(a), the Floquet band diagram is presented along the same high symmetry path $\Gamma - X - S - Y - \Gamma$ for the driving parameters $V = 3.02$ and $\omega = 4.8$. Here again, we observe multiple points where the Floquet bandgaps are very small with linear dispersive

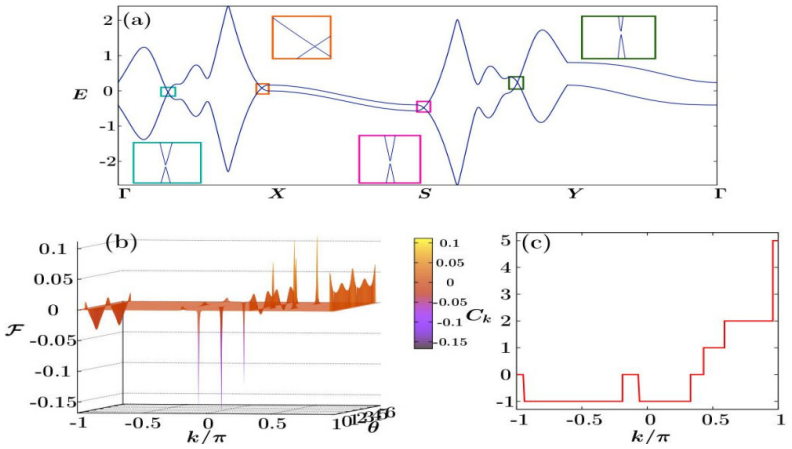

FIGURE 3.10: The driving parameters are set at $V = 3.02$ and $\omega = 4.9$; and *nine* photon sectors are considered for the numerics. Here for the lower Floquet band the Chern number $C = 5$. Subfigure (a) presents the Floquet band diagram along the same high symmetry path $\Gamma - X - S - Y - \Gamma$. Here we also find multiple points where the bandgaps are tiny. Again along $X - S$ path, the behavior of the Floquet bands is similar to the above case of $C = 3$. In (b), the Berry curvature is plotted as a function of k and θ for the lower Floquet band of the zero photon sector. Subfigure (c) presents C_k as a function of k.

bands. Moreover, along the $X - S$ path, the qualitative behavior of the Floquet bands is similar to the case of $C = 3$. We present the Berry curvature in Fig. 3.10(b). This figure shows the correlation between the localization of the Berry curvature and the Floquet bandgaps. According to our expectation, here again, we see that the smaller Floquet bandgaps are responsible for the stronger localization and *vice versa*. Like the previous case, we also see in Fig. 3.10(c) the appearance of nonzero Berry curvatures at different regions in the BZ, and that leads to the transitions in C_k. From the transition perspective, the property of the local Chern number is very rich here. We observe many different transitions in C_k. This is clearly the consequence of the complex structure of the Berry curvature as shown in Fig. 3.10(b). In this case, besides the transitions of $0 \leftrightarrow (-1)$, we also observe transitions like $0 \rightarrow 1$, $1 \rightarrow 2$, and $2 \rightarrow 5$. The final transition of $2 \rightarrow 5$ is happening again due to the same behavior of the Floquet bands along the high symmetry path $X - S$ as discussed above for the case of $C = 3$. In case of $C = 3$, the final transition of C_k was $0 \rightarrow 3$. The equal amount of jump in local Chern number $\Delta C_k = 3$ around $k = \pi$ suggests that the contribution of the $X - S$ path to the Chern number C is exactly

the same for both the high Chern number cases.

3.4 Summary and final remarks

In this paper, we study a periodically driven E-SSH model. An extensive study of different phase diagrams clarifies that the external periodic driving makes this system topologically much richer. First, we have found that our periodic driving protocol introduces gaps between the Floquet bands at the BZ boundary for non-zero values of the parameter ϕ. In the case of the undriven E-SSH model, the parameter ϕ determines the topology of the system. This result then motivates us to study a phase diagram in the parameter space of the relative strength of the NNN hopping and the parameter ϕ. We have observed that, for the weaker driving field strength, the phase diagram is almost identical ($C_s = 0 \text{ or } \pm 1$) to the phase diagram corresponding to the undriven system except that the sign of the Chern number is now opposite but of the same magnitude. However, for the stronger driving strength, the Chern number not only changes its sign, but its magnitude also increases with $C_s = \pm 3$. Moreover, we observe that the larger Chern number regions are surrounded by lower Chern number regions with $C_s = \pm 1$. The discovery of higher Chern numbers for the stronger driving field motivates us to extensively study the role of the driving parameters (ω and V) on the topological properties of the system.

We then study the topological phase diagram by studying the Chern number C_s as a function of the driving frequency ω and driving amplitude V. Here we concentrate separately on the driving frequency in two regimes: (1) lower than or the same order of the bandgap of the undriven E-SSH model; and (2) higher than the bandgap of the undriven E-SSH system. In the lower frequency regime, we observe many sharps topological phase transitions. Particularly for the weaker driving amplitudes, we observe topological phase transitions between a non-trivial phase with a very high Chern number to another non-trivial phase with another high Chern number. Higher Chern number

is also observed in the high-frequency regime but within a very restricted value of the driving parameters. Moreover, in this regime, we have observed the highest value of the Chern number as $C_s = +5$. The above discussion clearly shows that the 1D E-SSH model under monochromatic periodic driving can have many different topological phases with a much higher Chern number depending on the driving parameters.

We investigate in detail the higher Chern number cases with $C = 3$ and 5 at the higher frequency regime. The edge states are detected by calculating the PR of the energy eigenstates for all values of the synthetic dimension θ. After identifying the localized states, we then detected the edge states. Here we observe that whenever two Floquet bands in the zero photon sector come close to each other, the Berry curvature localizes there, and consequently, it contributes to the Chern number of the Floquet bands. In order to identify the contribution of the Berry curvature to the Chern number from different regions of the BZ, we introduce a measure "local Chern number" C_k. We see many jumps in the values of C_k when we plot this as a function of k, and these jumps exactly occur at those values of k where the gaps in two Floquet bands are very small.

In this study we consider a driving protocol of the form $V(t) = V_1 \cos \omega t + V_2 \sin \omega t$. Following the recently proposed perturbation theory in Ref. [125], this smooth driving protocol can be realized at the high-frequency limit (very large ω) upto an order of $1/\omega^2$ by a class of four-step pulse sequence of the form

$$\{H_0 + V_1, H_0 + V_2, H_0 - V_1, H_0 - V_2\},$$

where H_0 is the undriven Hamiltonian. Here each pulse is applied for the time interval $T/4$, where $T = 2\pi/\omega$. This kind of pulse sequences can be realized in cold atoms and optical lattice setup [126–128].

4

Theoretical study of N stacked SSH model via symmetry breaking

---

The contents of this Chapter has been published in Physical Review B as Aayushi Agrawal & J.N.Bandyopadhyay (2023).

4.1 Introduction

Different extensions of 1D SSH chain which either remains in 1D or 2D are investigated in the literature. As discussed in the previous Chapter, periodically driven E-SSH model was studied where monochromatic sinusoidal driving is used. The E-SSH model was considered as an effective 2D model, where the cyclic parameter plays the role of an additional synthetic dimension. In these extensions of the 1D SSH model, ladder structures and two coupled-SSH chains, have been proposed [129–137].

A series of works have studied two versions of the 2D SSH model: First, a square lattice, where each unit cell contains four different atoms [138, 139]. Therefore, this model has *four* energy bands. An interesting feature of this 2D SSH model is that it

shows nontrivial topology but with zero Berry curvature [140]. Second, a layered 2D SSH model is constructed by stacking N-number of SSH chains [141–145]. Moreover, one can obtain a layered structure of the 2D SSH model by promoting the cyclic parameter of the E-SSH model to (quasi)momentum. In general, a $(d + 1)$ dimensional layered structure can be constructed by stacking d dimensional TIs. This layered material is categorized as a new class of TIs, called *weak* TIs. Since the stacking happens in some particular direction, one can expect edge modes only in the stacking direction. Therefore, unlike the four bands 2D SSH model, where four edge modes may appear at all four sides, the N-stacked SSH model has edge modes only at the two sides along the direction of stacking. This results in an anisotropy of the edge states in the system.

Originally, this idea of stacking was incorporated in a generalized 3D quantum spin Hall (QSH) system [146, 147], where they formed 3D weak TIs from the layered 2D QSH [13, 14]. They also showed two distinct classes: weak TIs and strong TIs, depending on the nature of their surface states [146]. In this study, they observed that a small amount of disorder could destroy weak TIs and transform these into band insulators. A later study has demonstrated that the weak TIs are protected from any random disorder, provided this disorder does not break the TR symmetry and does not close the bulk energy gap [148]. Thereafter, a new topological phase was discovered near the transition from weak TIs to strong TIs, called topological *semimetal* (TSM) [149]. The TSMs are the phases where two (four) bands are separated by a finite band gap, however, there exist some points at the Fermi energy where both (four) bands have degeneracy [150, 151]. These degenerate band touching points are called Weyl (Dirac) nodes [152, 153].

Recently, a couple of extensive studies have found that, by varying the system parameters, the N-stacked SSH model makes a transition from trivial insulator to weak topological insulator via topological semimetal state [141, 142]. The experimental realization of this model has also been proposed [154]. Since this model is chiral symmetric,

we calculate the winding number as a topological invariant by dimension reduction. Until now, the N-stacked SSH model has been studied to preserve all the fundamental symmetries. Therefore, the above studies raise a natural question about the fate of the N-stacked SSH chains with various broken symmetries. The primary goal of this study is to investigate the impact of the broken symmetries on the N-stacked SSH model and catalog their interesting topological phases.

In this paper, we have considered a basic model of N-stacked half-filled SSH chains. This basic model preserves chiral, time-reversal (TR), and particle-hole (PH) symmetries like in the single SSH chain. The presence of these symmetries in the system suggests that its Hamiltonian satisfies the following conditions in quasi-momentum space or $\boldsymbol{k}$-space:

$$\begin{aligned} \mathcal{P}^{-1}\mathcal{H}(k_x,k_y)\,\mathcal{P} &= -\mathcal{H}(-k_x,-k_y), \\ \mathcal{T}^{-1}\mathcal{H}(k_x,k_y)\,\mathcal{T} &= \mathcal{H}(-k_x,-k_y), \\ C^{-1}\mathcal{H}(k_x,k_y)\,C &= -\mathcal{H}(k_x,k_y), \end{aligned} \tag{4.1}$$

where $\mathcal{P}$, $\mathcal{T}$, and C respectively represent chiral, TR, and PH operations. Based on these three fundamental symmetries, a periodic table of the topological materials was proposed to classify them [39, 40, 63]. A major part of this paper, preserving the PH symmetry in the system, investigate the topological properties of the system in the presence or absence of the chiral and the TR symmetries. These symmetries are systematically preserved or broken by allowing or restricting various hopping in the system. The TR symmetry is broken by considering hopping strengths with imaginary amplitude. Later, we also study the role of the PH symmetry on the topology of the system.

In this model of the N-stacked SSH chains, we have placed individual SSH chains along the x-direction, whereas in the y-direction, we have stacked N number of identical SSH chains. Here we have proposed different versions of the N-stacked SSH chains depending on the various hopping terms in the system. We consider two specific cases

for each of these versions: in one case, the individual SSH chains is topologically trivial (the winding number $w = 0$), and in the other case, the individual chain is topologically nontrivial ($w \neq 0$). We classify these different versions into two classes of Hamiltonians:

1. System with chiral symmetry. Because of this symmetry, off-diagonal terms appear in the Hamiltonian represented in the quasi-momentum space.

2. System without chiral symmetry. Along with the off-diagonal terms, now diagonal or mass terms appear in the Hamiltonian.

For the latter class, we have considered two sub-classes based on the presence and absence of the TR symmetry.

4.2 Weak topological insulator : N stacked SSH model

In this section, we study the N-stacked SSH chains model with chiral symmetry. This is the basic model whose structure is shown in Fig. (4.1). Here, N number of identical SSH chains are stacked along the y-direction, forming a 2D square/rectangular lattice model. Each SSH chain is a standard one with two sites per unit cell or one dimer per unit cell. Sites A and B are respectively represented by the red and black circles in the figure. Here we see that the *spin-less* electrons in this system can hop only to adjacent

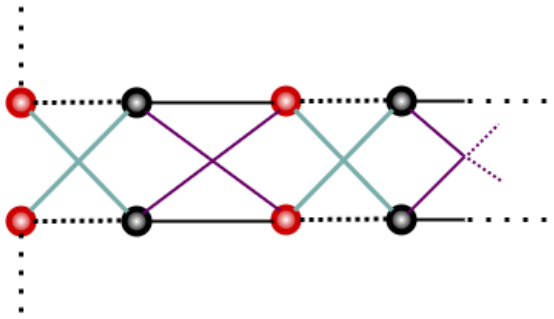

FIGURE 4.1: Schematic representation of the N-stacked SSH chains with chiral symmetry is presented. The red and black colored spheres, respectively, represent sites of A and B sub-lattices. The thick and dotted black bonds represent the inter-cell and intra-cell hopping within a chain, respectively. The neighboring chains are connected by light blue and purple dotted bonds.

or nearest neighbor sites through the bonds represented by the dotted and solid black lines along the x-direction. The electrons are allowed to hop only between neighboring chains, which are shown by the light blue and purple lines. This 2D lattice has only two sub-lattices. Therefore, like an SSH chain, this system has two energy bands.

The real-space Hamiltonian of this model is given as

$$\begin{aligned} H_{N-SSH} = & \sum_{n_x,n_y} \left[(1-\eta)\, c^{\dagger A}_{n_x,n_y} c^{B}_{n_x,n_y} + (1+\eta)\, c^{\dagger A}_{n_x+1,n_y} c^{B}_{n_x,n_y} \right] \\ & - \frac{\delta}{2} \sum_{n_x,n_y} \left[c^{\dagger A}_{n_x+1,n_y} c^{B}_{n_x,n_y+1} + c^{\dagger A}_{n_x+1,n_y+1} c^{B}_{n_x,n_y} \right] \\ & + \frac{\delta}{2} \sum_{n_x,n_y} \left[c^{\dagger A}_{n_x,n_y} c^{B}_{n_x,n_y+1} + c^{\dagger A}_{n_x,n_y+1} c^{B}_{n_x,n_y} \right] + \text{h.c.}, \end{aligned} \tag{4.2}$$

where $c^{A}_{n_x,n_y}$ (and $c^{B}_{n_x,n_y}$) and $c^{\dagger A}_{n_x,n_y}$ (and $c^{\dagger B}_{n_x,n_y}$) are the fermionic annihilation and creation operators corresponding to the sub-lattice A (and B). The first and the second terms of the Hamiltonian represent intra-cell and inter-cell hopping. The parameter η fixes the relative strengths of these hopping, and thus it decides the topological property of the individual SSH chain. The last two terms of the Hamiltonian describe the coupling between two adjacent SSH chains, and the parameter δ decides the strength of these hopping. Note that all the inter-chain hopping strengths are considered equal here. For the case of the full periodic boundary condition (PBC), i.e., the PBC is considered along both x- and y-directions, we have to stack N number of SSH chains on a toroidal surface. Correspondingly, the quasi-momentum space will also be a 2D toroidal surface, defined in $\boldsymbol{k} = (k_x,\, k_y)$ space. For the PBC, the above Hamiltonian in $\boldsymbol{k}$-space is expressed by substituting the real-space fermionic operators $\{c_{n_x,n_y}\}$ with its $\boldsymbol{k}$-space representation as

$$c_{n_x,n_y} = \frac{1}{N_x N_y} \sum_{k_x,k_y} e^{i(n_x k_x + n_y k_y)}\, \tilde{c}_{k_x,k_y}, \tag{4.3}$$

where N_x is the total number of unit cells (or dimers) along x-direction and N_y is the

number of SSH chains stacked along y-direction. We thus get the $\boldsymbol{k}$-space Hamiltonian as

$$H_{N-SSH} = \sum_{\boldsymbol{k}} \Psi_{\boldsymbol{k}}^{\dagger}\, \mathcal{H}_{N-SSH}(\boldsymbol{k})\, \Psi_{\boldsymbol{k}}, \tag{4.4}$$

where $\Psi_{\boldsymbol{k}} = \begin{bmatrix} c_{\boldsymbol{k}}^{A} & c_{\boldsymbol{k}}^{B} \end{bmatrix}^{T}$ are the Nambu spinors and the Hamiltonian kernel or the Bloch Hamiltonian $\mathcal{H}_{N-SSH}(\boldsymbol{k})$ is expressed as

$$\begin{aligned} \mathcal{H}_{N-SSH}(\boldsymbol{k}) &= \boldsymbol{h}(\boldsymbol{k}) \cdot \boldsymbol{\sigma}, \quad \text{where} \\ h_x(\boldsymbol{k}) &= \big[(1+\cos k_x) + (1-\cos k_x)(\delta \cos k_y - \eta)\big] \\ h_y(\boldsymbol{k}) &= \big[(1+\eta) - \delta \cos k_y\big]\, \sin k_x, \end{aligned} \tag{4.5}$$

were σ_α's with $\alpha = \{x, y, z\}$ are Pauli's pseudo-spin matrices. Two energy bands of this system are obtained from the eigenvalues of the above Bloch Hamiltonian and these are

$$\begin{aligned} E_{\pm}(\boldsymbol{k}) &= \pm\sqrt{h_x(\boldsymbol{k})^2 + h_y(\boldsymbol{k})^2} \\ &= \pm\sqrt{2}\big[\,(1+\cos k_x) + (1-\cos k_x)(\delta \cos k_y - \eta)^2\,\big]^{1/2}. \end{aligned} \tag{4.6}$$

Here, we consider two cases of the N-stacked SSH chains model: in one case, we set $\eta > 0$ to make the individual SSH chain topologically nontrivial; and in the other case, when $\eta < 0$, the individual SSH chain is topologically trivial. The presence of the edge states in the bulk gap characterizes the topological property of the system. The edge states are observed for the open boundary conditions (OBC) only. For better visibility of the edge states, here we consider energy bands under *partial* open boundary conditions (POBCs), when at a time the OBC is considered only along one direction, and the PBC is considered along the other direction. Geometrically, this suggests that the N-stacked SSH chains are now placed on a cylinder, where the cylinder's axis is along x-direction in one case and along y-direction in the other case. Under these two different POBC

cases, the Hamiltonians become

$$\begin{aligned}
&\mathcal{H}_{N-SSH}(k_x) = \\
&\left[\left\{(1-\eta) \ + \ (1+\eta)\cos k_x\right\}\sigma_x + (1+\eta)\sin k_x\sigma_y\right] \otimes \mathbb{1}_{Ny} \\
&+ \frac{\delta}{2}\left[(1-\cos k_x)\sigma_x - \sin k_x\sigma_y\right] \otimes \sum_{n_y}(c^{\dagger}_{n_y}c_{n_y+1} + \text{h.c.})
\end{aligned} \tag{4.7}$$

and

$$\begin{aligned}
&\mathcal{H}_{N-SSH}(k_y) = \sum_{n_x}\left[(1-\eta)\, c^{\dagger A}_{n_x}c^{B}_{n_x} + (1+\eta)\, c^{\dagger A}_{n_x+1}c^{B}_{n_x}\right] \\
&+ \delta\cos k_y \sum_{n_x}\left[c^{\dagger A}_{n_x}c^{B}_{n_x} - c^{\dagger A}_{n_x+1}c^{B}_{n_x}\right] + \text{h.c.} \\
&= \sum_{n_x}\left[\left(1-\eta+\delta\cos k_y\right)\, c^{\dagger A}_{n_x}c^{B}_{n_x} + \left(1+\eta-\delta\cos k_y\right)\, c^{\dagger A}_{n_x+1}c^{B}_{n_x}\right] \\
&+ \text{h.c.},
\end{aligned} \tag{4.8}$$

where $\mathcal{H}_{N-SSH}(k_x)$ is the Hamiltonian corresponding to the POBC case with the PBC is considered only along the x-direction; and $\mathcal{H}_{N-SSH}(k_y)$ represents the POBC Hamiltonian with the PBC is considered only along the y-direction. In other words, we can say that $\mathcal{H}_{N-SSH}(k_x)$ describes a model of N-stacked SSH chains placed on the surface of a cylinder, whose axis is along the y-direction; whereas $\mathcal{H}_{N-SSH}(k_y)$ describes the same 2D model on the surface of a cylinder, whose axis is along the x-direction. Here, $\mathbb{1}_{Ny}$ is a $N \times N$ identity matrix.

In Eq. (4.8), the Hamiltonian $\mathcal{H}_{N-SSH}(k_y)$ mimics a single SSH chain, where k_y plays the role of a parameter that modulates the hopping amplitudes. For each value of k_y, this Hamiltonian represents an SSH chain. Consequently, the defined weak topological invariant is independent of k_y, and that can be calculated only along the x-direction. If we compare with a single SSH chain, this system is topologically nontrivial when $\left(1+\eta-\delta\cos k_y\right) > \left(1-\eta+\delta\cos k_y\right)$. This imposes the following condition on k_y in

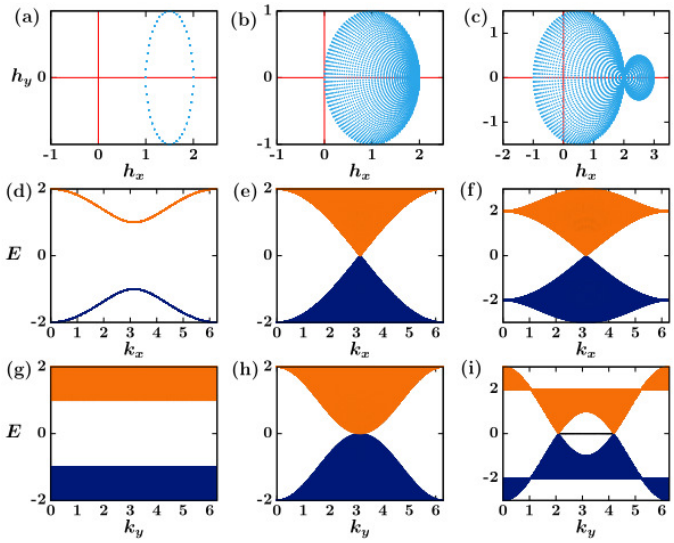

FIGURE 4.2: In (a)-(c), the closed curves in the $h_x - h_y$ plane are presented for the model proposed in Fig. 4.1 for $N_y = 200$ topologically trivial stacked SSH chains with 100 dimers in every single chain (i.e., $N_x = 200$). Here, we consider three different cases: $\delta = 0.0$, $\delta = 0.5$ and $\delta = 1$ with $\eta = -0.5$. In (d)-(f), corresponding energy bands are plotted as a function of k_x for the POBC case, where PBC is considered only along x-direction and OBC is considered along y-direction. Similarly, in (g)-(i), energy bands are plotted as a function of k_y, where PBC is considered only along the y-direction and OBC is considered along the x-direction.

the first Brillouin zone (BZ):

$$\cos^{-1}\left(\frac{\eta}{\delta}\right) < k_y < 2\pi - \cos^{-1}\left(\frac{\eta}{\delta}\right). \tag{4.9}$$

In Figs. 4.2(a)-(c) and 4.3(a)-(c), the Hamiltonian kernel $\boldsymbol{h}(\boldsymbol{k})$ is shown in the $h_x - h_y$ plane for individual trivial and nontrivial SSH chain, respectively for three different values of δ. Fig. 4.2 (a) and 4.3 (a) are plotted for $\delta = 0$, i.e., there is no interchain hopping. Therefore, it behaves like a single SSH chain. The closed curve encloses the origin only when the individual SSH chain is nontrivial. The next two figures are plotted for non-zero values of δ. Here, in contrast to the single SSH chain, it has a finite number of circles, which either enclose the origin or pass through the origin or not encloses the origin depending on the above condition of k_y. This is clearly observed when the energy bands are plotted as a function of k_y under POBCs.

We show the energy bands corresponding to the Hamiltonian $\mathcal{H}_{N-SSH}(k_x)$ and

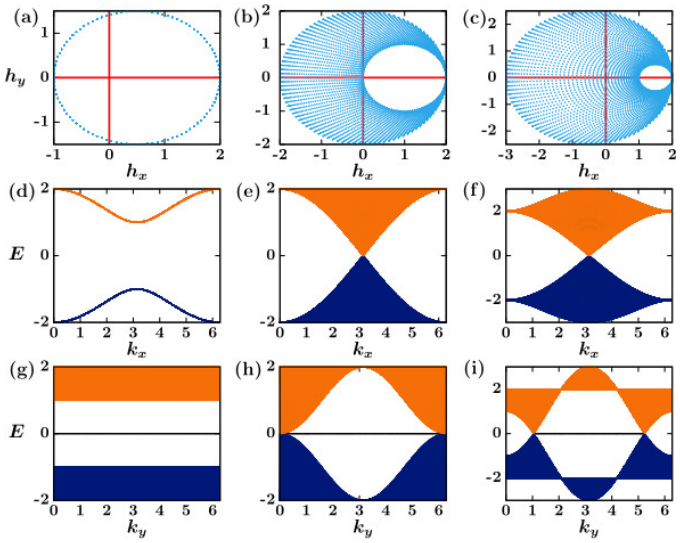

FIGURE 4.3: The same results are presented here as in Fig. (4.2), but here all the individual SSH chain is topologically nontrivial. Here, we again consider the same three different values of the parameter δ (= 0.0, 0.5 and 1.0) and fix the other parameter $\eta = 0.5$.

$\mathcal{H}_{N-SSH}(k_y)$ in Fig. 4.2(d)-(f) and Fig. 4.2(g)-(i), respectively. Here, we consider the individual SSH chain to be topologically trivial. We observe that, as the interchain hopping δ increases, the N-stacked SSH model constructed with the topologically trivial individual SSH chains starts exhibiting nontrivial nature.

The energy band diagrams for the case when the individual SSH chain is nontrivial are shown in Fig. 4.3(d)-(i). For this case, the N-stacked SSH model shows the zero energy edge states for all values of δ. However, the length of the zero energy states is decided by the above condition on k_y. The region where the zero energy edge states are presented is known as “Edge Brillouin zone (EBZ)". The edge states in the EBZ are bridged by two bulk nodes and this explains the topological semimetal behavior of the system [142]. For $\delta = 1$, besides the shifting of the band-touching points, we do not see any qualitative difference in the bands in Figs. 4.2(i) and 4.3(i). For this system, the

phase transitions occur in the following parametric way:

$$\begin{aligned} \eta < -\delta \quad &: \text{Trivial insulator,} \\ -\delta < \eta < \delta \quad &: \text{Topological semimetal,} \\ \eta > \delta \quad &: \text{Weak topological insulator.} \end{aligned} \tag{4.10}$$

In this study, we choose the parameters such that the system has edge states irrespective of the nature of the individual SSH chain, whether it is trivial or nontrivial.

4.3 Generalized N-stacked SSH chains with broken chiral symmetry

The chiral symmetry is broken in the N-stacked SSH chains by introducing bonds within the sub-lattices, leading to the intra-sub-lattice hopping. The Chern number is a topological invariant for systems with broken chiral symmetry. Moreover, here we have considered two sub-classes of systems depending on the presence and absence of the TR symmetry. Following Haldane's approach [12], the TR symmetry is broken by introducing intra-sub-lattice hopping with imaginary strength. This section is divided into two subsections. In subsections 4.3.1 and 4.3.2, we have respectively discussed the topological properties of the system with and without the TR symmetry, while the chiral symmetry is broken for both cases. Note once again that the PH symmetry is preserved.

4.3.1 Topological phases with TR symmetry

As a target of designing N-stacked SSH models of nontrivial topology with the Chern number $C \neq 0$, we introduce additional intra-sub-lattice hopping in our basic model. This hopping introduces a mass term in the $\boldsymbol{k}$-space Hamiltonian. Consequently, this term breaks the chiral symmetry and lifts the degeneracy of the two bands, which results in

an opening of the band gap. The broken chiral symmetry is the cause of the existence of non-zero and non-degenerate energy edge states. Here, we set $\gamma_A = -\gamma_B = \gamma$ to preserve the PH symmetry in the system, where γ_A (γ_B) is A to A (B to B) sub-lattice hopping strength. Note that here the intra-sub-lattice hopping strengths are equal in magnitude, but opposite in sign. As a consequence, the energy spectrum is symmetric about $E = 0$. For the condition $\gamma_A = \gamma_B$, the spectrum does not remain symmetric about $E = 0$ due to the broken PH symmetry, but the inversion symmetry (discussed later in Sec. 4.6) is preserved in the system. This model preserves the TR symmetry due to the real value of the chiral symmetry-breaking terms in the Hamiltonian.

We introduce NNN intra-chain (i.e., along the x-direction) bonds with real hopping strengths while keeping the original bonds intact. These bonds give additional hopping within an SSH chain from its A site (or B site) of a unit cell to the A site (or B site) of the adjacent unit cell. The schematic representation of this model is presented in Fig. 4.4(a). For this model, the Hamiltonian in the $\boldsymbol{k}$-space is given as:

$$\mathcal{H}_{\boldsymbol{k}} = \mathcal{H}_{N-SSH}(\boldsymbol{k}) + 2\gamma \cos k_x \, \sigma_z. \tag{4.11}$$

Here, the first term at the right side $\mathcal{H}_{N-SSH}(\boldsymbol{k})$ is given in Eq. (4.5). The second term appears due to the newly introduced NNN bonds, where we set the intra-sub-lattice long-range hopping strength $\gamma = 0.2$. In Figs. 4.4(b)-(e), the energy bands are presented for the POBC. Here the system satisfies the PBC along the y-direction, but the OBC along the x-direction. The corresponding POBC Hamiltonian is

$$\mathcal{H}(k_y) = \mathcal{H}_{N-SSH}(k_y) + \gamma \sum_{n_x} \left[\left(c^{\dagger A}_{n_x} c^{A}_{n_x+1} - c^{\dagger B}_{n_x} c^{B}_{n_x+1} \right) + h.c. \right] \tag{4.12}$$

Here, $\mathcal{H}_{N-SSH}(k_y)$ is already given in Eq. (4.8). Figs. 4.4(b) and 4.4(d) show the energy bands with the POBC for the Hamiltonian $\mathcal{H}(k_y)$, when the individual chain of

the stacked SSH chains is topologically trivial (winding number $w = 0$). On the other hand, Figs. 4.4(c) and (e) show the energy bands, when the individual SSH chain is topologically nontrivial ($w \neq 0$).

In Fig. 4.4(d), we see the presence of the edge states at the band gap. These states are not connecting the valence and the conduction band. Therefore, the Chern number of this system is $C = 0$. The energy band diagram of this system is similar to the bands shown in Ref. [70], where an SSH chain with an additional synthetic dimension was studied. For the other case, as shown in Fig. 4.4(e), an edge state emanating from one band forms a single lobe by crossing the edge state emanating from the other band twice and finally enters into the same band from where it was emanated. The edge state emanating from the other band shows the same property. Here again, the Chern number $C = 0$. The $C = 0$ is also observed for both cases by analytical means in Sec. 4.4. Even though for these cases $C = 0$, the presence of the edge states indicates nontrivial topology. This nontriviality will be revealed by the calculation of the 2D Zak phase in Sec. 4.5.

4.3.2 Topological phases without TR symmetry

In the previous subsection 4.3.1, we observed that the TR-symmetric N-stacked SSH chains without chiral symmetry could not have a nontrivial topology with a non-zero Chern number. Here, we study the N-stacked SSH chains with broken chiral symmetry and TR symmetry. The chiral symmetry was broken earlier by introducing intra-sub-lattice hopping with real hopping strengths. Here, we simultaneously break the chiral and the TR symmetries by replacing all the intra-sub-lattice real hopping strengths with imaginary amplitudes. In experiments, the imaginary hopping amplitude can be realized by applying a magnetic field-like gauge field in the direction perpendicular to the plane of the 2D lattice. However, following Haldane [12], we consider intra-sub- lattice imaginary hopping amplitude, which gives the gauge-field-like effect even without any

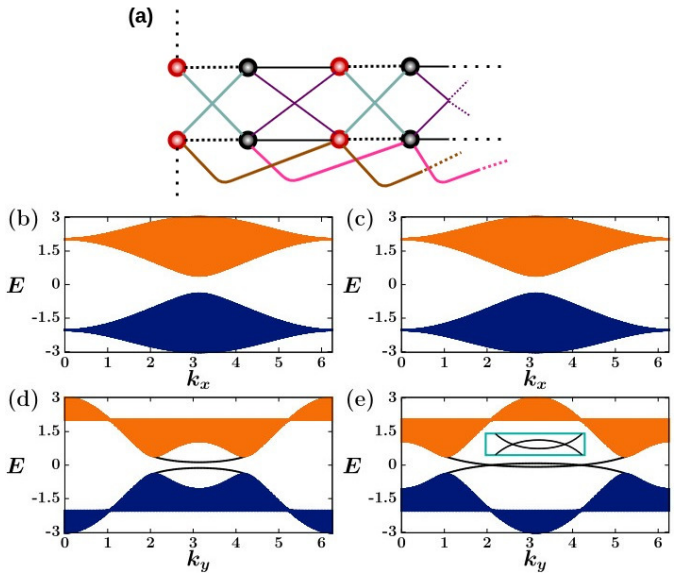

FIGURE 4.4: A schematic diagram of a N-stacked SSH model with broken chiral symmetry is shown in subfigure (a). Here, the intra-sub-lattice hopping strengths are real numbers and are shown by the solid-brown and magenta bonds. The corresponding energy bands under the POBCs are shown in subfigure (b)-(e). In subfigures (b) and (c), energy bands are shown as a function of k_x, where the PBC is considered along the x-direction and the OBC is considered along the y-direction. In subfigure (b), the individual SSH chain is trivial ($\eta = -0.5$); and in subfigure (c), each SSH chain is nontrivial ($\eta = 0.5$). For these two values of the parameter η, energy bands are shown as a function of k_y in subfigures (d) and (e), respectively. In these cases, the PBC is considered along the y-direction, and the OBC is considered along the x-direction. Here, we set the parameters $\delta = 1.0$ and $\gamma = 0.2$.

external physical field. We again set the intra-sub-lattice hopping strength $\gamma_A = -\gamma_B = i\gamma$ to preserve the PH symmetry. Due to the broken TR symmetry, this system can now be transformed into a Chern insulator, a TR symmetry broken topological insulator with a non-zero Chern number.

Model 1

First, we study the system with NNN intra-chain hopping of imaginary amplitude from A (or B) sites to A (or B) sites of the nearest unit cell. The schematic diagram of this model is shown in Fig. 4.5(a). The Hamiltonian of this system in the real space (lattice space) is of the form

$$\begin{aligned} H_{GN-SSH} &= H_{N-SSH} \\ &- i\gamma \sum_{n_x,n_y} \left(c^{\dagger A}_{n_x,n_y} c^{A}_{n_x+1,n_y} - c^{\dagger B}_{n_x,n_y} c^{B}_{n_x+1,n_y} - \text{h.c.} \right). \end{aligned} \tag{4.13}$$

The expression of the Hamiltonian H_{N-SSH} is given in Eq. (4.2). The above Hamiltonian in $\boldsymbol{k}$-space becomes

$$\mathcal{H}_{\boldsymbol{k}} = H_{N-SSH}(\boldsymbol{k}) + 2\gamma \sin k_x \, \sigma_z, \tag{4.14}$$

where the Hamiltonian $H_{N-SSH}(\boldsymbol{k})$ is given in Eq. (4.5). Here again we set $\gamma = 0.2$. For this case, we present the band diagrams in Fig. 4.5(b)-(e) under POBCs. The corresponding Hamiltonians are

$$\begin{aligned} &\mathcal{H}(k_x) = \mathcal{H}_{N-SSH}(k_x) + (2\gamma \sin k_x)\, \sigma_z \otimes \mathbb{1}_{Ny} \\ &\text{and} \\ &\mathcal{H}(k_y) = \mathcal{H}_{N-SSH}(k_y) - i\gamma \sum_{n_x} \left(c^{\dagger A}_{n_x} c^{A}_{n_x+1} - c^{\dagger B}_{n_x} c^{B}_{n_x+1} - \text{h.c.} \right). \end{aligned} \tag{4.15}$$

Figures 4.5(b) and 4.5(d) show energy bands for the case when the individual SSH chain is topologically trivial. On the other hand, Figs. 4.5(c) and 4.5(e) show energy bands for

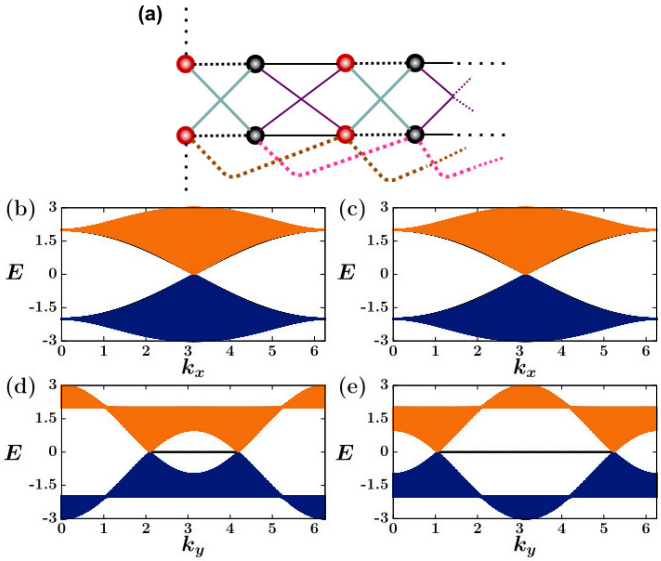

FIGURE 4.5: Model 1: The subfigure (a) shows a model which is identical to the model presented in Fig. 4.4(a). However, here the strengths of all the intra-sub-lattice hopping are imaginary (shown by the dotted bonds), breaking the TR-symmetry in the system. The other subfigures show the energy bands of the system under the POBCs. In subfigures (b) and (c), energy bands with the PBC only along x-direction are presented. Here, in (b), the individual SSH chain is topologically trivial with $\eta = -0.5$; whereas, in (c), the individual chain is topologically nontrivial with $\eta = 0.5$. Similarly, in subfigures (d) and (e), the energy bands are presented respectively for the same values of the parameter η, but here individual SSH chain with PBC is considered only along y-direction. Here, we set $\delta = 1$ and $\gamma = 0.2$.

the case when the individual SSH chain is topologically nontrivial. Here, when the PBC is considered only along x-direction, we observe that the system is gapless and the bands are touching at $k_x = \pi$. However, when the PBC is considered only along the y-direction, the two bands touch at $k_y = \pi/3$ and $k_y = 2\pi/3$. These suggest that the system has a pair of Dirac points at $(\pi, \pi/3)$ and $(\pi, 2\pi/3)$. At both the Dirac points, the term appears in this model due to the broken chiral and TR symmetries vanishes. Therefore, like the basic model, here we also do not see any opening of band gap. Moreover, this system has a pair of degenerate zero energy edge states. We have calculated the Chern number of the lower band of this system and found $C = 0$. Therefore, we now proceed to the next model, where *inter-chain* NNN hopping with imaginary amplitude is considered.

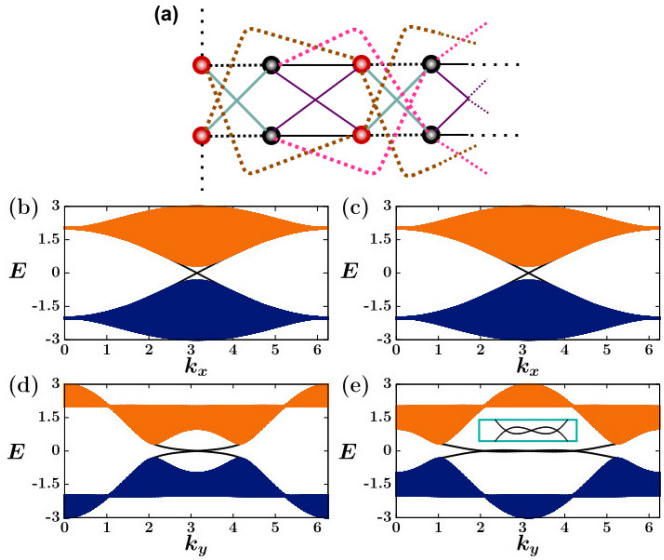

FIGURE 4.6: Model 2: In subfigures (a), two different types of inter-chain hopping terms are considered, which are shown by brown (A to A) and magenta (B to B) bonds. These intra-sub-lattice hopping strengths are imaginary numbers (represented by the dotted bonds). The imaginary hopping amplitude breaks the TR-symmetry in the system. The remaining subfigures (b)-(e) show the energy bands of this model under POBCs same as for the cases described in Figs. 4.5(b)-(e).

Model 2

The schematic representation of this model is shown in Fig. 4.6(a). Here, A (or B) sites of a SSH chain are connected to the A (or B) sites of the nearest unit cell of the neighboring SSH chain. In real space, the corresponding Hamiltonian under tight-binding condition is given as

$$\begin{aligned} H_{GN-SSH} &= H_{N-SSH} \\ &- i\gamma \sum_{n_x,n_y} \left(c^{\dagger A}_{n_x,n_y} c^{A}_{n_x+1,n_y+1} - c^{\dagger B}_{n_x,n_y} c^{B}_{n_x+1,n_y+1} - \text{h.c.} \right). \end{aligned} \tag{4.16}$$

The above Hamiltonian under PBC can be represented in the $\boldsymbol{k}$-space as

$$\mathcal{H}_{\boldsymbol{k}} = H_{N-SSH}(\boldsymbol{k}) + 2\gamma \, \sin(k_x + k_y) \, \sigma_z, \tag{4.17}$$

where, as earlier, we set $\gamma = 0.2$. For this model, we show the band diagrams in Figs. 4.6(b)-(e) under the POBCs and the corresponding Hamiltonians are

$$\begin{aligned}\mathcal{H}(k_x) = \mathcal{H}_{N-SSH}(k_x) + (\gamma \sin k_x)\ \sigma_z \otimes \sum_{n_y} \left(c^{\dagger}_{n_y} c_{n_y+1} + \text{h.c.}\right) \\ - i\,(\gamma \cos k_x)\ \sigma_z \otimes \sum_{n_y} \left(c^{\dagger}_{n_y} c_{n_y+1} - \text{h.c.}\right)\end{aligned} \tag{4.18}$$

and

$$\mathcal{H}(k_y) = \mathcal{H}_{N-SSH}(k_y) - i\gamma \sum_{n_x} \left[\left(c^{\dagger A}_{n_x} c^{A}_{n_x+1} - c^{\dagger B}_{n_x} c^{B}_{n_x+1}\right) e^{-ik_y} - \text{h.c.}\right].$$

Here, the energy bands for the case when the individual SSH chain is topologically trivial are shown in Figs. 4.6(b) and (d). On the other hand, Figs. 4.6(c) and (e) show the same for the case when the individual chain is topologically nontrivial. In Figs. 4.6(b) and (c), the edge states with single crossing is observed when the energy bands are presented for the Hamiltonian $\mathcal{H}(k_x)$. However, in Figs. 4.6(d) and (e), we respectively observe edge states with single and triple crossings (shown in the inset figure) in the energy bands of $\mathcal{H}(k_y)$. These band diagrams indicate that the system may exhibit nontrivial topological properties. We verify this by calculating the Chern number of the system and obtain $C = 1$ for both the cases. This study reveals that the system shows nontrivial topology, when the edge states cross odd number of times.

In case of the previous model, the edge states were only observed for the POBC case with the PBC along the y-direction and the OBC along the x-direction. In this model, the edge states are observed along both the directions. This suggests that this system behaves like a true 2D model with two-bands, without any effect of the stacking in a particular direction. This system is a Chern insulator with $C = 1$. These results motivate us to study the next model with A to A (or B to B) NN inter-chain hopping of imaginary amplitude along the vertical or the y-direction.

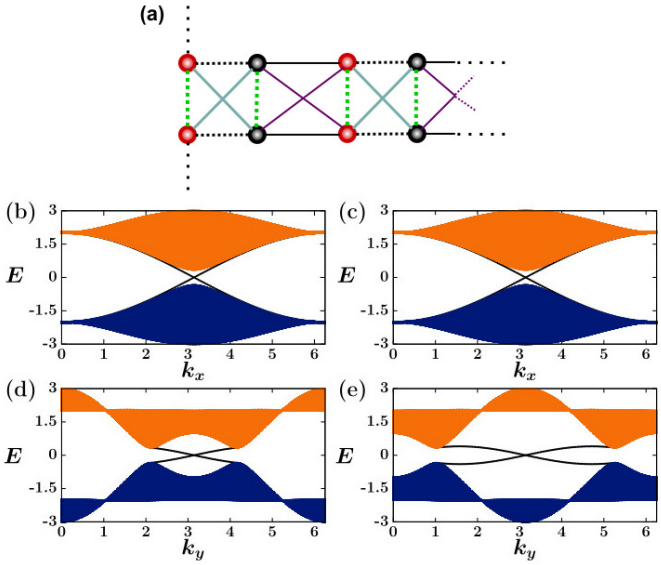

FIGURE 4.7: Model 3: The subfigure (a) shows that here we consider a different version of N-stacked SSH chains with broken chiral and TR-symmetry. This model has intra-sub-lattice hopping along the vertical direction shown by the dotted green bonds. Here, once again, the remaining subfigures show the energy bands of this model under the POBCs for the cases identical to Figs. 4.5(b)-(e).

Model 3

The schematic diagram of this system is shown in Fig. 4.7(a). The real-space Hamiltonian of this system is given as

$$\begin{aligned} H_{GN-SSH} &= H_{N-SSH} \\ &- i\gamma \sum_{n_x,n_y} \left(c^{\dagger A}_{n_x,n_y} c^{A}_{n_x,n_y+1} - c^{\dagger B}_{n_x,n_y} c^{B}_{n_x,n_y+1} - h.c. \right), \end{aligned} \tag{4.19}$$

and the corresponding Hamiltonian under the PBC is given in $\boldsymbol{k}$-space as

$$\mathcal{H}_{\boldsymbol{k}} = H_{N-SSH}(\boldsymbol{k}) + 2\gamma \sin k_y \, \sigma_z, \tag{4.20}$$

where we set $\gamma = 0.2$. The band diagrams are shown in Figs. 4.7(b)-(e) for the POBC Hamiltonians

$$\mathcal{H}(k_x) = \mathcal{H}_{N-SSH}(k_x) - (i\gamma)\,\sigma_z \otimes \sum_{n_y} \left(c^{\dagger}_{n_y} c_{n_y+1} - \text{h.c.} \right)$$

and (4.21)

$$\mathcal{H}(k_y) = \mathcal{H}_{N-SSH}(k_y) + 2\gamma \sin k_y \sum_{n_x} \left(c^{\dagger A}_{n_x} c^{A}_{n_x} - c^{\dagger B}_{n_x} c^{B}_{n_x} \right).$$

Similar to the previous cases, Figs. 4.7(b) and 4.7(d) show the energy bands, when all the individual SSH chain is topologically trivial. In Figs. 4.7(c) and 4.7(e), we have shown energy bands, where the individual SSH chain is topologically nontrivial. In all these figures, we observe edge states with single crossing only. Earlier, we have commented that Model 2 exhibits topologically nontrivial properties due to the odd number of crossings. In this model, we see single crossing of the edge states in the energy bands, which is also odd number of crossing. Therefore, we expect non-zero Chern number for this model. Our numerical calculation indeed finds $C = -1$. Like Model 2, again this model behaves like a true 2D Chern insulator with edge states along both the directions. Since, Model 2 and Model 3 show nontrivial topological properties with the Chern number of opposite signs, a natural question is whether the combination of these two models form a topologically trivial system. Thus we now study a combination of these two models.

Model 4

Finally, we consider a system having NNN diagonal hopping and NN vertical hopping among neighboring chains as depicted in Fig. 4.8(a). Moreover, here we assume the strength of both the hopping as imaginary numbers. The corresponding real-space

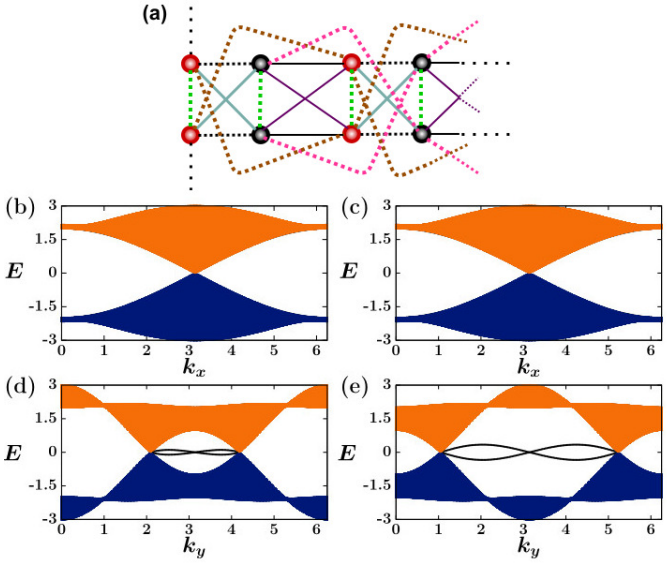

FIGURE 4.8: Model 4: The schematic diagram presented in subfigure (a) shows that this model combines Model 2 and Model 3, as presented in Figs. (4.6) and (4.7). The remaining subfigures show the energy bands of this model under POBCs, and their description is once again identical to Figs. 4.5(b)-(e).

Hamiltonian is given as

$$H_{GN-CSSH}(n_x, n_y) = H_{N-CSSH}(n_x, n_y) - i\gamma \sum_{n_x,n_y} \big(c^{\dagger A}_{n_x,n_y} c^{A}_{n_x,n_y+1} + c^{\dagger A}_{n_x,n_y} c^{A}_{n_x+1,n_y+1} - c^{\dagger B}_{n_x,n_y} c^{B}_{n_x,n_y+1} - c^{\dagger B}_{n_x,n_y} c^{B}_{n_x+1,n_y+1} - \text{h.c.} \big). \tag{4.22}$$

For this case, the $\boldsymbol{k}$-space Hamiltonian is

$$\mathcal{H}_{\boldsymbol{k}} = H_{N-SSH}(\boldsymbol{k}) + 2\gamma \left[\sin k_y + \sin(k_x + k_y)\right] \sigma_z, \tag{4.23}$$

where we set $\gamma = 0.2$. The corresponding POBC Hamiltonians are

$$\begin{aligned}\mathcal{H}(k_x) &= \mathcal{H}_{N-SSH}(k_x) + \gamma \sin k_x \, \sigma_z \otimes \sum_{n_y} \left(c^{\dagger}_{n_y} c_{n_y+1} + \text{h.c.} \right) \\ &- i\gamma(1 + \cos k_x)\sigma_z \otimes \sum_{n_y} \left(c^{\dagger}_{n_y} c_{n_y+1} - \text{h.c.} \right) \\ &\text{and} \\ \mathcal{H}(k_y) &= \mathcal{H}_{N-SSH}(k_y) + 2\gamma \sin k_y \sum_{n_x} \left(c^{\dagger A}_{n_x} c^{A}_{n_x} - c^{\dagger B}_{n_x} c^{B}_{n_x} \right) \\ &- i\gamma \sum_{n_x} \left[\left(c^{\dagger A}_{n_x} c^{A}_{n_x+1} - c^{\dagger B}_{n_x} c^{B}_{n_x+1} \right) e^{-ik_y} - \text{h.c.} \right].\end{aligned} \tag{4.24}$$

The energy bands corresponding to these Hamiltonians are presented in Figs. 4.8(b)-(e). These figures show that the energy bands are gapless. Similar to Figs. 4.4(d) and 4.4(e), the Chern number of this model is expected to be $C = 0$ due to the even number of crossings, and we have indeed found that by numerical calculation. Later, we shall also find the same by analytical calculation in Sec. 4.4. However, the presence of the edge states in this model is again indicating nontrivial topology, which is revealed in Sec. 4.5 by the calculation of the 2D Zak phase.

Here we consider all the inter-chain hopping strengths are equal. However, for the unequal strengths of the interchain NNN *diagonal* hopping (dotted red and brown lines in the figure) and the NN hopping along the vertical direction (dotted green lines in the figure), this model is topologically nontrivial with $C = \pm 1$. The sign of the Chern number is dependent on the relative strength $\Gamma \equiv \gamma_1 - \gamma_2$ of these two inter-chain hopping, where γ_1 is the inter-chain NNN diagonal hopping strength, and γ_2 is the strength of the inter-chain NN hopping along the vertical direction. When the NNN diagonal hopping strength is stronger than the NN vertical one, i.e., $\Gamma > 0$, the Chern number is $C = 1$. For the opposite case, when $\Gamma < 0$, we find $C = -1$. For both these cases, i.e., for $|\Gamma| > 0$, we expectedly observe a gap in the bulk part of the energy bands of Model 4. We have

already shown the gapless spectrum of Model 4 in Fig. 4.8 for $\Gamma = 0$, i.e. when $\gamma_1 = \gamma_2$. This implies $\Gamma = 0$ is the transition point for the topological phases with $C = 1$ to $C = -1$.

4.3.3 A summary of the results presented in this section

In all the cases discussed in this section, we observe that when the system has either NN vertical or NNN diagonal inter-chain hopping with imaginary amplitude, the systems exhibit nontrivial topology with the Chern number $C = \pm 1$. However, if we consider both these hopping in the system, we need unequal hopping strengths to get nontrivial topology with $C = \pm 1$. Furthermore, we observe that a system becomes topologically nontrivial with $C = \pm 1$ when the edge states emanating from the valence and conduction bands cross each other an odd number of times and connect the two bands. Compared with the energy band properties of the TR-symmetric systems with broken chiral symmetry, we observe according to the expectation that when the edge states cross each other an even number of times, the edge states do not connect the valence and the conduction bands. For these cases, we numerically find $C = 0$. However, in these models, the presence of the edge states indicates their nontrivial topology. In the next section, Sec. 4.4, we have calculated the Chern number of these models analytically, and these agree with the numerics. Moreover, in Sec. 4.5, the nontrivial topology of the systems with the Chern number $C = 0$ cases will be studied by the calculation of the 2D Zak phase as a topological invariant.

4.4 Chern number and phase diagram: An analytical calculation

We have extensively studied different cases of the N-stacked SSH chains. In this study, we numerically find two cases showing nontrivial topology with Chern number $C = \pm 1$.

The Chern number of the other cases was $C = 0$. However, these models have shown their nontrivial nature by exhibiting edge states. In the previous sections, we calculated the Chern number numerically as defined in Chapter 2 and given in Eq. (2.5). In this section, we focus on the analytical calculation of the Chern number. Moreover, here we have shown phase diagrams of the topological transition.

4.4.1 Chern number calculation

Instead of calculating the Chern number via Berry curvature, we follow an alternate formula to calculate the Chern number [114, 155]. Here, instead of integrating the Berry curvature over the Brillouin zone, one needs to calculate summation of a quantity at all the Dirac points D_i, and the formula is given as

$$C = \frac{1}{2} \sum_{\boldsymbol{k} \epsilon D_i} \text{sgn} \left[\partial_{k_x} \boldsymbol{h}(\boldsymbol{k}) \times \partial_{k_y} \boldsymbol{h}(\boldsymbol{k}) \right]_z \text{sgn} \left[h_z(\boldsymbol{k}) \right] . \tag{4.25}$$

Here, we assume that the Hamiltonian in the $\boldsymbol{k}$-space is of the form $\mathcal{H}_{\boldsymbol{k}} = \boldsymbol{h}(\boldsymbol{k}) \cdot \boldsymbol{\sigma}$. If we substitute $\boldsymbol{h}(\boldsymbol{k})$ of the Hamiltonians considered in this paper in the above equation, we get the expression for the Chern number as

$$C = \frac{1}{2} \sum_{\boldsymbol{k} \epsilon D_i} \left[\text{sgn}\{-\delta \sin k_y (1 + \eta - \delta \cos k_y)(1 - \cos k_x)\} \, \text{sgn}(h_z) \right]. \tag{4.26}$$

At the Dirac points, any system with PH symmetry has doubly degenerate zero-energy states. These Dirac points are calculated by setting first $h_x(\boldsymbol{k}) = h_y(\boldsymbol{k}) = 0$, and then nullify $h_z(\boldsymbol{k})$ by tuning the system parameters. Following this, we get the Dirac points for all the models at the same place in the first Brillouin zone, and these are at

$$D_1 : \left[\pi, \cos^{-1} \left(\frac{\eta}{\delta} \right) \right] \quad \text{and} \quad D_2 : \left[\pi, 2\pi - \cos^{-1} \left(\frac{\eta}{\delta} \right) \right] . \tag{4.27}$$

Symmetries	Section	Model #	$h_z(\boldsymbol{k})$	$h_z(\boldsymbol{k})\|_{\boldsymbol{k}=D_1}$	$h_z(\boldsymbol{k})\|_{\boldsymbol{k}=D_2}$	C
$\mathcal{P}, C, \mathcal{T}$	Sec. 4.2	–	0	0	0	0
$\mathcal{P}, \not{C}, \mathcal{T}$	Sec. 4.3.1	1	$2\gamma \cos k_x$	-2γ	-2γ	0
$\mathcal{P}, \not{C}, \not{\mathcal{T}}$	Sec. 4.3.2	1	$2\gamma \sin k_x$	0	0	0
		2	$2\gamma \sin(k_x + k_y)$	$\mp 2\gamma\sqrt{1-(\eta/\delta)^2}$	$\pm 2\gamma\sqrt{1-(\eta/\delta)^2}$	**+1***
		3	$2\gamma \sin k_y$	$\pm 2\gamma\sqrt{1-(\eta/\delta)^2}$	$\mp 2\gamma\sqrt{1-(\eta/\delta)^2}$	**−1***
		4(a)	$\gamma_1 = \gamma_2, 2\,[\gamma_1 \sin(k_x + k_y) + \gamma_2 \sin k_y]$	0	0	0
		4(b)	$\gamma_1 \neq \gamma_2, 2\,[\gamma_1 \sin(k_x + k_y) + \gamma_2 \sin k_y]$	$\pm 2(\gamma_2 - \gamma_1)\sqrt{1-(\eta/\delta)^2}$	$\mp 2(\gamma_2 - \gamma_1)\sqrt{1-(\eta/\delta)^2}$	**−1***

TABLE 4.1: A summary of the Chern number calculation using the analytical expression given in Eq. (4.28) is presented for all the systems studied in this paper. The extreme left column of the table shows the systems' presence and absence of different symmetries. Here, $\not{C}$ and $\not{\mathcal{T}}$ denote respectively the broken chiral and the broken TR symmetries in the system. However, for all the systems, the PH symmetry $\mathcal{P}$ is preserved. *The sign of the Chern number can also be opposite if some system parameters change the sign. Topological phases of the systems with broken PH symmetry are not summarized here.

The above relation shows that the Dirac points can exist (i.e., bands can touch each other) only when $|\delta| > |\eta|$. We observe that these Dirac points are not on the high-symmetric path [156]. Therefore, by changing a system parameter, the Dirac points can be moved anywhere in the BZ. Substituting the Dirac points in Eq. (4.26) with the condition $\left|\frac{\eta}{\delta}\right| < 1$ and assuming $\delta > 0$ without losing any generality, we obtain a simplified expression of

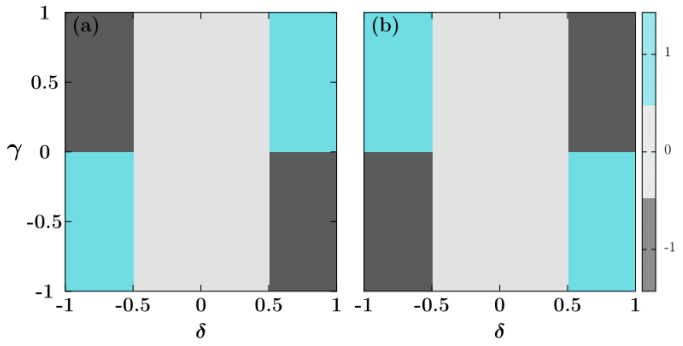

FIGURE 4.9: The subfigures (a) and (b) show the topological phase transitions in the models presented in Figs. 4.6(a) and 4.7(a), respectively. Here, the Chern number is calculated as a function of the parameters γ and δ for a fixed value of $\eta = 0.5$. Varying the parameters γ and δ, three different topological phases with $C = 0, \pm 1$ are observed.

the Chern number for our systems as

$$C = -\frac{1}{2}\mathrm{sgn}\left(\pm\sqrt{1-\frac{\eta^2}{\delta^2}}\right) \times \left(\mathrm{sgn}\left[h_z(\boldsymbol{k})\right]\Big|_{\boldsymbol{k}=D_1} - \mathrm{sgn}\left[h_z(\boldsymbol{k})\right]\Big|_{\boldsymbol{k}=D_2}\right). \tag{4.28}$$

This relation is valid for all the models discussed in this paper. Besides the constant term without any $\boldsymbol{k}$-dependency, the above expression clearly shows that the Chern number will be determined by the values of $h_z(\boldsymbol{k})$ at two Dirac points. This relation also predicts that the possible values of the Chern number are $C = 0, \pm 1$.

We have summarized the calculation of the Chern numbers using the analytical expression given in Eq. (4.28) in Table 4.1 for all the models of N-stacked SSH chains studied in Secs. 4.2, 4.3.1, and 4.3.2. We see from the table that, for the nontrivial topological cases with $C \neq 0$, a square root factor appears from the *mass* term of Eq. (4.28), which is identical to the first term of Eq. (4.28). Consequently, the square root disappears in the expression of the Chern number, and the condition $|\delta| > |\eta|$ gives $\mathrm{sgn}[1-(\eta/\delta)^2] = +1$.

4.4.2 Phase diagram

We now concentrate only on those two models, which showed nontrivial topology with $|C| = 1$, to study their topological phase transitions. Here, we fix the parameter $\eta = 0.5$, which decides the relative strength of the intra-dimer and inter-dimer hopping within an SSH chain. We then investigate the system's phase transition by tuning the system parameters (δ, γ), where these parameters decide the hopping strength between two neighboring SSH chains. In Figs. 4.9 (a) and (b), we present the phase-diagrams on the parameter space (δ, γ) of the Model 2 and 3 of Sec. 4.3.2. Here we also relax any restriction on the values of (δ, γ): these parameters can be both positive and negative.

Since we set $\eta = 0.5$, the Dirac points can only exist if $|\delta| \geq 0.5$. Consequently, when $|\delta| < 0.5$, the systems should show a trivial topology with $C = 0$. In Fig. 4.9, we indeed see for both the systems that the Chern number $C = 0$ in the region $|\delta| < 0.5$ of the parameter space and this region is highlighted by light-grey color. The phase diagrams show that, for these two models, the transition from trivial to nontrivial occurs when $\delta \geq \eta$. These figures also reveal that the topological properties of the two models are complementary to each other, i.e., wherever in the parameters space, the Chern number of one system is C, and the Chern number of the other system is $-C$. The parameter regions with nonzero Chern numbers are shown using cyan and grey colors.

4.5 Cases of the nontrivial topology with the Chern number $C = 0$

This section focuses on the $C = 0$ cases observed in Secs. 4.2, 4.3.1, 4.3.2. The basic model, which was considered at the beginning, is anisotropic. The anisotropy appears due to the independent intra-chain and inter-chain (both vertical and diagonal inter-chain bonds) hopping strength. This type of 2D anisotropic model can show nontrivial topological properties even though the Chern number of a system is *zero* [157]. For the anisotropic 2D model with $C = 0$, the topological invariant is the 2D Zak phase. The 2D Zak phase is nothing but the 1D Zak phase with fixed values of momenta which is defined as

$$Z_{x/y,m}(k_{y/x}) = \int_{BZ} A_{x/y,m}(k_x, k_y)\, dk_{x/y}, \tag{4.29}$$

where m represents the band indices for lower (-) and upper band (+). The Berry connection $A_{x/y,m}(k_x, k_y)$ is defined after the equation 2.5.

This investigation begins with the model presented in Sec. 4.2. This model has all three previously mentioned fundamental symmetries. For this model, we find the 2D

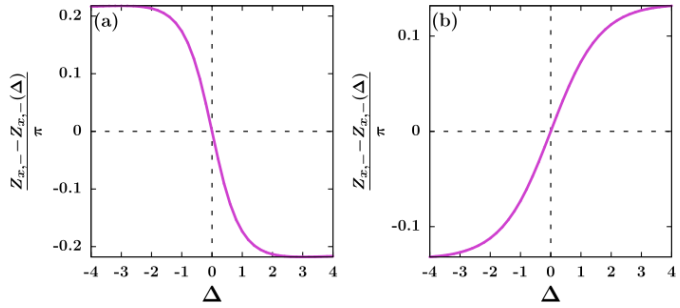

FIGURE 4.10: The difference between the 2D Zak phases of the basic model (Fig. 4.1) and the chiral symmetry broken system [Fig. 4.4(a)] is shown as a function of the NNN hopping amplitude $\Delta = 2\gamma$. In subfigures (a) and (b), the individual SSH chain with trivial and nontrivial topology is considered, respectively. These figures demonstrate the presence of the fractional Zak phase for the chiral symmetry broken N-stacked SSH model [Fig. 4.4(a)]. The Zak phases $Z_{x,-}$ and $Z_{x,-}(\Delta)$ are calculated at $k_y = \pi$.

Zak phase $Z_{x,-}(k_y) = -\pi$, provided the k_y values are within the range given in Eq. (4.9). However, for $k_x = \pi$, the 2D Zak phase $Z_{y,-}(k_x) = 0$. These values of the Zak phase are the same for both trivial and nontrivial individual SSH chains.

We then study the model presented in Sec. 4.3.1 that is an N-stacked SSH model with broken chiral symmetry. Because of the existence of the non-zero h_z, the pseudo-spinors move in the z-direction from the equatorial plane (represented by $h_z = 0$) of the Bloch sphere. This aberration of results is reflected in the non-quantized Zak phase, i.e., the Zak phase is not an integer multiple of π. This is referred to as the fractional Zak phase [158–161]. The presence of the fractional Zak phase has also been experimentally

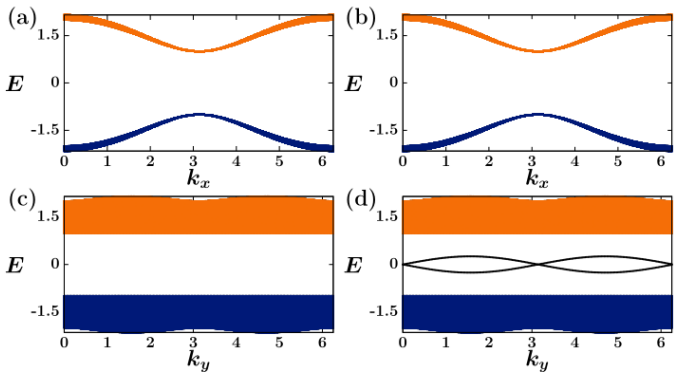

FIGURE 4.11: The band diagram is presented for the model shown in Fig. 4.8(a), where the strengths of the diagonal NNN and the vertical hopping are equal. In subfigures (a) and (b), we set $\eta = -0.5$ and 0.5 so that the individual SSH chain will be trivial and nontrivial, respectively. Here, we choose $\delta = 0$ for both the cases.

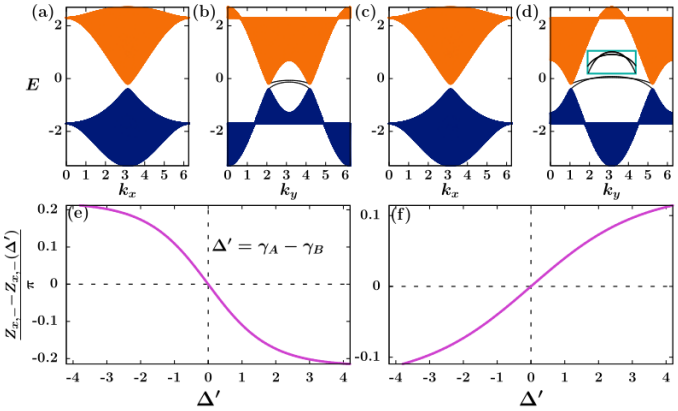

FIGURE 4.12: The energy bands are shown under POBCs of the system presented in Sec. 4.3A, but now with the broken PH symmetry. Since here both chiral and PH symmetries are broken, the energy bands are asymmetric. The Chern number is $C = 0$ in this case. Subfigures (a) and (b) present the results when the individual SSH chain is trivial ($\eta = -0.5$); whereas subfigures (c) and (d) are shown for the case when the individual SSH chain is non-trivial ($\eta = 0.5$). Here we set the parameter $\delta = 1.0$ for both the cases. Their corresponding deviation from the Zak phase of the basic model is presented respectively in subfigure (e) and (f). In subfigures (a)-(d), we set the hopping amplitude $\gamma_A = 0.2$ and $\gamma_B = 0.1$, which break the PH and inversion symmetries in the system.

observed for a chiral symmetry broken 1D TI [158]. For our model, we demonstrate in Fig. 4.10 the deviation of the Zak phase from the quantized to non-quantized values as a function of the NNN hopping amplitude $\Delta = 2\gamma$, the parameter which breaks the chiral symmetry. In Fig. 4.10(a), we show the deviation of the Zak phase for the case when the individual SSH chain is trivial, whereas Fig. 4.10(b) shows the same deviation when the individual SSH chain is nontrivial. The nature of the deviation of the Zak phase for these two cases is the opposite. According to our expectation, for both cases, when the parameter $\Delta \to 0$, the Zak phase approaches $-\pi$, a quantized value. Moreover, we also notice that the Zak phase saturates when $|\Delta| \geq 4$. However, in this parameter region, the NNN hopping strength becomes stronger than the NN hopping.

We now analyze the $C = 0$ cases discussed in Sec. 4.3.2. Here, both chiral and TR symmetries are broken. This section considers two models with $C = 0$: Model 1 and Model 4. The energy bands of Model 1 are similar to the basic model. Consequently, the Zak phase of Model 1 is equals the basic model. In the case of Model 4, when the inter-chain coupling parameters are equal (i.e., $\gamma_1 = \gamma_2 = \gamma$), the system exhibits $C = 0$.

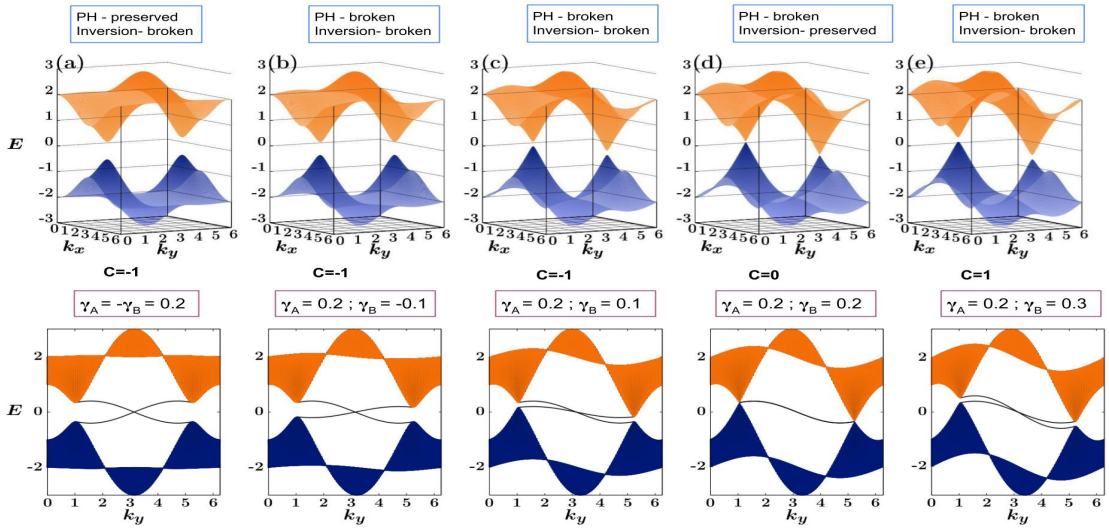

FIGURE 4.13: The energy bands are shown under POBCs with the broken PH symmetry of *Model 3* discussed in Sec.4.3B. In the upper panel, energy E is plotted as a function of the momenta k_x and k_y for different values of the intra-sub-lattice hopping amplitudes γ_A and γ_B for *Model 3* (discussed in Sec. 4.3B). The corresponding band diagram under POBCs with periodic boundary condition along y-direction are shown in the lower panel. As we gradually change the amplitudes γ_A and γ_B, the energy bands become asymmetric. Although there is a topological phase transition point at $\gamma_A = \gamma_B = 0.2$, where the system has inversion symmetry; but the PH symmetry is still broken at this point. Around this transition point, the system makes topological phase transition from a phase with Chern number $C = -1$ to a phase with $C = 1$. Here we set the dimerization constant $\eta = 0.5$ and hence the individual SSH chain is topologically nontrivial.

According to Ref. ([157]), the nontrivial topology of this anisotropic system appears through the presence of gap-edge states, which are completely isolated from the bulk part. In Fig. (4.11), similar gap-edge states in the whole BZ are also observed in our model. Here again, we consider two cases: all the SSH chains are topologically nontrivial, and all are trivial. The respective energy band diagrams are shown in Figs. 4.11(a)-(d). In these cases, we set $\delta = 0$. We show in Fig. 4.11(d) that the system has gap-edge states. Therefore, we concentrate only on this case. We find the 2D Zak phase $Z_{x,-}(k_y) = -\pi$, provided the values of k_y lie within the range given in Eq. (4.9). However, for $k_x = \pi$, the 2D Zak phase $Z_{y,-}(k_x) = 0$. Moreover, the area covered by the edge states in the BZ decreases after increasing δ, which is shown in Fig. 4.8(d)-(e).

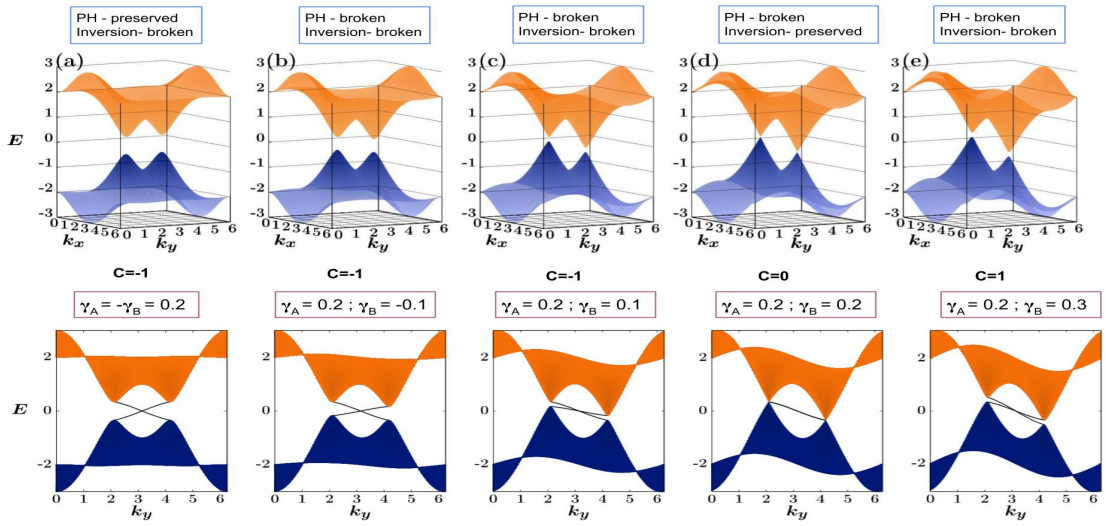

FIGURE 4.14: The same results are presented as in Fig. 4.13, but here we set the dimerization parameter $\eta = -0.5$ to make the individual SSH chain topologically trivial.

4.6 Systems with broken particle-hole symmetry

We now discuss the PH symmetry broken version of the models presented in Secs. 4.3A and 4.3B. In Fig. 4.12, the energy bands are presented for the PH symmetry broken version of the model presented in Sec. 4.3A under POBCs. Here, subfigures 4.12(a) and 4.12(b) are plotted when the individual SSH chain is trivial; whereas subfigures 4.12(c) and 4.12(d) are presented for the cases, when the individual SSH chain is nontrivial. In order to break the PH symmetry in the model, we set the A to A hopping amplitude γ_A and the B to B hopping amplitude γ_B unequal. Here, we particularly consider $\gamma_A = 0.2$ and $\gamma_B = 0.1$. Our results remain qualitatively invariant for any other pairs of unequal values of these above mentioned hopping parameters. The broken PH symmetry in the model leads to the asymmetric energy bands. In this case, we obtain the Chern number $C = 0$ as we obtained for the model presented in Sec. 4.3A, where only chiral symmetry was broken. Again like the chiral symmetry broken case, here we obtain the fractionalized Zak phase for this case. For the equal hopping amplitudes $\gamma_A = \gamma_B = 0.2$, the Zak phase gets quantized due to the preserved inversion symmetry. In order to preserve the

inversion symmetry, the Hamiltonian should satisfy the following condition:

$$\mathcal{R}^{-1}\,\mathcal{H}(k_x, k_y)\,\mathcal{R} = \mathcal{H}(-k_x, -k_y), \tag{4.30}$$

where $\mathcal{R}$ represents the inversion operation. The deviations of the Zak phase from the Zak phase of the basic model with all the symmetries preserved are shown in Fig. 4.12(e) (individual SSH is trivial) and (f) (individual SSH is nontrivial). Here the deviation of the Zak phase is plotted as a function of the difference Δ' between two intra-sub-lattice hopping amplitudes, i.e., $\Delta' = \gamma_A - \gamma_B$.

We then investigate the effect of the PH symmetry breaking on the models presented in Sec.4.3B. Here, we present only *Model 3* of Sec. 4.3B, because the other models of Sec. 4.3B show qualitatively similar behavior. The band diagram for the *Model 3* under full PBC and POBCs are shown in Figs. 4.13 and 4.14. The subfigures 4.13(a)-(e) show the band diagrams corresponding to the nontrivial SSH chain; and on the other hand, the subfigures 4.14(a)-(e) show the band diagrams corresponding to the trivial SSH chain. In the upper panel, the band diagrams are plotted under full PBC and their corresponding band diagrams under POBCs are shown in the lower panel. Here, we observe a topological phase transition from the topological phases with the Chern number $C = -1$ to $C = +1$ due to the interplay of the breaking and preserving of the PH and the inversion symmetries. The topological phase transition occurs in the system when the system has inversion symmetry with equal hopping amplitudes $\gamma_A = \gamma_B = 0.2$.

4.7 Experimental aspects of N-stacked SSH model

We now discuss the possible experimental realizations of the N-stacked SSH model. In order to construct the N-stacked SSH model, we first need to construct single 1D SSH chain. Recent discoveries suggest that the SSH chain could be realized in photonics

[162] and electric circuits [163]. In photonics, one-dimensional TIs can be engineered using an array of coupled optical waveguides [70, 162, 164, 165]. In Ref. [162], to design a 1D SSH chain, all the waveguides are kept at the same distance from each other and an auxiliary waveguide is placed next to every other waveguide. These auxiliary waveguides strengthen the coupling between the two waveguides that are same distance apart and thus simulate the intra-cell and inter-cell hopping in the 1D SSH chain. The array of optical waveguides can be fabricated using a femtosecond laser writing technique [162, 164, 166]. Moreover to design the SSH chain in the electric circuits, each sub-lattice is constructed from a combination of inductors and capacitors.

Similarly using the optical waveguides, the E-SSH model (mentioned in the Introduction section) with broken chiral symmetry can also be realized [165]. This fabrication uses photon propagation along a binary waveguide lattice placed in a zig-zag geometry [165]. In this experiment, the hopping is considered in such a manner that the system breaks chiral symmetry, but possesses inversion symmetry. The inversion symmetry in the system can be preserved by keeping the equal hopping amplitudes between A to A sub-lattice and B to B sub-lattice. This design is helpful in breaking the symmetries of the SSH chain. It is also studied that 2D photonic crystals with broken TR symmetry can be realized using photonic meta-materials [167].

Recent studies also have found that a N-stacked SSH chain can also be fabricated using magneto-mechanical meta-material [168] and electric circuits [154, 163]. In [168], the N-stacked SSH model is realized with dislocation defects, where the 1D SSH chain is designed using mechanical resonators. These mechanical resonators are coupled to each other through their magnetic interaction [168, 169]. Each resonator is like a sub-lattice and a unit cell is made of two coupled adjacent resonators. A N-stacked SSH model is designed when this setup is aligned in the x-direction and kept periodically along the y-direction.

Here we propose that a N-stacked SSH model can be fabricated by designing 1D SSH chain using the techniques mentioned above and place them periodically in the transverse direction of the SSH chains. The chiral symmetry can be broken following the method given in [165]. Moreover, imaginary hopping can be introduced (to break the TR symmetry) by applying a magnetic field-like gauge field in the direction perpendicular to the plane of the 2D lattice. Since the chiral, PH, and inversion symmetries are dependent on the hopping amplitudes from A to A and from B to B sub-lattices, these symmetries can be broken by properly placed the waveguides.

4.8 Summary

In this paper, we have proposed a 2D SSH model constructed by stacking N number of SSH chains with coupling only between two neighboring SSH chains. Here, we have considered two versions of the model determined by the topological property of the individual SSH chain: (1) all the chains are topologically trivial with the winding number $w = 0$; and (2) all the chains are topologically nontrivial with $w \neq 0$. Depending on the intra-chain parameters (intra-dimer and inter-dimer strengths) and the inter-chain coupling strength, the N-stacked SSH chains can be in three phases: topologically trivial, topological semimetal, and weak topological insulator. We have observed all these phases in this model by systematically breaking the symmetries.

We start the analysis with a basic model of the N-stacked SSH chains with all the fundamental symmetries (chiral, TR, and PH) preserved. Depending on the topological property of the individual chain, the basic model shows both topologically trivial and nontrivial nature. However, for both the cases, the Chern number of this model $C = 0$. The nontrivial topology of this model is identified from the presence of the edge states. We then start analyzing the role of different symmetries on the topology of this model.

First, we break the chiral symmetry by introducing intra-sub-lattice hopping in the system. This is done by allowing NNN hopping within an SSH chain. The introduction of this new hopping leads to a mass-like term, and consequently, it opens up the band gap. This model also shows the Chern number $C = 0$. However, edge states are still present in this model, which indicates its nontrivial topology.

Following Haldane, we have broken the TR-symmetry by introducing intra-sub-lattice hopping strength with imaginary amplitude. For this case, we have studied four different models. Only two models (Model 2 and Model 3) have shown nontrivial topology with $C = \pm 1$. The other models, Model 1 and Model 4 have the Chern number $C = 0$, but the presence of edge states in theses models indicate their nontrivial topology. However, Model 4 shows the nontrivial topology with a nonzero Chern number when two different types of inter-chain hopping strengths are considered unequal. In all these cases, we have preserved the PH symmetry in all the models. Therefore, we could apply a recently proposed analytical formulation to calculate the Chern number. This calculation agrees well with the models' numerically observed topological properties. We have presented phase diagrams of these systems that showed nontrivial topology with nonzero Chern numbers. Thus we have found a recipe to prepare a Chern insulator from a weak TI with $C = \pm 1$ and cataloged the topological phases of the N-stacked SSH chains by the systematic breaking of symmetries.

Next, we have concentrated separately on studying the nontrivial topological cases with $C = 0$. We have calculated the 2D Zak phase as a topological invariant for these cases. Interestingly, here we have observed two different behaviors in the 2D Zak phase: quantized Zak phase, which is equal to the integer multiples of π, and fractional Zak phase when this is not an integer multiple of π. The former is observed in the basic model (discussed in Sec. 4.2), and also in chiral and TR symmetry broken Model 1 and Model 4 (discussed in Sec. 4.3B). The latter is observed when the chiral symmetry is broken in

the basic model (discussed in Sec. 4.3A). For this model, we have extensively discussed how the breaking of the chiral symmetry affects the fractional nature of the Zak phase.

Finally, we have presented the results for the system with broken PH symmetry for the two cases: with broken chiral symmetry, and with broken chiral as well as the TR symmetry. The breaking of the PH symmetry introduces an asymmetry in the hopping terms of the system, which exhibits in the energy bands and also in the phase transition around the point where the system preserves inversion symmetry. We have also discussed possible experimental realizations of the N-stacked SSH model.

4.9 Outlook

Three-dimensional weak topological insulators (WTIs) formed by stacking 2D QSH layers have been studied extensively, both theoretically and experimentally. These studies also consider the impact of breaking of some of the fundamentals and translational symmetries [170–176, 176–186]. However, compare to 3D WTIs, there are relatively a few theoretical and experimental studies available on the 2D WTIs constructed from the stacked 1D TIs [143–145, 154, 163, 168]. In this extensive paper, we have introduced five different models (presented in Secs. 4.3A and 4.3B) which can be studied further with the broken translational symmetry also.

As a future perspective, one can construct a full-fledged three-dimensional layered structure by extending the N-stacked SSH model. In its 3D version of the N-stacked SSH model, one can place all the N-stacked layers periodically along the z-direction. This extension of 1D TIs to 3D WTIs will also exhibit following exotic topological properties as observed in the 3D layered QSH system: such as non-linear QHE, spin-polarization, Quantum anomalous layer Hall effect, QSH effect with half integer, etc. [179–182]. This work is useful in choosing a model, depending on the requirement of the study, which either preserve or break the fundamental symmetries. For this 3D extension, one can

also look into the macroscopic electric, magnetic and optical properties via symmetry breaking.

5

Floquet version of N stacked SSH model using circularly polarized light

---

The content of this Chapter has been submitted to the Physical Review B as Aayushi Agrawal and J.N. Bandyopadhyay.

In the upcoming two Chapters, we use a new notation Ω *for the driving frequency.*

5.1 Introduction

Floquet engineering is becoming a vast area of research, where a desired solid state system is synthesized by periodic driving. A primary goal of this research area is to design a periodic driving protocol to quickly introduce or enhance desired exotic properties in a given system by very controlled way [187]. In the realm of topological insulators (TIs), periodically driven TIs or Floquet TIs have been studied extensively. Periodic driving introduces many interesting features in the TIs, which may not be possible to realize by

any static means [50, 67, 93, 109, 188–191]. These periodically driven systems can be realized experimentally by ultracold atoms in optical lattices [66, 192].

The quasi-nD systems, engineered by stacking numerous nD systems, came into light after the discovery of weak topological insulators (WTIs). The WTIs were discovered in quasi-2D quantum spin Hall systems (QSH) in which 2D QSH layers were stacked and formed a 3D layered structure [146, 147]. A few studies on quasi-2D systems, such as 3D layered structure of graphene and topological crystalline insulators (TCI) have been conducted [47–49, 193–198]. The recent literature focuses extensively on different 2D materials, only a very little attention is paid to the quasi-1D systems form by a systematic stacking of numerous identical 1D systems. Recently, present authors rigorously study an N number of stacked SSH chains [212]. Similarly, some studies have investigated topological properties of another quasi-1D model, an extended Su-Schrieffer-Heeger model (E-SSH) [70, 199]. The E-SSH model is a 1D SSH chain where all the hopping amplitudes are modulated by a cyclic parameter θ and this cyclic parameter is considered as an another synthetic dimension. In fact, the Floquet version of the SSH chain, the simplest 1D TI which displays interesting properties [106, 118, 119, 200]. An intriguing feature of the static E-SSH model is that the phase diagram of this system resembles the phase diagram of the Haldane model. The interlink between the E-SSH model and N stacked SSH model is that by promoting θ to an actual dimension, one can obtain N stacked SSH model. The E-SSH model is also studied with different periodic drivings such as Dirac-delta kickings and sinusoidal driving [119, 199].

Through Floquet, the quasi-2D system of N stacked Graphene layers is also explored where circularly polarized light (CPL) is used as an external periodic drive and topological phases with the high Chern number (C) are observed [48]. The CPL is widely recognised for breaking the time-reversal symmetry [102, 122, 201–206]. As a result, it creates a new gap at the band touching points and the system harbors quantum Hall effect without using

any external magnetic field or creating Landau levels [12]. Furthermore, the CPL can be used to detect optical chirality, thermoelectric transport, photo-voltage, the dynamical Hall effect, and as a probe for high harmonic generation [207–211].

In this work, we aim to induce new Floquet topological phases through CPL in the N stacked SSH chains model. As per our knowledge, periodically driven WTI is not studied in literature. Here, we study a 2D WTI under periodic driving. This undriven N stacked SSH chains follows all the three fundamental symmetries (chiral, particle-hole, and time-reversal), which hosts nontrivial topology but with Chern number $C = 0$. In the undriven case, two possible construction were addressed: N stacked SSH model where each SSH chain is topologically trivial (winding number, $w = 0$), and each SSH chain is nontrivial ($w = 1$) [212]. As we turn on the driving, these two cases exhibit different topological phases. This model has an interesting feature beacuse there exist a coupling term between the momenta k_x and k_y which makes the system complex and distinct from various other well-studied 2D systems [18, 213]. At the low energy limit, near the band touching points, the dispersion relation of this system becomes quadratic with a $k_x k_y$ like coupling term.

In various studies, it has been observed that, in case of the linear dispersion, that the band crossing points or Dirac points are stable against any small perturbation [12, 214–216]. However, for the case of the quadratic dispersion near the band crossing points or semi-Dirac points are unstable for the small perturbation: either a gap is opened up or splits into two Dirac points [204, 217]. The emergence of the semi-Dirac point requires linear dispersion in one direction, and quadratic dispersion in the other direction. This non-linear dispersion encourages to investigate the N stacked SSH chains under the influence of linearly polarized light LPL along the $x-$ and y-directions.

This paper is organized as follows: In Sec. 5.2, we briefly discuss the static Hamiltonian. In the next section, Sec. 5.3, we discuss the Floquet formalism and the periodically

driven Hamiltonian which uses the exact Floquet replica method. In the next section, Sec. 5.4, we calculate the low-energy Hamiltonian to show a signature of hierarchy in Floquet band gaps. In Sec. 5.5, we demonstrate the role of linearly polarized light on the N stacked SSH model. Finally, we summarize in Sec. 5.6.

5.2 Static Hamiltonian

We consider a static N stacked SSH chain model, which is composed of an N number of SSH chains stacked in the vertical direction [212]. In real space, the mathematical expression for this static system is given as

$$\begin{aligned} H_{N-SSH} = (1-\eta)\sum_{n_x,n_y} c^{\dagger A}_{n_x,n_y} c^{B}_{n_x,n_y} + (1+\eta)\sum_{n_x,n_y} c^{\dagger A}_{n_x+1,n_y} c^{B}_{n_x,n_y} \\ + \frac{\delta}{2}\sum_{n_x,n_y}\left[c^{\dagger A}_{n_x,n_y} c^{B}_{n_x,n_y+1} + c^{\dagger A}_{n_x,n_y+1} c^{B}_{n_x,n_y}\right] \\ - \frac{\delta}{2}\sum_{n_x,n_y}\left[c^{\dagger A}_{n_x+1,n_y} c^{B}_{n_x,n_y+1} + c^{\dagger A}_{n_x+1,n_y+1} c^{B}_{n_x,n_y}\right] + h.c. \end{aligned} \tag{5.1}$$

Here δ is the hopping amplitude between the inter-sublattices of neighboring SSH chains; and η is the dimerization constant of the individual SSH chain. The parameter η can be negative or positive values which results in trivial or nontrivial SSH chain. To illustrate the energy spectrum and topological properties, we write the Hamiltonian in the quasimomentum space (or $\boldsymbol{k}$-space), which is given as

$$H_{N-SSH}(\boldsymbol{k}) = \boldsymbol{h}\cdot\boldsymbol{\sigma} \tag{5.2}$$

$$\begin{aligned} h_x(\mathbf{k}) =& [(1+\cos k_x) + (1-\cos k_x)\,(\delta\cos k_y - \eta)] \\ h_y(\mathbf{k}) =& [(1+\eta) - \delta\cos k_y]\,\sin k_x \end{aligned}$$

In our previous study [212], we found that breaking of chiral and time-reversal symmetries are essential for this static system to be a Chern insulator (CI). However, this static system follows all three fundamental symmetries, and shows topological properties even when the Chern number $C = 0$. For this case, its topological property is determined by nonzero 2D Zak phase $Z(k_y) = -\pi$. This study also revealed that the topological properties of this system are not dependent on the topological properties of the individual SSH chain. We now discuss this model under the periodic driving with CPL. It is well-known that the CPL breaks the chiral as well as the TR symmetry in the system, and this leads to nontrivial topological properties in the system with non-zero Chern number.

5.3 Driven Hamiltonian

We now apply a laser field whose vector potential $\boldsymbol{A}(t)$ has the form

$$\boldsymbol{A}(t) = (A_{0x}\cos\Omega t, A_{0y}\sin\Omega t)$$

with it satisfies $\boldsymbol{A}(t+T) = \boldsymbol{A}(t)$, where T is the time-period of the driving, and consequently the driving frequency $\Omega = 2\pi/T$. Here, A_{0x} and A_{0y} are the components of the vector potential along x and y direction, respectively. If we set $A_{0x} = A_{0y} = A_0$, the laser field will be the CPL. The LPL is a special case of this laser field, when it has a form either $\boldsymbol{A}(t) = (A_{0x}\cos\Omega t, 0)$ or $\boldsymbol{A}(t) = (0, A_{0y}\cos\Omega t)$. This driving is induced in the system by the Peierls substitution, which modifies the form of the quasi-momenta k_x and k_y as

$$k_x(t) \longrightarrow k_x + A_x(t)\,;\; k_y(t) \longrightarrow k_y + A_y(t)$$

The form of the time-periodic Hamiltonian in the $\boldsymbol{k}$-space reads

$$\begin{aligned} H_{N-SSH}(\mathbf{k},t) =& [(1+\cos k_x(t)) + (1-\cos k_x(t)) \\ & \times (\delta \cos k_y(t) - \eta)]\sigma_x \\ & + [(1+\eta) - \delta \cos k_y(t)]\ \sin k_x(t)\, \sigma_y \end{aligned} \tag{5.3}$$

In order to solve the time-periodic equation, we use the Floquet replica method and calculate the effective Hamiltonian, which is an infinite dimensional matrix in the frequency space.

We write the Fourier components $H^{(m)}$ for the N-stacked SSH model in the form as

$$H^{(m)} = \boldsymbol{d}^{(m)} \cdot \boldsymbol{\sigma}.$$

The driving modifies the undriven part as follows

$$H^{(0)}_{N-SSH} = \boldsymbol{d}^{(0)}_{N-SSH} \cdot \boldsymbol{\sigma} \tag{5.4a}$$

where

$$\begin{aligned} \left(d^{(0)}_{N-SSH}\right)_x =& \ (1-\eta) + (1+\eta)\ \cos k_x\, J_0(A_0) + \delta\ \cos k_y\, J_0(A_0) \\ & - \delta\ \cos k_x\ \cos k_y\, J_0^2(A_0) \end{aligned} \tag{5.4b}$$

$$\left(d^{(0)}_{N-SSH}\right)_y = \ (1+\eta)\ \sin k_x\, J_0(A_0) - \delta\ \sin k_x\ \cos k_y\, J_0^2(A_0); \tag{5.4c}$$

where J_0 is the Bessel function of the first kind with zeroth order.

In order to calculate the other non-zero Fourier components, we choose the driving amplitude A_0 such that the Bessel functions contribute only upto an order of A_0^2. The higher order Fourier components are neglected, because we assume that the amplitude

A_0 is small. Thus, the effective Hamiltonian H_{eff} have only $H^{(1)}$ and $H^{(2)}$ Fourier components, which are given as

$$H^{(1)}_{N-SSH} = \boldsymbol{d}^{(1)}_{N-SSH} \cdot \boldsymbol{\sigma} \tag{5.5a}$$

where

$$\begin{aligned}\left(d^{(1)}_{N-SSH}\right)_x = &-(1+\eta)\,\sin k_x\, J_1(A_0) + i\,\delta \sin k_y\, J_1(A_0) \\ &-\delta\left\{-\sin k_x\,\cos k_y + i\,\cos k_x\,\sin k_y\right\} J_0(A_0)\, J_1(A_0)\end{aligned} \tag{5.5b}$$

$$\begin{aligned}\left(d^{(1)}_{N-SSH}\right)_y = &(1+\eta)\,\cos k_x\, J_1(A_0) \\ &-\delta\left\{\cos k_x\,\cos k_y + i\,\sin k_x\,\sin k_y\right\} J_0(A_0)\, J_1(A_0);\end{aligned} \tag{5.5c}$$

and

$$H^{(2)}_{N-SSH} = \boldsymbol{d}^{(2)}_{N-SSH} \cdot \boldsymbol{\sigma} \tag{5.6a}$$

where

$$\begin{aligned}\left(d^{(2)}_{N-SSH}\right)_x = &-(1+\eta)\,\cos k_x\, J_2(A_0) + \delta\,\cos k_y\, J_2(A_0) \\ &+ i\,\delta \sin k_x\,\sin k_y J_1^2(A_0)\end{aligned} \tag{5.6b}$$

$$\left(d^{(2)}_{N-SSH}\right)_y = -(1+\eta)\,\sin k_x\, J_2(A_0) - i\,\delta\,\cos k_x\,\sin k_y J_1^2(A_0). \tag{5.6c}$$

Here, J_1 and J_2 are the Bessel functions of the first kind.

Floquet energy bands corresponding to the Hamiltonian given in Eq. (5.3) are shown in Fig 5.1. In subfigure 5.1(a) and 5.1(c), we consider each SSH chain is topologically trivial ($\eta = -0.5$). Subsequently, in subfigure 5.1(b) and 5.1(d), we consider individual SSH chain as nontrivial ($\eta = 0.5$). The Floquet bands are shown for cylindrical geometry with axis along x-direction or y-direction. Here, axis along x-direction (or y-direction)

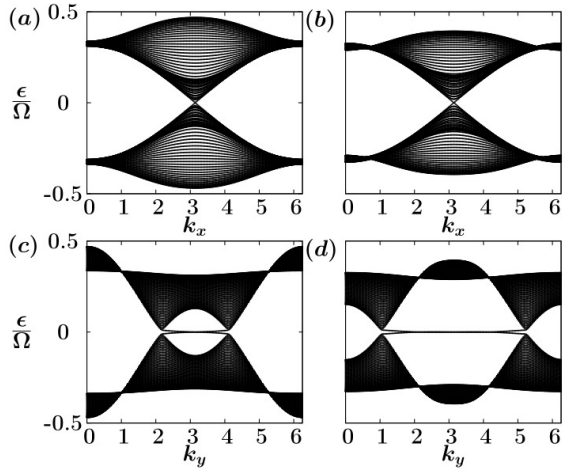

FIGURE 5.1: Quasienergy bands for the periodically driven N stacked SSH chains are shown as a function of k_x and k_y in cylindrical geometry. In subfigures (a) and (c), all the SSH chains are considered trivial ($\eta = -0.5$), while in subfigures (b) and (d), all the SSH chains are nontrivial ($\eta = 0.5$). Here, when the quasienergy bands are shown as a function of k_x (k_y), then this suggests that the PBC is considered along x-direction (y-direction), and the OBC is considered along the other direction. In both the cases, the driving generates new Floquet topological phases with Chern number $C = -1$, and this is depicted by the edge states. For both the plots, we fix the parameters as $\delta = 1.0$, $A_0 = 0.5$ and $\Omega = 6.0$.

means, we consider periodic boundary condition (PBC) along y-direction (or x-direction), and open boundary condition (OBC) along the x-direction (or y-direction). These Floquet bands are presented in the high-frequency regime with $\Omega = 6.0$ and the driving amplitude $A_0 = 0.5$. In both the case, we obtain nontrivial topology with $C = -1$, which was topologically trivial with $C = 0$ in the undriven case [212]. With the application of the CPL, the N stacked SSH model is transformed into a Chern insulator. In the undriven case, we found that the topological properties remained unchanged irrespective of underlying SSH chains are topologically trivial or nontrivial. In both cases, we observe qualitatively similar characteristics for this specific driving amplitude and frequency. To illustrate the complete behavior of the topological properties in driving parameter space, we present a phase diagram in the next section.

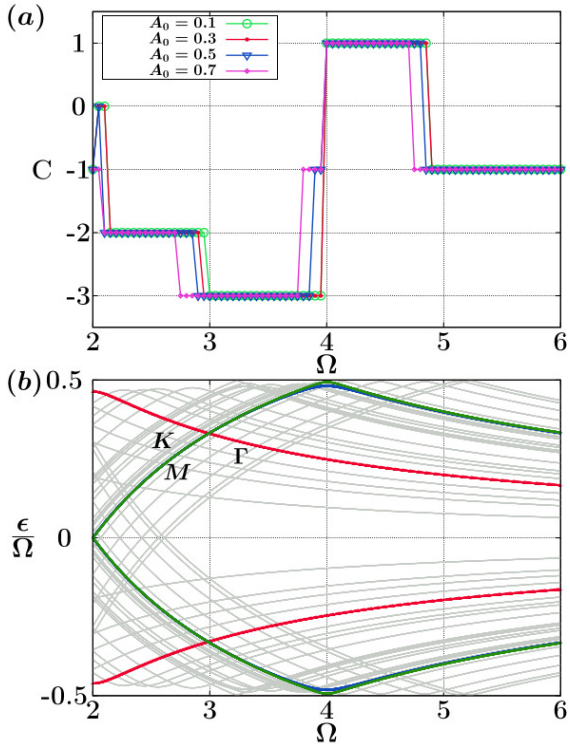

FIGURE 5.2: Different topological phases with different Chern numbers C are shown as the function of driving frequency Ω and driving amplitude A_0. In this case, we set $\eta = -0.5$ and hence the individual SSH chain is topologically trivial. Here, we consider 9 photon sectors in the Hamiltonian to get the desired convergence. In subfigure (b), the Floquet bands are plotted in FBZ along the high symmetric path. Here, Γ is (π, π), K is $(2\pi, \pi)$ and M is $(2\pi, 2\pi)$.

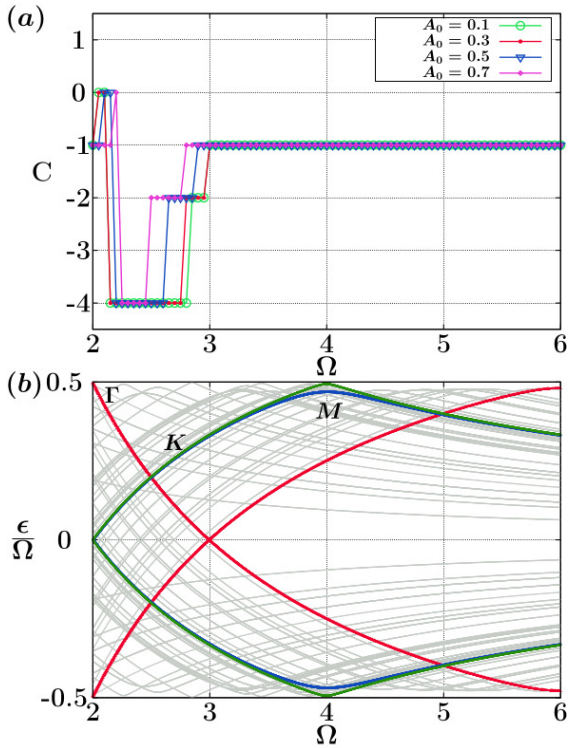

FIGURE 5.3: The results presented here is similar to Fig. 5.2, but here we consider individual SSH chain as topologically nontrivial.

5.3.1 Phase diagram

In this section, we demonstrate two phase diagrams depending on the topological property of the individual SSH chain. The phase diagrams are plotted in the driving parameter space of amplitude (A_0) and frequency (Ω) to illustrate various topological phases. The result for the case when the individual SSH chain is topologically trivial is presented in Fig. 5.2(a), whereas Fig. 5.3(a) shows the result when the individual SSH chains are topologically nontrivial. In these phase diagrams, we show the sum of the Chern number of all the Floquet bands below $\epsilon = 0$ as a function of the driving frequency Ω for four different values of driving amplitudes $A_0 = 0.1, 0.3, 0.5$ and 0.7. As stated in Ref. [218], in frequency domain, one can calculate the number of chiral edge states in a particular gap by summing the Chern number of all the Floquet bands below that gap.

In these phase-diagrams, we consider 9 photon sectors to achieve the convergence. For the trivial case, we observe five different topological phases with $C = 0, \pm 1, -2$, and -3. In the low-frequency regime ($\Omega < 4.0$), we obtain topological phases with the high Chern number while in the high-frequency regime ($\Omega > 4.0$), system exhibits topological phases with $C = \pm 1$. In Fig. 5.3, where the phase diagram is plotted for the nontrivial case, we observe four different topological phases with Chern number $C = 0, -1, -2$, and -4. For this case, the system saturates at the topological phase with $C = -1$ in the high frequency regime. It is important to note that, for the different values of the driving amplitude $A_0 \in [0.1, 0.7]$, the variation in the Chern number with the driving frequency Ω is almost similar. The variation in the Chern number is mostly determined by the variation in Ω. Nevertheless, both the phase diagrams show that, in comparison to the undriven case, the Floquet version of the N stacked SSH chains displays much richer topological phases with high Chern numbers.

It is well known that the bulk boundary correspondence in the Floquet system is not the same as the undriven cases. In case of the undriven systems, the edge states appear

only in the energy gaps between the bulk bands. However, in the Floquet version of these systems, we have infinite number of copies of the undriven systems. The driving does not affect the band gap only between the original bands, but it also affects different copies or replicas, and consequently edge states can also appear in between Floquet replica bands. Here, we consider the Floquet bands or quasi-energy bands only in the first Floquet Brillouin zone (FBZ), where the edge states can exist at the central gap $\frac{\epsilon}{\Omega} = 0$; and as well as at the boundary of the FBZ, i.e., at $\frac{\epsilon}{\Omega} = 0.5$. As a consequence, the total number of chiral edge states are calculated from the relation $C = C_0 - C_\pi$, where C_0 and C_π respectively measure the number of chiral edge states in the central gap and the gap around the Floquet zone boundary. For the frequency regime $2.0 \leq \Omega \leq 6.0$, we observe $C_\pi = 0$ at the Floquet zone boundary. Therefore, in this frequency regime, the Chern number is always $C = C_0$.

The topological phase transitions observed in the phase diagrams are occurred in the system because the closing and re-opening of some of the band gaps. Therefore, in Figs. 5.2(b) and 5.3(b), we show the bands in the first FBZ along the high symmetric path. Earlier, we have mentioned that the topological phases are almost independent of A_0, we plot these band diagrams only for $A_0 = 0.1$. We see that phase transition occurs either due to the band gap closing at $\epsilon/\Omega = 0$ or at the Floquet zone boundary $\epsilon/\Omega = \pm 0.5$. Since, the maximum band gap in the undriven system is 4.0, we find that the band gap closing occurs at $\epsilon/\Omega = \pm 0.5$ when $\Omega = 4$.

5.3.2 Demonstration of the edge states of the Floquet topological phases with high Chern number

In this section, we demonstrate the edge states in the energy band diagrams for the higher Chern numbers with $|C| > 1$. In Fig. 5.2, we observed topological phases with the Chern number $C = -2$ and -3. Here, we select two pairs of the driving amplitudes and

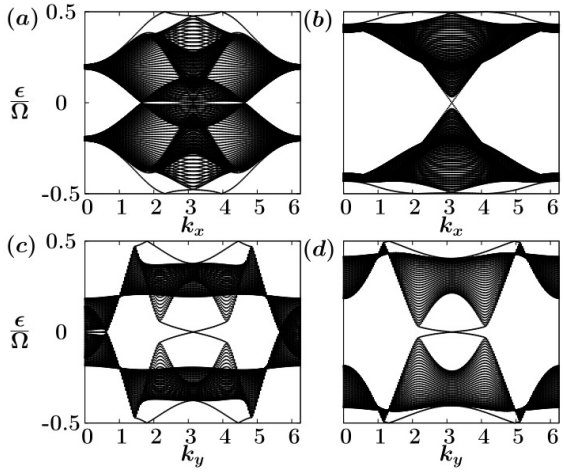

FIGURE 5.4: The quasienergy bands under POBCs are shown for the Chern numbers $C = -2$ and $C = -3$ corresponding to the phase diagram Fig. 5.2. In subfigures (a) and (c), the bands are plotted for the driving amplitude $A_0 = 0.5$ and the driving frequency $\Omega = 2.5$. In subfigures (b) and (d), the bands are plotted for $A_0 = 0.5$ and $\Omega = 3.5$. In both the cases, the individual SSH chain is considered as topologically trivial.

frequencies $(A_0 = 0.5, \Omega = 2.5)$ and $(A_0 = 0.5, \Omega = 3.5)$ from the phase diagram, where the corresponding Chern numbers are $C = -2$ and -3, respectively. For the presentation purpose, we choose $A_0 = 0.5$ so that the band gap is prominent and the edge states are clearly visible. In Fig. 5.4(a)-(d), we have shown the energy band diagram for the case of cylindrical geometry. In this figure, we consider individual SSH chain is topologically trivial.

In Fig. 5.5(a)-(d), the energy band diagrams for cylindrical geometry are presented, where the individual SSH chain is nontrivial. In these figures, we have shown the edge states for the topological phases with $C = -4$ and $C = -2$. The band diagrams (Figs. 5.4 and 5.5) exhibit edge states along both the directions, thus these show true 2D system even though the system is constructed as a weak topological insulator by stacking many SSH chains.

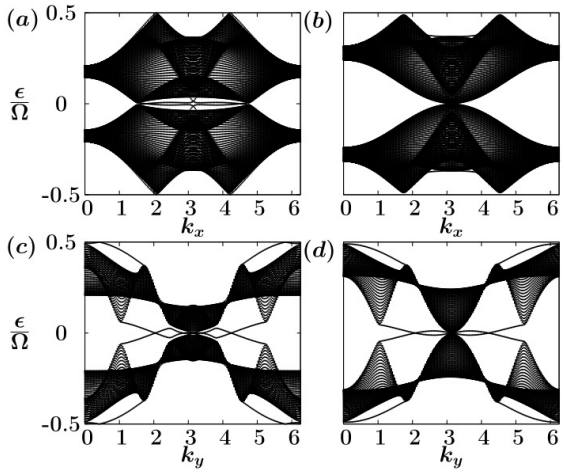

FIGURE 5.5: Quasienergy bands for cylindrical geometry are shown for the Chern numbers $C = -4$ and $C = -2$ corresponding to the phase diagram presented in Fig. 5.3. In subfigures (a) and (c), the bands are shown for the driving amplitude $A_0 = 0.5$ and the driving frequency $\Omega = 2.5$. In subfigures (b) and (d), the bands are presented for $A_0 = 0.5$ and $\Omega = 2.9$. In both the cases, the individual SSH chain is considered as topologically nontrivial.

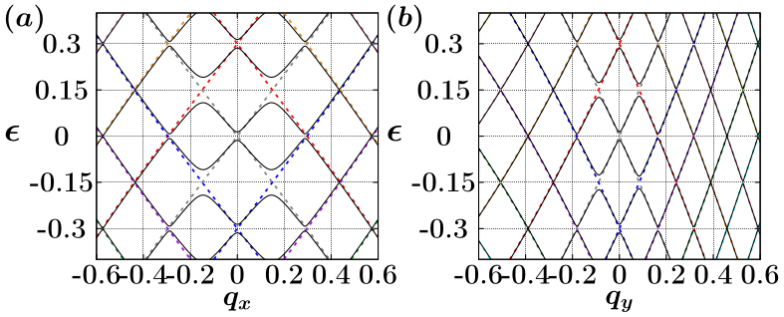

FIGURE 5.6: The quasienergy bands repulsion in case of the low-energy Hamiltonian is shown for the cylindrical geometry. In subfigure (a), the PBC is considered along the x-direction, and the OBC is considered along the y-direction. The boundary condition is interchanged in subfigure (b), i.e., the PBC is considered along x-direction, and the OBC is considered along the y-direction. Here, the individual SSH chain is considered as nontrivial. The colored dashed lines are used to show the quasi-energy bands for the undriven system, whereas the black solid lines are used for the driven case. We set the driving parameters at: $\Omega = 0.3$ and $A_0 = 0.05$.

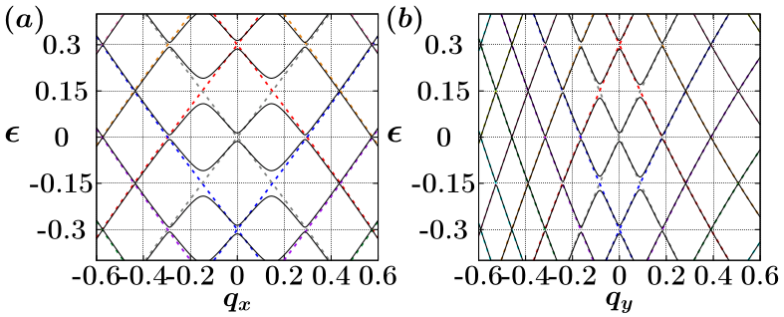

FIGURE 5.7: The results presented here is similar to Fig. 5.6, but here the individual SSH chain is topologically trivial.

5.4 Low-energy Hamiltonian

The low-energy Hamiltonian near the band touching point $\boldsymbol{K}_D = \left[\pi, \cos^{-1}\frac{\eta}{\delta}\right]$, can be derived by substituting $\boldsymbol{k} = \boldsymbol{q} + \boldsymbol{K}_D$ in Eq. (5.2). Here, $|\boldsymbol{q}| \ll 1$ and under this condition the Hamiltonian will be

$$\begin{aligned} h_x^{(0)} &= \frac{q_x^2}{2} - \eta q_y^2 - 2q_y\sqrt{\delta^2 - \eta^2} \\ h_y^{(0)} &= -q_x - q_x q_y\sqrt{\delta^2 - \eta^2} \end{aligned} \tag{5.7}$$

For the driven case, we obtain Fourier components of the low energy Hamiltonian by substituting $\boldsymbol{q} \to \boldsymbol{q} + \boldsymbol{A}(t)$

$$\begin{aligned} h_x^{(1)} &= q_x\frac{A_0}{2} + i\eta q_y A_0 + iA_0\sqrt{\delta^2 - \eta^2} \\ h_y^{(1)} &= -\frac{A_0}{2} + iq_x\frac{A_0}{2} + q_y\frac{A_0}{2}\sqrt{\delta^2 - \eta^2} \\ h_x^{(2)} &= \frac{A_0^2}{8} + \eta\frac{A_0^2}{4} \\ h_y^{(2)} &= i\frac{A_0^2}{4}\sqrt{\delta^2 - \eta^2} \end{aligned} \tag{5.8}$$

Here we see that, unlike graphene, the low-energy Hamiltonian of the N-stacked SSH model has a non-linear dispersion. Moreover, the Hamiltonian has asymmetry along k_x and k_y directions due to the presence of a coupling term. Overall, these made the system more complex than any other 2D systems. We now investigate the behavior of the low-energy Hamiltonian.

The effect of the asymmetry in the Hamiltonian can be seen in Figs. 5.6 and 5.7, where we have projected the Floquet bands along one of the directions of the quasi momenta, and set the value of the other quasi momentum equals zero. In this figure, the dotted lines represent energy bands of the undriven system, where different colors are used for denoting different photon sectors. The black solid lines are used for the driven case. As we turn on the driving, the Floquet bands corresponding to different

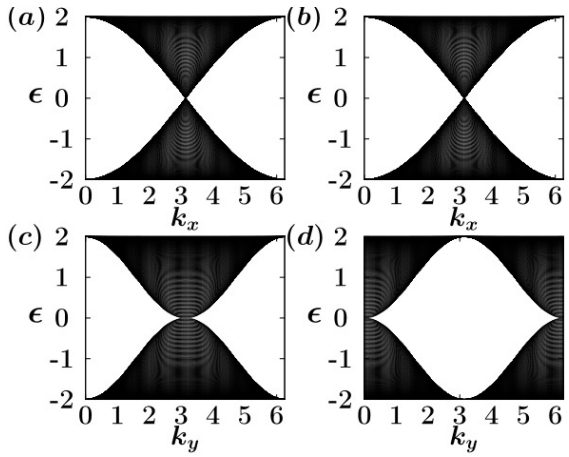

FIGURE 5.8: The quasienergy bands with a semi-Dirac point are shown for the undriven case with $\delta = |\eta|$. In subfigures (a) and (c), we set $\delta = 0.5$ and $\eta = -0.5$, and hence the individuak SSH chain is topologically trivial. On the other hand, in subfigures (b) and (d), where the individual SSH chain is made topologically nontrivial by setting $\delta = 0.5$ and $\eta = 0.5$.

photon sectors repel each other and create band gaps, where Floquet edge states can appear. Our major goal is to investigate whether the Floquet bands of the N stacked model has the same hierarchical structure as observed in graphene [206]. Even though our system is very much different from graphene, we observe some hierarchical structure in the Floquet band gaps at $\epsilon = 0$, and also at $\epsilon = \pm\frac{\Omega}{2}$. We observe that the behavior of the level repulsion around the central gap and the Floquet zone boundary is qualitatively similar to graphene. The width of the Floquet gaps are almost of the order of $\left(\frac{A_0}{\Omega}\right)^{\Delta m}$, where Δm is the difference between the photon sectors. In Figs. 5.6 and 5.7, we show by red and blue dotted lines that the first largest Floquet band gap occurs at $\epsilon = \pm\frac{\Omega}{2}$, due to the repulsion between the bands with photon sectors $m = \pm 1$ and $m = 0$. However, the width of the Floquet band gap at $\epsilon = 0$ between the bands in the zero photon sector is of the order of $\left(\frac{A_0}{\Omega}\right)^2$ [206].

5.5 N stacked SSH model with linearly polarized light

Earlier, we have shown that the N stacked SSH model has non-linear dispersion. Therefore, we choose the system parameters in such a way that this model also shows a

semi-Dirac point, i.e., a band touching point where the dispersion along one direction is linear and quadratic along the other direction. Similar semi-Dirac point is observed in hexagonal lattice. The semi-Dirac point of this system is split into two Dirac points if the system is shined by an LPL [204]. For our study, we consider two cases of the LPL: along x and y-directions. Our goal is to observe whether the semi-Dirac point of the N stacked SSH model also splits into two Dirac points. Here, we set $\delta = |\eta|$ in Eq. (5.2). For the case, when N stacked SSH chain is constructed with trivial SSH chains, we observe a semi-Dirac point at $[\pi, \pi]$ as shown in Figs. 5.8(a) and 5.8(c). For the other case, when N stacked SSH chain is constructed with nontrivial SSH chains, we find the semi-Dirac point at $[\pi, 0]$ (or at $[\pi, 2\pi]$) as shown in Figs. 5.8(b) and 5.8(d). The emergence of the semi-Dirac behavior can be identified by deriving the low-energy Hamiltonian around these band touching points as follows:

$$h_x^{(0)} = \frac{q_x^2}{2} - \eta q_y^2; \; h_y^{(0)} = -q_x \tag{5.9}$$

The above low energy Hamiltonian of the N stacked SSH model clearly shows semi-Dirac like behavior for the condition $[\delta = |\eta|]$. We now separately study the role of LPL along x and y-directions.

5.5.1 Linearly polarized light along x-direction

First, we consider the case when the LPL is applied along x-direction of the form $A(t) = A_0 \cos \Omega t$. For this driving, we find the Fourier component of the Hamiltonian for $m = 0$ as:

$$H^{(0)}_{N-SSH} = \boldsymbol{d}^{(0)}_{N-SSH} \cdot \boldsymbol{\sigma} \tag{5.10a}$$

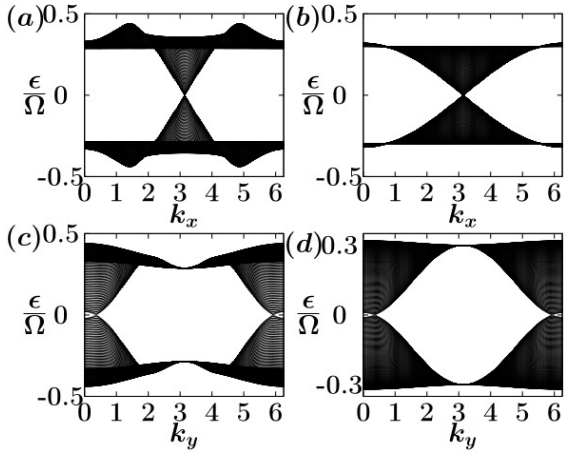

FIGURE 5.9: The quasienergy bands are presented, when the LPL is applied along the x-direction for the case when the individual SSH chain is topologically nontrivial. Here, we fix the driving parameters at $A_0 = 0.5$ and $\delta = \eta = 0.5$ in all the subfigures. In subfigures (a) and (c), we set $\Omega = 3.0$; while in subfigures (b) and (d), we set $\Omega = 6.0$. Here, we observe the emergence of the semi-Dirac like point as LPL is applied along x-direction.

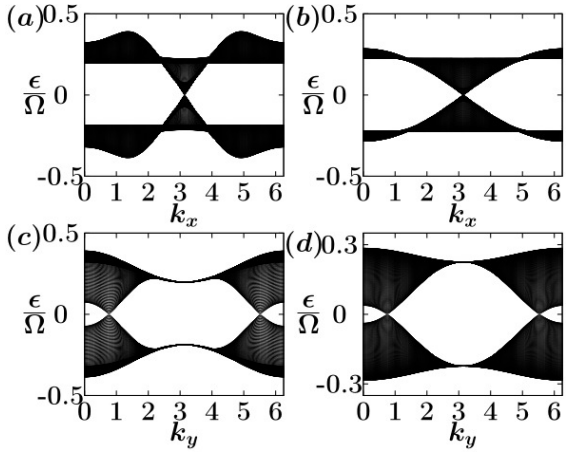

FIGURE 5.10: This figure is similar to Fig. 5.9, but here we consider stronger driving amplitude $A_0 = 1.0$.

where

$$\left(d^{(0)}_{N-SSH}\right)_x = (1-\eta) + (1+\eta)\,\cos k_x\, J_0(A_0) + \delta\,\cos k_y, \\ -\delta\,\cos k_x\,\cos k_y\, J_0(A_0) \tag{5.10b}$$

$$\left(d^{(0)}_{N-SSH}\right)_y = (1+\eta)\,\sin k_x\, J_0(A_0) - \delta\,\sin k_x\,\cos k_y\, J_0(A_0). \tag{5.10c}$$

The Fourier component of the Hamiltonian for $m = 1$ is obtained as:

$$H^{(1)}_{N-SSH} = \boldsymbol{d}^{(1)}_{N-SSH} \cdot \boldsymbol{\sigma} \tag{5.11a}$$

where

$$\left(d^{(1)}_{N-SSH}\right)_x = -(1+\eta)\ \sin k_x\, J_1(A_0) + \delta \sin k_x \cos k_y J_1(A_0) \tag{5.11b}$$

$$\left(d^{(1)}_{N-SSH}\right)_y = \left[(1+\eta) - \delta \cos k_y\right]\ \cos k_x\, J_1(A_0) \tag{5.11c}$$

and for $m = 2$ as:

$$H^{(2)}_{N-SSH} = \boldsymbol{d}^{(2)}_{N-SSH} \cdot \boldsymbol{\sigma} \tag{5.12a}$$

$$\left(d^{(2)}_{N-SSH}\right)_x = -(1+\eta)\ \cos k_x\, J_2(A_0) + \delta \cos k_x \cos k_y J_2(A_0) \tag{5.12b}$$

$$\left(d^{(2)}_{N-SSH}\right)_y = -\left[(1+\eta) - \delta \cos k_y\right]\ \sin k_x J_2(A_0). \tag{5.12c}$$

The Floquet energy band diagrams are shown in Figs. 5.9, 5.10 and 5.11. Here again we consider two different cases depending on the topological property of the individual SSH chain. In Figs. 5.9 and 5.10, each SSH chain is considered as nontrivial by setting $\eta = 0.5$. Unlike the case of hexagonal lattice, here we observe that the semi-Dirac like point splits into two band-touching points with non-linear dispersion along y-direction. This behavior is observed for both high and low frequency regime. In Figs. 5.9(a) and (c), we set the driving frequency $\Omega = 3.0$. On the other hand, in Figs. 5.9(b) and (d), we set $\Omega = 6.0$. The driving amplitude is fixed at $A_0 = 0.5$ for both the frequencies. As we increase the driving amplitude, the separation between the two band touching points also increase, as shown in Fig. 5.10. In contrary, when we consider each SSH chain as topologically trivial, the semi-Dirac like point does not split, but a band-gap opens at that point. This result is shown in Fig. 5.11.

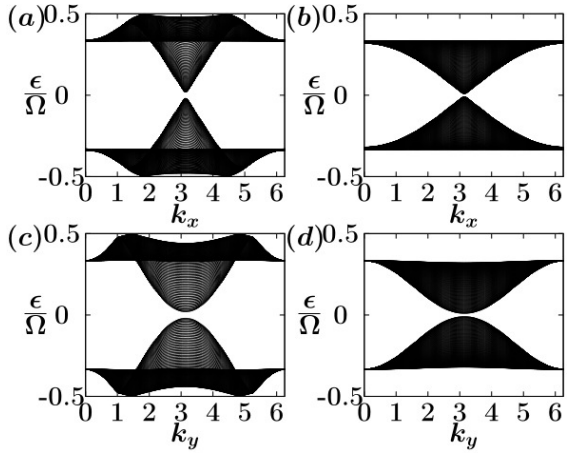

FIGURE 5.11: The quasi-energy bands are presented for the case when the LPL is applied along the x-direction. Here we fix the parameters $\delta = -\eta = 0.5$ and hence the individual SSH chain topologically trivial. We set the driving amplitude $A_0 = 0.5$. In subfigures (a) and (c), we set $\Omega = 3.0$; while in subfigures (b) and (d), we set $\Omega = 6.0$. Here, we see opening of a gap in the quasi-energy band gap at the semi-Dirac-like point.

5.5.2 Linearly polarized light along y-direction

We now consider the other case where the LPL is applied along y-direction of the same form as earlier, i.e., $A(t) = A_0 \cos \Omega t$. Like the previous case, for this driving, we find the Fourier component of the Hamiltonian for $m = 0$ as:

$$H^{(0)}_{N-SSH} = \boldsymbol{d}^{(0)}_{N-SSH} \cdot \boldsymbol{\sigma} \tag{5.13a}$$

where

$$\begin{aligned}\left(d^{(0)}_{N-SSH}\right)_x = {} & (1-\eta) + (1+\eta)\, \cos k_x + \delta\, \cos k_y\, J_0(A_0) \\ & - \delta\, \cos k_x\, \cos k_y\, J_0(A_0)\end{aligned} \tag{5.13b}$$

$$\left(d^{(0)}_{N-SSH}\right)_y = (1+\eta)\, \sin k_x - \delta\, \sin k_x\, \cos k_y\, J_0(A_0). \tag{5.13c}$$

Again, we derive the Fourier component of the Hamiltonian for $m = 1$ as:

$$H^{(1)}_{N-SSH} = \boldsymbol{d}^{(1)}_{N-SSH} \cdot \boldsymbol{\sigma} \tag{5.14a}$$

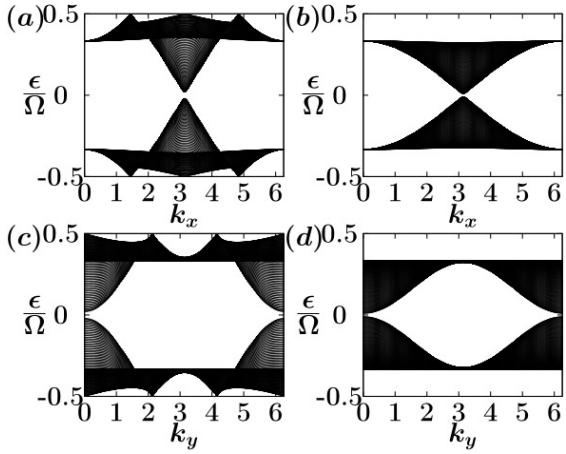

FIGURE 5.12: The quasi-energy bands are shown for the case when the LPL is applied along y-direction and here we consider the individual SSH chain as topologically nontrivial by setting the parameters $\delta = \eta = 0.5$. The driving amplitude is set at $A_0 = 0.5$ in all the subfigures. In the subfigures (a) and (c), we consider $\Omega = 3.0$; while $\Omega = 6.0$ is considered in subfigures (b) and (d). Here, we also observe opening of a band gap at the semi-Dirac-like point.

$$\left(d^{(1)}_{N-SSH}\right)_x = -\delta \sin k_y J_1(A_0) + \delta \cos k_x \sin k_y J_1(A_0) \tag{5.14b}$$

$$\left(d^{(1)}_{N-SSH}\right)_y = \delta \sin k_x \sin k_y J_1(A_0) \tag{5.14c}$$

and for $m = 2$ as:

$$H^{(2)}_{N-SSH} = \boldsymbol{d}^{(2)}_{N-SSH} \cdot \boldsymbol{\sigma} \tag{5.15a}$$

$$\left(d^{(2)}_{N-SSH}\right)_x = -\delta \cos k_y J_2(A_0) + \delta \cos k_x \cos k_y J_2(A_0) \tag{5.15b}$$

$$\left(d^{(2)}_{N-SSH}\right)_y = \delta \sin k_x \cos k_y J_2(A_0). \tag{5.15c}$$

In Fig. 5.12, the Floquet band diagrams are shown for the case where the individual SSH chain is topologically nontrivial. On the other hand, in Fig. 5.13, the Floquet band diagrams are presented for the trivial case. For both the cases, we find the semi-Dirac like point does not split, and a band gap opens at that point.

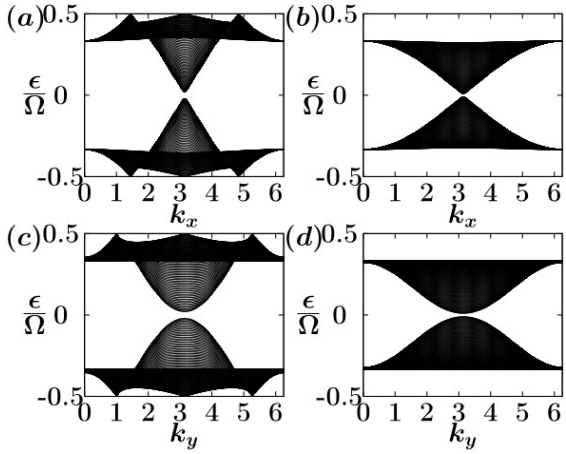

FIGURE 5.13: Similar results as Fig. 5.12 are presented, but here the individual SSH chain is considered as topologically trivial by setting $\delta = -\eta = 0.5$.

5.6 Summary

We consider a time-periodic driving acting on the N stacked SSH model and examine the topological properties of this system. We use circularly polarized light as a periodic drive and compute the effective Hamiltonian using the Floquet replica method. This method is an exact method that determines the topological phases in the high-frequency regime as well as in the low-frequency regime. This system exhibits topological phases with high Chern numbers in the low-frequency regime. We consider two different ways of constructing the N stacked SSH model: either construction has each trivial SSH chain, or the construction has each nontrivial SSH chain. In the driving parameter space, the phase diagram shows the topological phases with high Chern numbers in the low-frequency regime. After driving, both the construction has distinct topological properties. When the N stacked SSH model has all trivial SSH chains, the highest Chern number is $C = -3$ while for each nontrivial SSH chain, the highest Chern number is $C = -4$. We also observed that with the varying driving amplitude A_0, the topological phases remain the same but change with the varying driving frequency Ω. The topological transition occurs when a band gap closing or reopening happens in the system. Therefore, with the varying Ω, we have shown that the energy bands, lie in the first Floquet Brillouin zone. We have

also shown the band diagrams in cylindrical geometry to present the results with the high Chern number.

In the Floquet systems, the total number of chiral edge states between the gap at $\epsilon = 0$ and $\epsilon = \frac{\Omega}{2}$ is obtained by $C = C_0 - C_\pi$. Here, C_0 and C_π are calculated by the sum of the Chern number of all the Floquet bands below the energy at $\epsilon = 0$ and $\epsilon = \frac{\Omega}{2}$, respectively. For both cases, we always obtain $C_\pi = 0$; hence, we obtain $C = C_0$. The model we chose here is slightly nontrivial due to the coupling between the quasimomenta k_x and k_y. We compute a low-energy Hamiltonian around the band touching points to observe the effect of this coupling near the band touching points. This coupling leads to quadratic nonlinear dispersion. Even after the nonlinear dispersion, which is a completely different behavior from the Graphene, this model has the signature of hierarchy in the Floquet gaps.

Due to the unconventional dispersion (with the presence of coupling, qudratic and linear term), we observe a semi-Dirac-like band touching point for a particular choice of the system parameter. We find that, for the periodic driving with LPL along x-direction, the semi-Dirac-like point splits into two band touching points with nonlinear dispersion. On the other hand, when the LPL is applied along the y-direction, a band gap opens around the semi-Dirac-like point. The same observation is shown for the hexagonal lattice [204]. We have shown the band diagrams for the existence of the semi-Dirac point, splitting into two band points and the opening of the band gap for the cylindrical geometry.

6

Floquet topological phases of N stacked SSH model using elliptically polarized light

---

In this Chapter, we only include some of the preliminary results of this study.

6.1 Introduction

In the previous Chapter, we investigated the periodically driven N stacked SSH model where CPL and LPL were used as periodic driving. In this Chapter, we introduce the effect of elliptically polarized light (EPL) on the N stacked SSH model. We consider the EPL of the form

$$\boldsymbol{A} = \left[A_{0x}\cos\Omega t, A_{0y}\cos(\Omega t + \phi)\right]$$

Our main focus is to study the topological properties with the varying phase factor ϕ. Even for $\phi = 0$, this driving can be of the form EPL if $A_{0x} \neq A_{0y}$. In this Chapter, again we use the Floquet replica method to calculate the Floquet effective Hamiltonian. The Fourier component and the modified static Hamiltonian have the following form

$$\begin{aligned}
H^{(0)}_{N-SSH} &= \boldsymbol{d}^{(0)}_{N-SSH} \cdot \boldsymbol{\sigma} \\
\left(d^{(0)}_{N-SSH}\right)_x &= (1-\eta) + (1+\eta)\ \cos k_x\, J_0(A_{0x}) + \delta\ \cos k_y\, J_0(A_{0y}) \\
&\quad - \delta\ \cos k_x\ \cos k_y\, J_0(A_{0x}) J_0(A_{0y}) \\
\left(d^{(0)}_{N-SSH}\right)_y &= (1+\eta)\ \sin k_x\, J_0(A_{0x}) - \delta\ \sin k_x\ \cos k_y\, J_0(A_{0x}) J_0(A_{0y})
\end{aligned} \tag{6.1}$$

$$\begin{aligned}
H^{(1)}_{N-SSH} &= \boldsymbol{d}^{(1)}_{N-SSH} \cdot \boldsymbol{\sigma} \\
\left(d^{(1)}_{N-SSH}\right)_x &= -(1+\eta)\ \sin k_x\, J_1(A_{0x}) - \delta \sin k_y\, J_1(A_{0y})\, e^{i\phi} \\
&\quad - \delta \left\{ -\sin k_x\ \cos k_y J_1(A_{0x}) J_0(A_{0y}) - \cos k_x\ \sin k_y J_0(A_{0x}) J_1(A_{0y})\, e^{i\phi} \right\} \\
\left(d^{(1)}_{N-SSH}\right)_y &= (1+\eta)\ \cos k_x\, J_1(A_{0x}) \\
&\quad - \delta \left\{ \cos k_x\ \cos k_y J_1(A_{0x}) J_0(A_{0y}) - \sin k_x\ \sin k_y J_0(A_{0x}) J_1(A_{0y})\, e^{i\phi} \right\}
\end{aligned} \tag{6.2}$$

$$\begin{aligned}
H^{(2)}_{N-SSH} &= \boldsymbol{d}^{(2)}_{N-SSH} \cdot \boldsymbol{\sigma} \\
\left(d^{(2)}_{N-SSH}\right)_x &= -(1+\eta)\ \cos k_x\, J_2(A_{0x}) - \delta\ \cos k_y\, J_2(A_{0y})\, e^{i2\phi} \\
&\quad - \delta \sin k_x\ \sin k_y\, J_1(A_{0x}) J_1(A_{0y})\, e^{i\phi} \\
\left(d^{(2)}_{N-SSH}\right)_y &= -(1+\eta)\ \sin k_x\, J_2(A_{0x}) + \delta\ \cos k_x\ \sin k_y\, J_1(A_{0x})\, J_1(A_{0y})\, e^{i\phi}
\end{aligned} \tag{6.3}$$

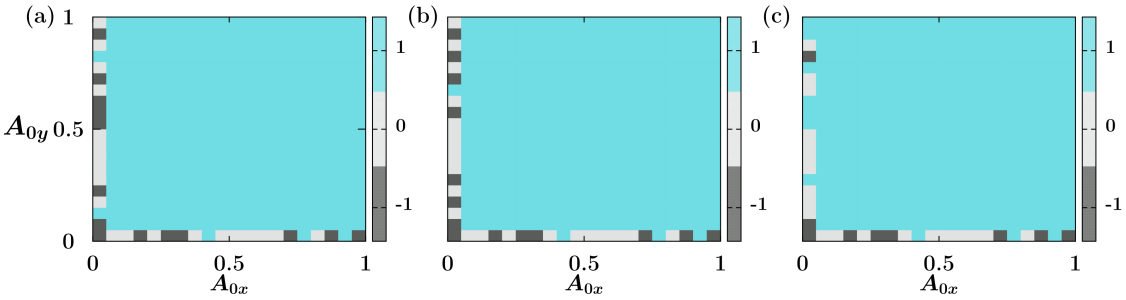

FIGURE 6.1: Different phase diagrams are shown for different values of ϕ in the high-frequency regime by choosing the driving frequency $\Omega = 6.0$. In this figure, the Chern number is shown as a function of driving amplitudes A_{0x} and A_{0y}. In subfigures (a), (b), and (c) we set ϕ as $\pi/3$, $\pi/4$ and $3\pi/4$, respectively. Here, in all subfigures, we choose $\delta = 1$ and $\eta = 0.5$. In the high-frequency regime, we observe topological phases with the Chern number $C = \pm 1$.

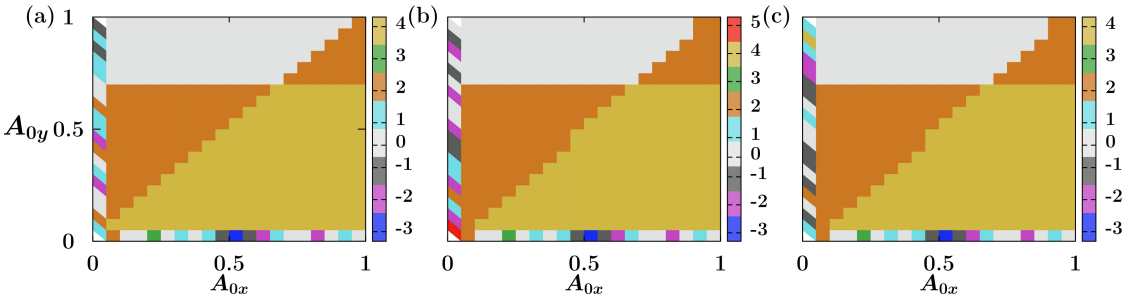

FIGURE 6.2: The same phase diagrams as shown in 6.1, are presented, but for $\Omega = 3.0$. In the low-frequency regime, we observe topological phases with the higher Chern number $|C| > 1$.

6.2 Results

In this section, we show phase diagrams for different ϕ values in high-frequency regimes by choosing $\Omega = 6.0$. In these phase diagrams, the Chern number is shown as a function of the driving amplitudes A_{0x} and A_{0y}. Here, the Chern number is the sum of the Chern number of all the Floquet bands below the energy $\epsilon = 0$ which shows the total number of chiral edge states in the gap $\epsilon = 0$. In all the phase diagrams, we observe the phase transitions between the Floquet topological phases with $C = 0$ and $C = \pm 1$. In Figs. 6.1(a), 6.1(b) and 6.1(c) which are plotted for $\phi = \pi/3$, $\phi = \pi/4$ and $\phi = 3\pi/4$, respectively, the Floquet topological phase saturates at $C = +1$ for $A_{0x}, A_{0y} > 0.1$. Next, we will present the same phase diagrams but in the low-frequency regime by choosing $\Omega = 3.0$.

For four different values of ϕ, the different phase diagrams are shown in Fig. 6.2 for $\Omega = 3.0$. Here, we observe the Floquet topological phases with the higher Chern number, i.e. $|C| > 1$. The phase diagrams are more or less similar when the driving amplitudes A_{0x} and A_{0y} are larger than 0.1.

Further, we want to calculate the time-averaged optical conductivity for this system using the extended Kubo formalism. The optical conductivity for a probe frequency ω is given as [155]

$$\sigma^{u\nu(m)}(\omega) = -i \sum_{\alpha,\gamma>\alpha} \sum_{m} \frac{f_\alpha - f_\gamma}{\epsilon_\alpha - \epsilon_\gamma - m\Omega} \times \left[\frac{j^{\nu(m)}_{\alpha\gamma} j^{u(-m)}_{\gamma\alpha}}{\omega + i0^+ - (\epsilon_\alpha - \epsilon_\gamma - m\Omega)} + \frac{j^{u(m)}_{\alpha\gamma} j^{\nu(-m)}_{\gamma\alpha}}{\omega + i0^+ + (\epsilon_\alpha - \epsilon_\gamma - m\Omega)} \right] \tag{6.4}$$

where m represents the different photon sectors, α, γ are band indices, f_α and f_γ are occupation of the bands and $j^{\nu(m)}_{\alpha\gamma}$ is the Fourier component along ν-direction which can

be obtained by as follows

$$j_{\alpha\gamma}^{\nu(m)} = \frac{1}{T}\int_0^T \langle \phi_\alpha(t) \mid \frac{\partial H(t)}{\partial k_\nu} \mid \phi_\gamma(t)\rangle \, e^{-im\Omega t} dt \tag{6.5}$$

Here, $\phi_{\alpha/\gamma}(t)$ and $\frac{\partial H(t)}{\partial k_\nu}$ are periodic and can expand by means of Fourier transformation and we obtain

$$j_{\alpha\gamma}^{\nu(m)} = \sum_{l,p} \langle \phi_\alpha^l \mid j^{\nu(p)} \mid \phi_\alpha^{l+m-p} \rangle \tag{6.6}$$

7

Conclusion and Outlook

7.1 Conclusion

The primary focus of this thesis was to investigate the topological properties of the quasi-1D TIs. The *Chapter* 3, studied the $E - SSH$ model, where a cyclic parameter θ was sitting in all the hopping amplitudes. We assumed this parameter θ as another synthetic dimension and behaved this $E - SSH$ model as a 2D model. Sinusoidal driving is applied to the NN and NNN hopping amplitudes. To compute the effective Hamiltonian, the Floquet replica method is used which works in the high-frequency as well as the low-frequency regime. In the high-frequency regime, we presented a phase diagram between the parameters of NNN hopping amplitudes. This result revealed that this model has the identical phase diagram as Haldane obtained for the hexagonal lattice with the borders of the Chern number $C = \pm 1$ while the middle part of this phase diagram is filled with the topological phases $C = \pm 3$. Moreover, this study also demonstrated two different phase diagrams in high- and low-frequency regimes where the Chern number is presented as

a function of the driving parameters ω and V. In the high-frequency regime, the largest Chern number is $C = 5$ whereas in the low-frequency regime, we obtained the topological phase with $|C| = 10$. The presence of the high Chern number phases ($C = 3$ and $C = 5$) is detected by showing the participation ratio and the corresponding Floquet Bloch state to show the localization of the states at the edges of the system. For these cases, we have also shown the band diagram along the high-symmetric path and the Berry curvature. At the points where the two bands come closer, the Berry curvature localizes, and the Chern number gets some non-zero contributions from these points. To observe the contribution from the Berry curvature to the Chern number, a local measure, 'local Chern number C_k' is shown as a function of k. This result found the jumps exactly at the same values of k where the Berry curvature localizes.

The *Chapter* 4, cataloged the topological phases of the N stacked SSH model by breaking symmetries systematically. This model can be attained by promoting the cyclic parameter θ of the $E - SSH$ model to an actual momentum. As the name explains, it is a 2D layered structure where N number of SSH chains are placed in y-direction. This model considered all the hopping in such a manner that it preserves all three fundamental symmetries (chiral, TR and PH). The primary goal of this study was to study the topological properties of this model by systematic breaking of the symmetries. In the presence of all three symmetries, this model showed $C = 0$. In this Chapter, we have provided a separate section that describes all the cases with $C = 0$. Next, this study considered the model that breaks chiral symmetry in the system. The breaking of chiral symmetry is obtained by considering hopping from A (or B) sublattice to A (or B) sublattice with real hopping strengths. Again, the model with broken chiral symmetry had $C = 0$. Then, by following the idea of Haldane, we introduced intra-sublattice hopping, but with imaginary and opposite strengths, which led to the breaking of the TR and chiral symmetry. In this category, four different models along with their topological properties

were demonstrated, where two models showed the topological properties with $C = \pm 1$. The presence of particle-hole symmetry facilitated an analytical calculation of C which agreed with the numerical calculation of C and also the phase diagram. Next, the case for $C = 0$ was demonstrated, which is explained by the 2D Zak phase which is quantized for chiral symmetric and chiral and TR symmetry broken systems. However, the 2D Zak phase was fractionalized when chiral symmetry was absent in the system. This detailed study finally showed the interplay between PH and inversion symmetry which also exhibited a topological phase transition. Here, the PH symmetry was broken for unequal intra-sublattice hopping and equal intra-sublattice hopping ensured the presence of inversion symmetry.

The *Chapter* 5 investigated N stacked SSH model with the application of periodic driving. This study adopted the model which preserves all three symmetries and applies CPL. The CPL is recognized for the breaking of TR symmetry in the system. Similar to *Chapter* 4, this study again considered two cases: the N stacked SSH model constructed either each SSH chain is topologically trivial or topologically nontrivial. The time-independent effective Hamiltonian is computed using the Floquet replica method which is further used for computing quasi-energies and the topological invariant. As discussed in *Chapter* 3, using the replica method, one can work in low-frequency as well as in the high-frequency regime. In the low-frequency regime, the driven system exhibited topological phases with a high Chern number for both cases whether the individual SSH chain is trivial or non-trivial. Contrary to the undriven N stacked SSH model, the periodically driven N stacked SSH model showed different topological phases for both cases. This model also has some heirarchy signature even the low-energy Hamiltonian has non-linear dispersion because of a cross term. This case is very different from the graphene which has linear dispersion. Moreover, the emergence of the semi-Dirac point split into two Dirac points with non-linear dispersion by the application of LPL

in x-direction and induced a gap at semi Dirac point with the application of LPL in y-direction.

7.2 Future outlook

We now sketch some of the promising projects which we like to work on in future.

A study of bilayer N stacked SSH model: Here, we will consider two layers of N stacked SSH model. First, we will construct the single N stacked SSH layer by placing an SSH chain starting with the A sublattice over the SSH chain which is starting with the sublattice B. The schematic diagram of this N stacked SSH model is shown in the following figure. The model Hamiltonian for a single layer of the N stacked SSH model will be as follows

$$\begin{aligned} H_{N-SSH} = &\sum_{n_x,n_y} \left[(1-\eta)c^{A\dagger}_{n_x,n_y}c^{B}_{n_x,n_y} + (1+\eta)c^{A\dagger}_{n_x+1,n_y}c^{B}_{n_x,n_y}\right] \\ &+ \delta \sum_{n_x,n_y} \left[c^{A\dagger}_{n_x,n_y}c^{B}_{n_x,n_y+1}\right] \end{aligned} \tag{7.1}$$

This work is essentially motivated by the bilayer Graphene. Our primary focus will be to compare this model with the bilayer graphene and find a magic angle with the intriguing topological properties in the system.

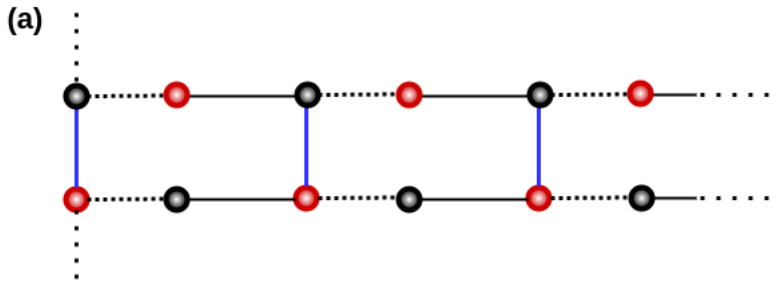

FIGURE 7.1: Schematic diagram of a single layer of N stacked SSH model that has a graphene-like structure. Here, red and black filled circles represent A and B sublattice, respectively.

***N* stacked SSH model irradiated by twisted light:** Recently, in Ref. [219], the monolayer graphene irradiated by a twisted light is reported. The components of the vector potential of twisted light are of the following form

$$A_x + iA_y = A_0 f(r) e^{i(\Omega t + m\phi)}$$

Here, A_0 is the driving amplitude, Ω is the driving frequency, $f(r)$ is the spatial profile and integer m is the orbital angular momentum. The twisted light is spatially modulated light which carries an orbital angular momentum and has phase singularity around the axis because of which the beam possesses a helical wavefront. In our previous study, we observed that N stacked SSH model shares some properties with graphene. In this project, we would also like to extend our study with the N stacked SSH model irradiated by a twisted light.

***N* stacked Kitaev model:** Like the N stacked SSH model, we would also like to study the stacked Kitaev model where the role of pairing term along x and y-direction can be observed. This project aims to uncover distinct topological phenomena in the presence of such pairing interactions. Additionally, these models can be further extended by incorporating a spin-orbit coupling term, with a pairing term, by adding a non-hermitian term and using a quasi-periodic potential. The comprehensive exploration of these aspects will provide an in-depth understanding of the emergence of exotic topological properties in these systems. Furthermore, we intend to investigate the optical conductivity of these models and explore their applicability in studying high harmonic generations.

Bibliography

[1] Desheng Kong and Yi Cui. Opportunities in chemistry and materials science for topological insulators and their nanostructures. *Nature Chemistry*, 3(11): 845–849, Nov 2011. ISSN 1755-4349. doi:10.1038/nchem.1171. URL https://doi.org/10.1038/nchem.1171.

[2] Liang et. al. Li. Highly conducting single-molecule topological insulators based on mono- and di-radical cations. *Nature Chemistry*, 14(9):1061–1067, Sep 2022. ISSN 1755-4349. doi:10.1038/s41557-022-00978-1. URL https://doi.org/10.1038/s41557-022-00978-1.

[3] Angel Martín Pendás, Julia Contreras-García, Fernanda Pinilla, José D. Mella, Carlos Cardenas, and Francisco Muñoz. A chemical theory of topological insulators. *Chem. Commun.*, 55:12281–12287, 2019. doi:10.1039/C9CC04054D. URL http://dx.doi.org/10.1039/C9CC04054D.

[4] R. J. Cava, Huiwen Ji, M. K. Fuccillo, Q. D. Gibson, and Y. S. Hor. Crystal structure and chemistry of topological insulators. *J. Mater. Chem. C*, 1:3176–3189, 2013. doi:10.1039/C3TC30186A. URL http://dx.doi.org/10.1039/C3TC30186A.

[5] K. v. Klitzing, G. Dorda, and M. Pepper. New method for high-accuracy determination of the fine-structure constant based on quantized Hall resistance. *Phys. Rev. Lett.*, 45:494–497, Aug 1980. doi:10.1103/PhysRevLett.45.494. URL https://link.aps.org/doi/10.1103/PhysRevLett.45.494.

[6] D. J. Thouless, M. Kohmoto, M. P. Nightingale, and M. den Nijs. Quantized Hall conductance in a two-dimensional periodic potential. *Phys. Rev. Lett.*, 49: 405–408, Aug 1982. doi:10.1103/PhysRevLett.49.405. URL https://link.aps.org/doi/10.1103/PhysRevLett.49.405.

[7] Barry Simon. Holonomy, the quantum adiabatic theorem, and berry's phase. *Phys. Rev. Lett.*, 51:2167–2170, Dec 1983. doi:10.1103/PhysRevLett.51.2167. URL https://link.aps.org/doi/10.1103/PhysRevLett.51.2167.

[8] Mahito Kohmoto. Topological invariant and the quantization of the hall conductance. *Annals of Physics*, 160(2):343–354, 1985. ISSN 0003-4916. doi:https://doi.org/10.1016/0003-4916(85)90148-4. URL https://www.sciencedirect.com/science/article/pii/0003491685901484.

[9] Qian Niu, D. J. Thouless, and Yong-Shi Wu. Quantized hall conductance as a topological invariant. *Phys. Rev. B*, 31:3372–3377, Mar 1985. doi:10.1103/PhysRevB.31.3372. URL https://link.aps.org/doi/10.1103/PhysRevB.31.3372.

[10] Yasuhiro Hatsugai. Chern number and edge states in the integer quantum Hall effect. *Phys. Rev. Lett.*, 71:3697–3700, Nov 1993. doi:10.1103/PhysRevLett.71.3697. URL https://link.aps.org/doi/10.1103/PhysRevLett.71.3697.

[11] J. E. Avron, R. Seiler, and B. Simon. Homotopy and quantization in condensed matter physics. *Phys. Rev. Lett.*, 51:51–53, Jul 1983. doi:10.1103/PhysRevLett.51.51. URL https://link.aps.org/doi/10.1103/PhysRevLett.51.51.

[12] F. D. M. Haldane. Model for a quantum Hall effect without landau levels: Condensed-matter realization of the "parity anomaly". *Phys. Rev. Lett.*, 61:2015–2018, Oct 1988. doi:10.1103/PhysRevLett.61.2015. URL https://link.aps.org/doi/10.1103/PhysRevLett.61.2015.

[13] C. L. Kane and E. J. Mele. Quantum spin Hall effect in graphene. *Phys. Rev. Lett.*, 95:226801, Nov 2005. doi:10.1103/PhysRevLett.95.226801. URL https://link.aps.org/doi/10.1103/PhysRevLett.95.226801.

[14] C. L. Kane and E. J. Mele. Z_2 topological order and the quantum spin Hall effect. *Phys. Rev. Lett.*, 95:146802, Sep 2005. doi:10.1103/PhysRevLett.95.146802. URL https://link.aps.org/doi/10.1103/PhysRevLett.95.146802.

[15] Shinsei Ryu and Yasuhiro Hatsugai. Topological origin of zero-energy edge states in particle-hole symmetric systems. *Phys. Rev. Lett.*, 89:077002, Jul 2002. doi:10.1103/PhysRevLett.89.077002. URL https://link.aps.org/doi/10.1103/PhysRevLett.89.077002.

[16] Joel E Moore. The birth of topological insulators. *Nature*, 464(7286):194–198, 2010. URL https://doi.org/10.1038/nature08916.

[17] M. Z. Hasan and C. L. Kane. Colloquium: Topological insulators. *Rev. Mod. Phys.*, 82:3045–3067, Nov 2010. doi:10.1103/RevModPhys.82.3045. URL https://link.aps.org/doi/10.1103/RevModPhys.82.3045.

[18] B. Andrei Bernevig, Taylor L. Hughes, and Shou-Cheng Zhang. Quantum spin Hall effect and topological phase transition in hgte quantum wells. *Science*, 314 (5806):1757–1761, 2006. doi:10.1126/science.1133734. URL https://www.science.org/doi/abs/10.1126/science.1133734.

[19] Alexander B. Khanikaev, S. Hossein Mousavi, Wang-Kong Tse, Mehdi Kargarian, Allan H. MacDonald, and Gennady Shvets. Photonic topological insulators. *Nature Materials*, 12(3):233–239, Mar 2013. ISSN 1476-4660. doi:10.1038/nmat3520. URL https://doi.org/10.1038/nmat3520.

[20] Mengyun He, Huimin Sun, and Qing Lin He. Topological insulator: Spintronics and quantum computations. *Frontiers of Physics*, 14(4):43401, May 2019. ISSN 2095-0470. doi:10.1007/s11467-019-0893-4. URL https://doi.org/10.1007/s11467-019-0893-4.

[21] Matthew J. Gilbert. Topological electronics. *Communications Physics*, 4(1):70, Apr 2021. ISSN 2399-3650. doi:10.1038/s42005-021-00569-5. URL https://doi.org/10.1038/s42005-021-00569-5.

[22] Wenchao Tian, Wenbo Yu, Jing Shi, and Yongkun Wang. The property, preparation and application of topological insulators: A review. *Materials*, 10(7), 2017. ISSN 1996-1944. doi:10.3390/ma10070814. URL https://www.mdpi.com/1996-1944/10/7/814.

[23] Ning Xu, Yong Xu, and Jia Zhu. Topological insulators for thermoelectrics. *npj Quantum Materials*, 2(1):51, Sep 2017. ISSN 2397-4648. doi:10.1038/s41535-017-0054-3. URL https://doi.org/10.1038/s41535-017-0054-3.

[24] Chenguang Fu, Yan Sun, and Claudia Felser. Topological thermoelectrics. *APL Materials*, 8(4):040913, 04 2020. ISSN 2166-532X. doi:10.1063/5.0005481. URL https://doi.org/10.1063/5.0005481.

[25] Yuri V. Ivanov, Alexander T. Burkov, and Dmitry A. Pshenay-Severin. Thermoelectric properties of topological insulators. *physica status solidi (b)*, 255 (7):1800020, 2018. doi:https://doi.org/10.1002/pssb.201800020. URL https://onlinelibrary.wiley.com/doi/abs/10.1002/pssb.201800020.

[26] Koushik Pal, Shashwat Anand, and Umesh V. Waghmare. Thermoelectric properties of materials with nontrivial electronic topology. *J. Mater. Chem. C*, 3: 12130–12139, 2015. doi:10.1039/C5TC02344K. URL http://dx.doi.org/10.1039/C5TC02344K.

[27] Yong Xu. Thermoelectric effects and topological insulators*. *Chinese Physics B*, 25(11):117309, sep 2016. doi:10.1088/1674-1056/25/11/117309. URL https://dx.doi.org/10.1088/1674-1056/25/11/117309.

[28] San-Dong Guo and Liang Qiu. Thermoelectric properties of topological insulator basn2. *Journal of Physics D: Applied Physics*, 50(1):015101, nov 2016. doi:10.1088/1361-6463/50/1/015101. URL https://dx.doi.org/10.1088/1361-6463/50/1/015101.

[29] Yu Zhou, Wang-Li Tao, Zhao-Yi Zeng, Xiang-Rong Chen, and Qi-Feng Chen. Thermoelectric properties of topological insulator lanthanum phosphide via first-principles study. *Journal of Applied Physics*, 125(4):045107, 01 2019. ISSN 0021-8979. doi:10.1063/1.5043170. URL https://doi.org/10.1063/1.5043170.

[30] H. Zhang, C. Q. Xu, S. H. Lee, Z. Q. Mao, and X. Ke. *Phys. Rev. B*, 105:184411, May 2022. doi:10.1103/PhysRevB.105.184411. URL https://link.aps.org/doi/10.1103/PhysRevB.105.184411.

[31] Yabin Fan and Kang L. Wang. Spintronics Based on Topological Insulators. *Spin*, 6(2):1640001-226, oct 2016. doi:10.1142/S2010324716400014.

[32] New horizons in spintronics. *Nature Materials*, 21(1):1–1, Jan 2022. ISSN 1476-4660. doi:10.1038/s41563-021-01184-z. URL https://doi.org/10.1038/s41563-021-01184-z.

[33] Dmytro Pesin and Allan H. MacDonald. Spintronics and pseudospintronics in graphene and topological insulators. *Nature Materials*, 11(5):409–416, May 2012. ISSN 1476-4660. doi:10.1038/nmat3305. URL https://doi.org/10.1038/nmat3305.

[34] Takehito Yokoyama and Shuichi Murakami. Spintronics and spincaloritronics in topological insulators. *Physica E: Low-dimensional Systems and Nanostructures*, 55:1–8, 2014. ISSN 1386-9477. doi:https://doi.org/10.1016/j.physe.2013.07.015. URL https://www.sciencedirect.com/science/article/pii/S1386947713002567. Topological Objects.

[35] Qing Lin He, Taylor L. Hughes, N. Peter Armitage, Yoshinori Tokura, and Kang L. Wang. Topological spintronics and magnetoelectronics. *Nature Materials*, 21(1): 15–23, Jan 2022. ISSN 1476-4660. doi:10.1038/s41563-021-01138-5. URL https://doi.org/10.1038/s41563-021-01138-5.

[36] Y. Shiomi, K. Nomura, Y. Kajiwara, K. Eto, M. Novak, Kouji Segawa, Yoichi Ando, and E. Saitoh. Spin-electricity conversion induced by spin injection into topological insulators. *Phys. Rev. Lett.*, 113:196601, Nov 2014. doi:10.1103/PhysRevLett.113.196601. URL https://link.aps.org/doi/10.1103/PhysRevLett.113.196601.

[37] N. Samarth. Topological spintronics. In *2016 74th Annual Device Research Conference (DRC)*, 2016 74th Annual Device Research Conference (DRC), pages 1–1, 2016. doi:10.1109/DRC.2016.7548496. URL https://doi.org/10.1109/DRC.2016.7548496.

[38] Bin Liu, Wuyuan Xie, Han Li, Yanrong Wang, Daoping Cai, Dandan Wang, Lingling Wang, Yuan Liu, Qiuhong Li, and Taihong Wang. Surrounding sensitive electronic properties of bi2te3 nanoplates—potential sensing applications of topological insulators. *Scientific Reports*, 4(1):4639, Apr 2014. ISSN 2045-2322. doi:10.1038/srep04639. URL https://doi.org/10.1038/srep04639.

[39] Andreas P. Schnyder, Shinsei Ryu, Akira Furusaki, and Andreas W. W. Ludwig. Classification of topological insulators and superconductors in three spatial dimensions. *Phys. Rev. B*, 78:195125, Nov 2008. doi:10.1103/PhysRevB.78.195125. URL https://link.aps.org/doi/10.1103/PhysRevB.78.195125.

[40] Shinsei Ryu, Andreas P Schnyder, Akira Furusaki, and Andreas W W Ludwig. Topological insulators and superconductors: tenfold way and dimensional hierarchy. *New Journal of Physics*, 12(6):065010, jun 2010. doi:10.1088/1367-2630/12/6/065010. URL https://doi.org/10.1088/1367-2630/12/6/065010.

[41] K. S. Novoselov, A. K. Geim, S. V. Morozov, D. Jiang, Y. Zhang, S. V. Dubonos, I. V. Grigorieva, and A. A. Firsov. Electric field effect in atomically thin carbon films. *Science*, 306(5696):666–669, 2004. doi:10.1126/science.1102896. URL https://www.science.org/doi/abs/10.1126/science.1102896.

[42] Y. L. Chen, J. G. Analytis, J.-H. Chu, Z. K. Liu, S.-K. Mo, X. L. Qi, H. J. Zhang, D. H. Lu, X. Dai, Z. Fang, S. C. Zhang, I. R. Fisher, Z. Hussain, and Z.-X. Shen. Experimental realization of a three-dimensional topological insulator, bi₂te₃. *Science*, 325(5937):178–181, 2009. doi:10.1126/science.1173034. URL https://www.science.org/doi/abs/10.1126/science.1173034.

[43] M. Zahid Hasan and Joel E. Moore. Three-dimensional topological insulators. *Annual Review of Condensed Matter Physics*, 2(1):55–78, 2011. doi:10.1146/annurev-conmatphys-062910-140432. URL https://doi.org/10.1146/annurev-conmatphys-062910-140432.

[44] W. P. Su, J. R. Schrieffer, and A. J. Heeger. Solitons in polyacetylene. *Phys. Rev. Lett.*, 42:1698–1701, Jun 1979. doi:10.1103/PhysRevLett.42.1698. URL https://link.aps.org/doi/10.1103/PhysRevLett.42.1698.

[45] A. J. Heeger, S. Kivelson, J. R. Schrieffer, and W. P. Su. Solitons in conducting polymers. *Rev. Mod. Phys.*, 60:781–850, Jul 1988. doi:10.1103/RevModPhys.60.781. URL https://link.aps.org/doi/10.1103/RevModPhys.60.781.

[46] János K Asbóth, László Oroszlány, and András Pályi. A short course on topological insulators. *Lecture notes in physics*, 919:997–1000, 2016. URL https://doi.org/10.1007/978-3-319-25607-8.

[47] Sanjib Kumar Das, Binghai Yan, Jeroen van den Brink, and Ion Cosma Fulga. Topological crystalline insulators from stacked graphene layers. *Phys. Rev. B*, 99: 165418, Apr 2019. doi:10.1103/PhysRevB.99.165418. URL https://link.aps.org/doi/10.1103/PhysRevB.99.165418.

[48] Si Li, Cheng-Cheng Liu, and Yugui Yao. Floquet high chern insulators in periodically driven chirally stacked multilayer graphene. *New Journal of Physics*, 20 (3):033025, mar 2018. doi:10.1088/1367-2630/aab2c7. URL https://dx.doi.org/10.1088/1367-2630/aab2c7.

[49] Marwa Mannaï, Jean-Noël Fuchs, Frédéric Piéchon, and Sonia Haddad. Stacking-induced Chern insulator. *Phys. Rev. B*, 107:045117, Jan 2023. doi:10.1103/PhysRevB.107.045117. URL https://link.aps.org/doi/10.1103/PhysRevB.107.045117.

[50] Jérôme Cayssol, Balázs Dóra, Ferenc Simon, and Roderich Moessner. Floquet topological insulators. *Physica Status Solidi – Rapid Research Letters*, 7(1-2): 101–108, 2013. doi:https://doi.org/10.1002/pssr.201206451. URL https://onlinelibrary.wiley.com/doi/abs/10.1002/pssr.201206451.

[51] A. Gómez-León and G. Platero. Floquet-Bloch theory and topology in periodically driven lattices. *Phys. Rev. Lett.*, 110:200403, May 2013. doi:10.1103/PhysRevLett.110.200403. URL https://link.aps.org/doi/10.1103/PhysRevLett.110.200403.

[52] Michael Victor Berry. Quantal phase factors accompanying adiabatic changes. *Proc. Royal Soc. London. A.*, 392(1802):45–57, 1984. URL https://doi.org/10.1098/rspa.1984.0023.

[53] S. Pancharatnam. Generalized theory of interference, and its applications. *Proceedings of the Indian Academy of Sciences - Section A*, 44(5):247–262, Nov 1956. ISSN 0370-0089. doi:10.1007/BF03046050. URL https://doi.org/10.1007/BF03046050.

[54] C. K. Chiang, C. R. Fincher, Y. W. Park, A. J. Heeger, H. Shirakawa, E. J. Louis, S. C. Gau, and Alan G. MacDiarmid. Electrical conductivity in doped polyacetylene. *Phys. Rev. Lett.*, 39:1098–1101, Oct 1977. doi:10.1103/PhysRevLett.39.1098. URL https://link.aps.org/doi/10.1103/PhysRevLett.39.1098.

[55] Hideki Shirakawa, Edwin J. Louis, Alan G. MacDiarmid, Chwan K. Chiang, and Alan J. Heeger. Synthesis of electrically conducting organic polymers: halogen derivatives of polyacetylene, (ch). *J. Chem. Soc., Chem. Commun.*, pages 578–580, 1977. doi:10.1039/C39770000578. URL http://dx.doi.org/10.1039/C39770000578.

[56] Jon H. Shirley. Solution of the schrödinger equation with a hamiltonian periodic in time. *Phys. Rev.*, 138:B979–B987, May 1965. doi:10.1103/PhysRev.138.B979. URL https://link.aps.org/doi/10.1103/PhysRev.138.B979.

[57] Charles Kittel. *Introduction to Solid State Physics*. Wiley, 8 edition, 2004. ISBN 9780471415268.

[58] N. W. Ashcroft and N. D. Mermin. *Solid State Physics*. Holt-Saunders, 1976.

[59] Hideo Sambe. Steady states and quasienergies of a quantum-mechanical system in an oscillating field. *Phys. Rev. A*, 7:2203–2213, Jun 1973. doi:10.1103/PhysRevA.7.2203. URL https://link.aps.org/doi/10.1103/PhysRevA.7.2203.

[60] A Eckardt and M Holthaus. Dressed matter waves. *Journal of Physics: Conference Series*, 99:012007, feb 2008. doi:10.1088/1742-6596/99/1/012007. URL https://doi.org/10.1088/1742-6596/99/1/012007.

[61] N Goldman, G Juzeliūnas, P Öhberg, and I B Spielman. Light-induced gauge fields for ultracold atoms. *Reports on Progress in Physics*, 77(12):126401, nov 2014. doi:10.1088/0034-4885/77/12/126401. URL https://doi.org/10.1088/0034-4885/77/12/126401.

[62] Takahiro Mikami, Sota Kitamura, Kenji Yasuda, Naoto Tsuji, Takashi Oka, and Hideo Aoki. Brillouin-Wigner theory for high-frequency expansion in periodically driven systems: Application to Floquet topological insulators. *Phys. Rev. B*, 93:144307, Apr 2016. doi:10.1103/PhysRevB.93.144307. URL https://link.aps.org/doi/10.1103/PhysRevB.93.144307.

[63] Alexander Altland and Martin R. Zirnbauer. Nonstandard symmetry classes in mesoscopic normal-superconducting hybrid structures. *Phys. Rev. B*, 55:1142–1161, Jan 1997. doi:10.1103/PhysRevB.55.1142. URL https://link.aps.org/doi/10.1103/PhysRevB.55.1142.

[64] P. Gehring, H. M. Benia, Y. Weng, R. Dinnebier, C. R. Ast, M. Burghard, and K. Kern. A natural topological insulator. *Nano Letters*, 13(3):1179–1184, 2013. doi:10.1021/nl304583m. URL https://doi.org/10.1021/nl304583m.

[65] Yoichi Ando. Topological insulator materials. *Journal of the Physical Society of Japan*, 82(10):102001, 2013. doi:10.7566/JPSJ.82.102001. URL https://doi.org/10.7566/JPSJ.82.102001.

[66] Gregor Jotzu, Michael Messer, Rémi Desbuquois, Martin Lebrat, Thomas Uehlinger, Daniel Greif, and Tilman Esslinger. Experimental realization of the topological Haldane model with ultracold fermions. *Nature*, 515(7526):237–240, 2014. URL https://doi.org/10.1038/nature13915.

[67] Mikael C Rechtsman, Julia M Zeuner, Yonatan Plotnik, Yaakov Lumer, Daniel Podolsky, Felix Dreisow, Stefan Nolte, Mordechai Segev, and Alexander Szameit. Photonic Floquet topological insulators. *Nature*, 496(7444):196–200, 2013. URL https://doi.org/10.1038/nature12066.

[68] T. Thonhauser and David Vanderbilt. Insulator/Chern-insulator transition in the Haldane model. *Phys. Rev. B*, 74:235111, Dec 2006. doi:10.1103/PhysRevB.74.235111. URL https://link.aps.org/doi/10.1103/PhysRevB.74.235111.

[69] Ningning Hao, Ping Zhang, Zhigang Wang, Wei Zhang, and Yupeng Wang. Topological edge states and quantum Hall effect in the Haldane model. *Phys. Rev. B*, 78:075438, Aug 2008. doi:10.1103/PhysRevB.78.075438. URL https://link.aps.org/doi/10.1103/PhysRevB.78.075438.

[70] Linhu Li, Zhihao Xu, and Shu Chen. Topological phases of generalized Su-Schrieffer-Heeger models. *Phys. Rev. B*, 89:085111, Feb 2014. doi:10.1103/PhysRevB.89.085111. URL https://link.aps.org/doi/10.1103/PhysRevB.89.085111.

[71] Yaacov E. Kraus, Yoav Lahini, Zohar Ringel, Mor Verbin, and Oded Zilberberg. Topological states and adiabatic pumping in quasicrystals. *Phys. Rev. Lett.*, 109:106402, Sep 2012. doi:10.1103/PhysRevLett.109.106402. URL https://link.aps.org/doi/10.1103/PhysRevLett.109.106402.

[72] Mor Verbin, Oded Zilberberg, Yaacov E. Kraus, Yoav Lahini, and Yaron Silberberg. Observation of topological phase transitions in photonic quasicrystals. *Phys. Rev. Lett.*, 110:076403, Feb 2013. doi:10.1103/PhysRevLett.110.076403. URL https://link.aps.org/doi/10.1103/PhysRevLett.110.076403.

[73] Feng Mei, Jia-Bin You, Dan-Wei Zhang, X. C. Yang, R. Fazio, Shi-Liang Zhu, and L. C. Kwek. Topological insulator and particle pumping in a one-dimensional shaken optical lattice. *Phys. Rev. A*, 90:063638, Dec 2014. doi:10.1103/PhysRevA.90.063638. URL https://link.aps.org/doi/10.1103/PhysRevA.90.063638.

[74] D. J. Thouless. Quantization of particle transport. *Phys. Rev. B*, 27:6083–6087, May 1983. doi:10.1103/PhysRevB.27.6083. URL https://link.aps.org/doi/10.1103/PhysRevB.27.6083.

[75] Huaiming Guo and Shu Chen. Kaleidoscope of symmetry-protected topological phases in one-dimensional periodically modulated lattices. *Phys. Rev. B*, 91:

041402, Jan 2015. doi:10.1103/PhysRevB.91.041402. URL https://link.aps.org/doi/10.1103/PhysRevB.91.041402.

[76] Masoud Bahari and Mir Vahid Hosseini. Zeeman-field-induced nontrivial topological phases in a one-dimensional spin-orbit-coupled dimerized lattice. *Phys. Rev. B*, 94:125119, Sep 2016. doi:10.1103/PhysRevB.94.125119. URL https://link.aps.org/doi/10.1103/PhysRevB.94.125119.

[77] N. Ahmadi, J. Abouie, and D. Baeriswyl. Topological and nontopological features of generalized Su-Schrieffer-Heeger models. *Phys. Rev. B*, 101:195117, May 2020. doi:10.1103/PhysRevB.101.195117. URL https://link.aps.org/doi/10.1103/PhysRevB.101.195117.

[78] Chao Li and Andrey E. Miroshnichenko. Extended SSH model: Non-local couplings and non-monotonous edge states. *Physics*, 1(1):2–16, 2019. ISSN 2624-8174. URL https://www.mdpi.com/2624-8174/1/1/2.

[79] Cui-Zu Chang, Jinsong Zhang, Xiao Feng, Jie Shen, Zuocheng Zhang, Minghua Guo, Kang Li, Yunbo Ou, Pang Wei, Li-Li Wang, Zhong-Qing Ji, Yang Feng, Shuaihua Ji, Xi Chen, Jinfeng Jia, Xi Dai, Zhong Fang, Shou-Cheng Zhang, Ke He, Yayu Wang, Li Lu, Xu-Cun Ma, and Qi-Kun Xue. Experimental observation of the quantum anomalous Hall effect in a magnetic topological insulator. *Science*, 340(6129):167–170, 2013. doi:10.1126/science.1234414. URL https://www.science.org/doi/abs/10.1126/science.1234414.

[80] Cui-Zu Chang, Weiwei Zhao, Duk Y. Kim, Haijun Zhang, Badih A. Assaf, Don Heiman, Shou-Cheng Zhang, Chaoxing Liu, and Jagadeesh S. Chan, Moses H. W.and Moodera. High-precision realization of robust quantum anomalous Hall state in a hard ferromagnetic topological insulator. *Nature Materials*, 14(5): 473–477, May 2015. ISSN 1476-4660. doi:10.1038/nmat4204. URL https://doi.org/10.1038/nmat4204.

[81] Yujun Deng, Yijun Yu, Meng Zhu Shi, Zhongxun Guo, Zihan Xu, Jing Wang, Xian Hui Chen, and Yuanbo Zhang. Quantum anomalous Hall effect in intrinsic magnetic topological insulator $MnBi_2Te_4$. *Science*, 367(6480):895–900, 2020. doi:10.1126/science.aax8156. URL https://www.science.org/doi/abs/10.1126/science.aax8156.

[82] Xufeng Kou, Shih-Ting Guo, Yabin Fan, Lei Pan, Murong Lang, Ying Jiang, Qiming Shao, Tianxiao Nie, Koichi Murata, Jianshi Tang, Yong Wang, Liang He, Ting-Kuo Lee, Wei-Li Lee, and Kang L. Wang. Scale-invariant quantum anomalous Hall effect in magnetic topological insulators beyond the two-dimensional limit. *Phys. Rev. Lett.*, 113:137201, Sep 2014. doi:10.1103/PhysRevLett.113.137201. URL https://link.aps.org/doi/10.1103/PhysRevLett.113.137201.

[83] J. G. Checkelsky, R. Yoshimi, A. Tsukazaki, K. S. Takahashi, Y. Kozuka, J. Falson, M. Kawasaki, and Y. Tokura. Trajectory of the anomalous Hall effect towards the quantized state in a ferromagnetic topological insulator. *Nature Physics*, 10 (10):731–736, Oct 2014. doi:10.1038/nphys3053. URL https://doi.org/10.1038/nphys3053.

[84] Yunbo Ou, Chang Liu, Gaoyuan Jiang, Yang Feng, Dongyang Zhao, Weixiong Wu, Xiao-Xiao Wang, Wei Li, Canli Song, Li-Li Wang, Wenbo Wang, Weida Wu, Yayu Wang, Ke He, Xu-Cun Ma, and Qi-Kun Xue. Enhancing the quantum anomalous Hall effect by magnetic codoping in a topological insulator. *Advanced Materials*, 30(1):1703062, 2018. doi:https://doi.org/10.1002/adma.201703062.

[85] M. Serlin, C. L. Tschirhart, H. Polshyn, Y. Zhang, J. Zhu, K. Watanabe, T. Taniguchi, L. Balents, and A. F. Young. Intrinsic quantized anomalous Hall effect in a Moiré heterostructure. *Science*, 367(6480):900–903, 2020. doi:10.1126/science.aay5533. URL https://www.science.org/doi/abs/10.1126/science.aay5533.

[86] Aaron L. Sharpe, Eli J. Fox, Arthur W. Barnard, Joe Finney, Kenji Watanabe, Takashi Taniguchi, M. A. Kastner, and David Goldhaber-Gordon. Emergent ferromagnetism near three-quarters filling in twisted bilayer graphene. *Science*, 365(6453):605–608, 2019. doi:10.1126/science.aaw3780. URL https://www.science.org/doi/abs/10.1126/science.aaw3780.

[87] Yi-Fan Zhao, Ruoxi Zhang, Ruobing Mei, Ling-Jie Zhou, Hemian Yi, Ya-Qi Zhang, Jiabin Yu, Run Xiao, Ke Wang, Nitin Samarth, Moses H. W. Chan, Chao-Xing Liu, and Cui-Zu Chang. Tuning the Chern number in quantum anomalous Hall insulators. *Nature*, 588(7838):419–423, Dec 2020. ISSN 1476-4687. doi:10.1038/s41586-020-3020-3. URL https://doi.org/10.1038/s41586-020-3020-3.

[88] Moumita Deb and Asim Kumar Ghosh. Topological phases of higher chern numbers in kitaev–heisenberg ferromagnet with further-neighbor interactions. *Journal of Physics: Condensed Matter*, 31(34):345601, jun 2019. doi:10.1088/1361-648x/ab22ef. URL https://doi.org/10.1088/1361-648x/ab22ef.

[89] Bartholomew Andrews and Gunnar Möller. Stability of fractional chern insulators in the effective continuum limit of harper-hofstadter bands with chern number $|c| > 1$. *Physical Review B*, 97(3), Jan 2018. ISSN 2469-9969. doi:10.1103/physrevb.97.035159. URL http://dx.doi.org/10.1103/PhysRevB.97.035159.

[90] Bartholomew Andrews, Titus Neupert, and Gunnar Möller. Stability, phase transitions, and numerical breakdown of fractional chern insulators in higher chern bands of the hofstadter model. *Physical Review B*, 104(12), Sep 2021. ISSN 2469-9969. doi:10.1103/physrevb.104.125107. URL http://dx.doi.org/10.1103/PhysRevB.104.125107.

[91] Takuya Kitagawa, Erez Berg, Mark Rudner, and Eugene Demler. Topological characterization of periodically driven quantum systems. *Phys. Rev. B*, 82:235114, Dec 2010. doi:10.1103/PhysRevB.82.235114. URL https://link.aps.org/doi/10.1103/PhysRevB.82.235114.

[92] A. Gómez-León and G. Platero. Floquet-Bloch theory and topology in periodically driven lattices. *Phys. Rev. Lett.*, 110:200403, May 2013. doi:10.1103/PhysRevLett.110.200403. URL https://link.aps.org/doi/10.1103/PhysRevLett.110.200403.

[93] Mark S. Rudner and Netanel H. Lindner. Band structure engineering and non-equilibrium dynamics in floquet topological insulators. *Nature Reviews Physics*, 2 (5):229–244, May 2020. ISSN 2522-5820. doi:10.1038/s42254-020-0170-z. URL https://doi.org/10.1038/s42254-020-0170-z.

[94] Hailong Wang, Derek Y. H. Ho, Wayne Lawton, Jiao Wang, and Jiangbin Gong. Kicked-harper model versus on-resonance double-kicked rotor model: From spectral difference to topological equivalence. *Phys. Rev. E*, 88:052920, Nov 2013. doi:10.1103/PhysRevE.88.052920. URL https://link.aps.org/doi/10.1103/PhysRevE.88.052920.

[95] Longwen Zhou and Jiangbin Gong. Floquet topological phases in a spin-1/2 double kicked rotor. *Phys. Rev. A*, 97:063603, Jun 2018. doi:10.1103/PhysRevA.97.063603. URL https://link.aps.org/doi/10.1103/PhysRevA.97.063603.

[96] Wang H. Ho D. et al. Zhou, L. Aspects of floquet bands and topological phase transitions in a continuously driven superlattice. *The European Physical Journal B*, 87, 2014. URL https://doi.org/10.1140/epjb/e2014-50465-9.

[97] Tanay Nag and Bitan Roy. Anomalous and normal dislocation modes in floquet topological insulators. *Communications Physics*, 4(1):157, Jul 2021. ISSN 2399-3650. doi:10.1038/s42005-021-00659-4. URL https://doi.org/10.1038/s42005-021-00659-4.

[98] Tanay Nag, Vladimir Juričić, and Bitan Roy. Out of equilibrium higher-order topological insulator: Floquet engineering and quench dynamics. *Phys. Rev. Research*, 1:032045, Dec 2019. doi:10.1103/PhysRevResearch.1.032045. URL https://link.aps.org/doi/10.1103/PhysRevResearch.1.032045.

[99] Tanay Nag and Atanu Rajak. Periodic and aperiodic dynamics of flat bands in diamond-octagon lattice. *Phys. Rev. B*, 104:134307, Oct 2021. doi:10.1103/PhysRevB.104.134307. URL https://link.aps.org/doi/10.1103/PhysRevB.104.134307.

[100] P. Leboeuf, J. Kurchan, M. Feingold, and D. P. Arovas. Phase-space localization: Topological aspects of quantum chaos. *Phys. Rev. Lett.*, 65:3076–3079, Dec 1990. doi:10.1103/PhysRevLett.65.3076. URL https://link.aps.org/doi/10.1103/PhysRevLett.65.3076.

[101] Gonzalo Usaj, P. M. Perez-Piskunow, L. E. F. Foa Torres, and C. A. Balseiro. Irradiated graphene as a tunable Floquet topological insulator. *Phys. Rev. B*, 90: 115423, Sep 2014. doi:10.1103/PhysRevB.90.115423. URL https://link.aps.org/doi/10.1103/PhysRevB.90.115423.

[102] Arijit Kundu, H. A. Fertig, and Babak Seradjeh. Effective theory of Floquet topological transitions. *Phys. Rev. Lett.*, 113:236803, Dec 2014. doi:10.1103/PhysRevLett.113.236803. URL https://link.aps.org/doi/10.1103/PhysRevLett.113.236803.

[103] Arnob Kumar Ghosh, Tanay Nag, and Arijit Saha. Floquet generation of a second-order topological superconductor. *Phys. Rev. B*, 103:045424, Jan 2021. doi:10.1103/PhysRevB.103.045424. URL https://link.aps.org/doi/10.1103/PhysRevB.103.045424.

[104] Arnob Kumar Ghosh, Tanay Nag, and Arijit Saha. Floquet second order topological superconductor based on unconventional pairing. *Phys. Rev. B*, 103:085413, Feb 2021. doi:10.1103/PhysRevB.103.085413. URL https://link.aps.org/doi/10.1103/PhysRevB.103.085413.

[105] Qing-Jun Tong, Jun-Hong An, Jiangbin Gong, Hong-Gang Luo, and C. H. Oh. Generating many majorana modes via periodic driving: A superconductor model. *Phys. Rev. B*, 87:201109, May 2013. doi:10.1103/PhysRevB.87.201109. URL https://link.aps.org/doi/10.1103/PhysRevB.87.201109.

[106] V. Dal Lago, M. Atala, and L. E. F. Foa Torres. Floquet topological transitions in a driven one-dimensional topological insulator. *Phys. Rev. A*, 92:023624, Aug 2015. doi:10.1103/PhysRevA.92.023624. URL https://link.aps.org/doi/10.1103/PhysRevA.92.023624.

[107] Scott A. Skirlo, Ling Lu, and Marin Soljačić. Multimode one-way waveguides of large Chern numbers. *Phys. Rev. Lett.*, 113:113904, Sep 2014. doi:10.1103/PhysRevLett.113.113904. URL https://link.aps.org/doi/10.1103/PhysRevLett.113.113904.

[108] Scott A. Skirlo, Ling Lu, Yuichi Igarashi, Qinghui Yan, John Joannopoulos, and Marin Soljačić. Experimental observation of large Chern numbers in photonic crystals. *Phys. Rev. Lett.*, 115:253901, Dec 2015. doi:10.1103/PhysRevLett.115.253901. URL https://link.aps.org/doi/10.1103/PhysRevLett.115.253901.

[109] Tian-Shi Xiong, Jiangbin Gong, and Jun-Hong An. Towards large-Chern-number topological phases by periodic quenching. *Phys. Rev. B*, 93:184306, May 2016. doi:10.1103/PhysRevB.93.184306. URL https://link.aps.org/doi/10.1103/PhysRevB.93.184306.

[110] Shujie Cheng, Honghao Yin, Zhanpeng Lu, Chaocheng He, Pei Wang, and Gao Xianlong. Predicting large-Chern-number phases in a shaken optical dice lattice. *Phys. Rev. A*, 101:043620, Apr 2020. doi:10.1103/PhysRevA.101.043620. URL https://link.aps.org/doi/10.1103/PhysRevA.101.043620.

[111] Hua Jiang, Zhenhua Qiao, Haiwen Liu, and Qian Niu. Quantum anomalous Hall effect with tunable Chern number in magnetic topological insulator film. *Phys. Rev. B*, 85:045445, Jan 2012. doi:10.1103/PhysRevB.85.045445. URL https://link.aps.org/doi/10.1103/PhysRevB.85.045445.

[112] Chen Fang, Matthew J. Gilbert, and B Andrei Bernevig. Large-Chern-number quantum anomalous Hall effect in thin-film topological crystalline insulators. *Phys. Rev. Lett.*, 112:046801, Jan 2014. doi:10.1103/PhysRevLett.112.046801. URL https://link.aps.org/doi/10.1103/PhysRevLett.112.046801.

[113] Yi-Xiang Wang and Fuxiang Li. High Chern number phase in topological insulator multilayer structures. *Phys. Rev. B*, 104:035202, Jul 2021. doi:10.1103/PhysRevB.104.035202. URL https://link.aps.org/doi/10.1103/PhysRevB.104.035202.

[114] Doru Sticlet, Frederic Piéchon, Jean-Noël Fuchs, Pavel Kalugin, and Pascal Simon. Geometrical engineering of a two-band Chern insulator in two dimensions with arbitrary topological index. *Phys. Rev. B*, 85:165456, Apr 2012. doi:10.1103/PhysRevB.85.165456. URL https://link.aps.org/doi/10.1103/PhysRevB.85.165456.

[115] Zhen Zhang, Jing-Yang You, Xing-Yu Ma, Bo Gu, and Gang Su. Kagome quantum anomalous Hall effect with high Chern number and large band gap. *Phys. Rev. B*, 103:014410, Jan 2021. doi:10.1103/PhysRevB.103.014410. URL https://link.aps.org/doi/10.1103/PhysRevB.103.014410.

[116] Hui Yang, Junjie Zeng, Yulei Han, and Zhenhua Qiao. Anderson localization induced by spin-flip disorder in large-Chern-number quantum anomalous Hall effect. *Phys. Rev. B*, 104:115414, Sep 2021. doi:10.1103/PhysRevB.104.115414. URL https://link.aps.org/doi/10.1103/PhysRevB.104.115414.

[117] Longwen Zhou and Jiangbin Gong. Recipe for creating an arbitrary number of floquet chiral edge states. *Phys. Rev. B*, 97:245430, Jun 2018. doi:10.1103/PhysRevB.97.245430. URL https://link.aps.org/doi/10.1103/PhysRevB.97.245430.

[118] Xiao-Long Lü and Hang Xie. Topological phases and pumps in the Su-Schrieffer-Heeger model periodically modulated in time. *Journal of Physics: Condensed Matter*, 31(49):495401, 2019. URL https://doi.org/10.1088/1361-648x/ab3d72.

[119] Chun-Fang Li, Li-Na Luan, and Lin-Cheng Wang. Topological properties of an extend Su-Schrieffer-Heeger model under periodic kickings. *International Journal of Theoretical Physics*, 59:2852, July 2020. doi:10.1007/s10773-020-04545-7.

[120] Ching-Kai Chiu, Jeffrey C. Y. Teo, Andreas P. Schnyder, and Shinsei Ryu. Classification of topological quantum matter with symmetries. *Rev. Mod. Phys.*, 88:035005, Aug 2016. doi:10.1103/RevModPhys.88.035005. URL https://link.aps.org/doi/10.1103/RevModPhys.88.035005.

[121] Souvik Bandyopadhyay, Utso Bhattacharya, and Amit Dutta. Temporal variation in the winding number due to dynamical symmetry breaking and associated transport in a driven Su-Schrieffer-Heeger chain. *Phys. Rev. B*, 100:054305, Aug 2019. doi:10.1103/PhysRevB.100.054305. URL https://link.aps.org/doi/10.1103/PhysRevB.100.054305.

[122] Y. H. Wang, H. Steinberg, P. Jarillo-Herrero, and N. Gedik. Observation of Floquet-Bloch states on the surface of a topological insulator. *Science*, 342(6157):453–457, 2013. ISSN 0036-8075. doi:10.1126/science.1239834. URL https://science.sciencemag.org/content/342/6157/453.

[123] Here $|u_\alpha\rangle$ are the eigenstates of the Floquet Hamiltonian H_F, i.e., $H_F|u_\alpha\rangle = E_\alpha|u_\alpha\rangle$. A typical structure of all the eigenstates is

$$|u_\alpha\rangle = [\ldots\ldots \underbrace{* * *}_{|u_\alpha^{-1}\rangle} \underbrace{* * *}_{|u_\alpha^{0}\rangle} \underbrace{* * *}_{|u_\alpha^{+1}\rangle} \ldots\ldots]^T,$$

where $|u_\alpha^m\rangle$ are the components of the eigenstate $|u_\alpha\rangle$ in the photon sector m. We have assigned the color to each of the eigenvalues E_α by calculating the corresponding static weight $|\langle u_\alpha^0|u_\alpha^0\rangle|^2$.

[124] Takahiro Fukui, Yasuhiro Hatsugai, and Hiroshi Suzuki. Chern numbers in discretized Brillouin zone: efficient method of computing (spin) Hall conductances. *Journal of the Physical Society of Japan*, 74(6):1674–1677, 2005. URL https://doi.org/10.1143/JPSJ.74.1674.

[125] N. Goldman and J. Dalibard. Periodically driven quantum systems: Effective hamiltonians and engineered gauge fields. *Phys. Rev. X*, 4:031027, Aug 2014. doi:10.1103/PhysRevX.4.031027. URL https://link.aps.org/doi/10.1103/PhysRevX.4.031027.

[126] Brandon M. Anderson, I. B. Spielman, and Gediminas Juzeliūnas. Magnetically generated spin-orbit coupling for ultracold atoms. *Phys. Rev. Lett.*, 111:125301, Sep 2013. doi:10.1103/PhysRevLett.111.125301. URL https://link.aps.org/doi/10.1103/PhysRevLett.111.125301.

[127] Zhi-Fang Xu, Li You, and Masahito Ueda. Atomic spin-orbit coupling synthesized with magnetic-field-gradient pulses. *Phys. Rev. A*, 87:063634, Jun 2013. doi:10.1103/PhysRevA.87.063634. URL https://link.aps.org/doi/10.1103/PhysRevA.87.063634.

[128] Anders S. Sørensen, Eugene Demler, and Mikhail D. Lukin. Fractional quantum hall states of atoms in optical lattices. *Phys. Rev. Lett.*, 94:086803, Mar 2005. doi:10.1103/PhysRevLett.94.086803. URL https://link.aps.org/doi/10.1103/PhysRevLett.94.086803.

[129] Juan Zurita, Charles E. Creffield, and Gloria Platero. Topology and interactions in the photonic creutz and creutz-hubbard ladders. *Advanced Quantum Technologies*, 3(2):1900105, 2020. doi:https://doi.org/10.1002/qute.201900105. URL https://onlinelibrary.wiley.com/doi/abs/10.1002/qute.201900105.

[130] Milad Jangjan and Mir Vahid Hosseini. Topological properties of subsystem-symmetry-protected edge states in an extended quasi-one-dimensional dimerized lattice. *Phys. Rev. B*, 106:205111, Nov 2022. doi:10.1103/PhysRevB.106.205111. URL https://link.aps.org/doi/10.1103/PhysRevB.106.205111.

[131] Milad Jangjan and Mir Vahid Hosseini. Floquet engineering of topological metal states and hybridization of edge states with bulk states in dimerized two-leg ladders. *Scientific Reports*, 10(1):14256, Aug 2020. ISSN 2045-2322. doi:10.1038/s41598-020-71196-3. URL https://doi.org/10.1038/s41598-020-71196-3.

[132] B Hetényi and M Yahyavi. Topological insulation in a ladder model with particle-hole and reflection symmetries. *Journal of Physics: Condensed Matter*, 30(10): 10LT01, feb 2018. doi:10.1088/1361-648X/aaac9d. URL https://dx.doi.org/10.1088/1361-648X/aaac9d.

[133] Kyle Monkman and Jesko Sirker. Operational entanglement of symmetry-protected topological edge states. *Phys. Rev. Research*, 2:043191, Nov 2020. doi:10.1103/PhysRevResearch.2.043191. URL https://link.aps.org/doi/10.1103/PhysRevResearch.2.043191.

[134] Carla Borja, Esther Gutiérrez, and Alexander López. Emergence of Floquet edge states in the coupled Su-Schrieffer-Heeger model. *Journal of Physics: Condensed Matter*, 34(20):205701, mar 2022. doi:10.1088/1361-648x/ac5865. URL https://doi.org/10.1088/1361-648x/ac5865.

[135] C. Li, S. Lin, G. Zhang, and Z. Song. Topological nodal points in two coupled Su-Schrieffer-Heeger chains. *Phys. Rev. B*, 96:125418, Sep 2017. doi:10.1103/PhysRevB.96.125418. URL https://link.aps.org/doi/10.1103/PhysRevB.96.125418.

[136] A. Sivan and M. Orenstein. Topology of multiple cross-linked Su-Schrieffer-Heeger chains. *Phys. Rev. A*, 106:022216, Aug 2022. doi:10.1103/PhysRevA.106.022216. URL https://link.aps.org/doi/10.1103/PhysRevA.106.022216.

[137] Shao-Liang Zhang and Qi Zhou. Two-leg Su-Schrieffer-Heeger chain with glide reflection symmetry. *Phys. Rev. A*, 95:061601, Jun 2017. doi:10.1103/PhysRevA.95.061601. URL https://link.aps.org/doi/10.1103/PhysRevA.95.061601.

[138] Daichi Obana, Feng Liu, and Katsunori Wakabayashi. Topological edge states in the Su-Schrieffer-Heeger model. *Phys. Rev. B*, 100:075437, Aug 2019. doi:10.1103/PhysRevB.100.075437. URL https://link.aps.org/doi/10.1103/PhysRevB.100.075437.

[139] Chang-An Li, Sang-Jun Choi, Song-Bo Zhang, and Björn Trauzettel. Dirac states in an inclined two-dimensional Su-Schrieffer-Heeger model. *Phys. Rev. Research*, 4:023193, Jun 2022. doi:10.1103/PhysRevResearch.4.023193. URL https://link.aps.org/doi/10.1103/PhysRevResearch.4.023193.

[140] Feng Liu and Katsunori Wakabayashi. Novel topological phase with a zero berry curvature. *Phys. Rev. Lett.*, 118:076803, Feb 2017. doi:10.1103/PhysRevLett.118.076803. URL https://link.aps.org/doi/10.1103/PhysRevLett.118.076803.

[141] Bo-Hung Chen. *Two-Dimensional Extended Su-Schrieffer-Heeger Model*. PhD thesis, National Taiwan Normal University (Taiwan), 2018. URL http://rportal.lib.ntnu.edu.tw:8080/server/api/core/bitstreams/9c19bce0-b5f3-44da-9927-53d2ed784c9b/content.

[142] A Pályi. Topological Insulators. URL https://physics.bme.hu/sites/physics.bme.hu/files/users/BMETE11MF34_kov/weyl_semimetals.pdf.

[143] Peter Rosenberg and Efstratios Manousakis. Topological superconductivity in a two-dimensional Weyl SSH model. *Phys. Rev. B*, 106:054511, Aug 2022. doi:10.1103/PhysRevB.106.054511. URL https://link.aps.org/doi/10.1103/PhysRevB.106.054511.

[144] Peter Rosenberg and Efstratios Manousakis. Weyl nodal-ring semimetallic behavior and topological superconductivity in crystalline forms of Su-Schrieffer-Heeger chains. *Phys. Rev. B*, 104:134511, Oct 2021. doi:10.1103/PhysRevB.104.134511. URL https://link.aps.org/doi/10.1103/PhysRevB.104.134511.

[145] Peter Rosenberg, Niraj Aryal, and Efstratios Manousakis. Numerically exact study of Weyl superconductivity. *Phys. Rev. B*, 100:104522, Sep 2019. doi:10.1103/PhysRevB.100.104522. URL https://link.aps.org/doi/10.1103/PhysRevB.100.104522.

[146] Liang Fu, C. L. Kane, and E. J. Mele. Topological insulators in three dimensions. *Phys. Rev. Lett.*, 98:106803, Mar 2007. doi:10.1103/PhysRevLett.98.106803. URL https://link.aps.org/doi/10.1103/PhysRevLett.98.106803.

[147] J. E. Moore and L. Balents. Topological invariants of time-reversal-invariant band structures. *Phys. Rev. B*, 75:121306, Mar 2007. doi:10.1103/PhysRevB.75.121306. URL https://link.aps.org/doi/10.1103/PhysRevB.75.121306.

[148] Zohar Ringel, Yaacov E. Kraus, and Ady Stern. Strong side of weak topological insulators. *Phys. Rev. B*, 86:045102, Jul 2012. doi:10.1103/PhysRevB.86.045102. URL https://link.aps.org/doi/10.1103/PhysRevB.86.045102.

[149] Cheng-Cheng Liu, Jin-Jian Zhou, Yugui Yao, and Fan Zhang. Weak topological insulators and composite Weyl semimetals: β-Bi_4X_4 (X=Br, I). *Phys. Rev. Lett.*, 116:066801, Feb 2016. doi:10.1103/PhysRevLett.116.066801. URL https://link.aps.org/doi/10.1103/PhysRevLett.116.066801.

[150] A. A. Burkov. Topological semimetals. *Nature Materials*, 15(11):1145–1148, Nov 2016. ISSN 1476-4660. doi:10.1038/nmat4788. URL https://doi.org/10.1038/nmat4788.

[151] Andrei Bernevig, Hongming Weng, Zhong Fang, and Xi Dai. Recent progress in the study of topological semimetals. *Journal of the Physical Society of Japan*, 87 (4):041001, 2018. doi:10.7566/JPSJ.87.041001. URL https://doi.org/10.7566/JPSJ.87.041001.

[152] Xiangang Wan, Ari M. Turner, Ashvin Vishwanath, and Sergey Y. Savrasov. Topological semimetal and fermi-arc surface states in the electronic structure of pyrochlore iridates. *Phys. Rev. B*, 83:205101, May 2011. doi:10.1103/PhysRevB.83.205101. URL https://link.aps.org/doi/10.1103/PhysRevB.83.205101.

[153] S. M. Young, S. Zaheer, J. C. Y. Teo, C. L. Kane, E. J. Mele, and A. M. Rappe. Dirac semimetal in three dimensions. *Phys. Rev. Lett.*, 108:140405, Apr 2012. doi:10.1103/PhysRevLett.108.140405. URL https://link.aps.org/doi/10.1103/PhysRevLett.108.140405.

[154] Huanhuan Yang, Lingling Song, Yunshan Cao, and Peng Yan. Experimental realization of two-dimensional weak topological insulators. *Nano Letters*, 22(7): 3125–3132, Apr 2022. ISSN 1530-6984. doi:10.1021/acs.nanolett.2c00555. URL https://doi.org/10.1021/acs.nanolett.2c00555.

[155] S. Sajad Dabiri, Hosein Cheraghchi, and Ali Sadeghi. Floquet states and optical conductivity of an irradiated two-dimensional topological insulator. *Phys. Rev. B*, 106:165423, Oct 2022. doi:10.1103/PhysRevB.106.165423. URL https://link.aps.org/doi/10.1103/PhysRevB.106.165423.

[156] Xiaolong Feng, Jiaojiao Zhu, Weikang Wu, and Shengyuan A. Yang. Two-dimensional topological semimetals*. *Chinese Physics B*, 30(10):107304, nov 2021. doi:10.1088/1674-1056/ac1f0c. URL https://dx.doi.org/10.1088/1674-1056/ac1f0c.

[157] H. C. Wu, L. Jin, and Z. Song. Nontrivial topological phase with a zero chern number. *Phys. Rev. B*, 102:035145, Jul 2020. doi:10.1103/PhysRevB.102.035145. URL https://link.aps.org/doi/10.1103/PhysRevB.102.035145.

[158] Marcos Atala, Monika Aidelsburger, Julio T. Barreiro, Dmitry Abanin, Takuya Kitagawa, Eugene Demler, and Immanuel Bloch. Direct measurement of the zak phase in topological bloch bands. *Nature Physics*, 9(12):795–800, Dec 2013. ISSN 1745-2481. doi:10.1038/nphys2790. URL https://doi.org/10.1038/nphys2790.

[159] P. Delplace, D. Ullmo, and G. Montambaux. Zak phase and the existence of edge states in graphene. *Phys. Rev. B*, 84:195452, Nov 2011. doi:10.1103/PhysRevB.84.195452. URL https://link.aps.org/doi/10.1103/PhysRevB.84.195452.

[160] Jan Carl Budich and Eddy Ardonne. Fractional topological phase in one-dimensional flat bands with nontrivial topology. *Phys. Rev. B*, 88:035139, Jul 2013. doi:10.1103/PhysRevB.88.035139. URL https://link.aps.org/doi/10.1103/PhysRevB.88.035139.

[161] Sujit Sarkar. Quantization of geometric phase with integer and fractional topological characterization in a quantum Ising chain with long-range interaction. *Scientific Reports*, 8(1):5864, Apr 2018. ISSN 2045-2322. doi:10.1038/s41598-018-24136-1. URL https://doi.org/10.1038/s41598-018-24136-1.

[162] Stefano Longhi. Zak phase of photons in optical waveguide lattices. *Opt. Lett.*, 38(19):3716–3719, Oct 2013. doi:10.1364/OL.38.003716. URL https://opg.optica.org/ol/abstract.cfm?URI=ol-38-19-3716.

[163] Junkai Dong, Vladimir Juričić, and Bitan Roy. Topolectric circuits: Theory and construction. *Phys. Rev. Res.*, 3:023056, Apr 2021.

doi:10.1103/PhysRevResearch.3.023056. URL https://link.aps.org/doi/10.1103/PhysRevResearch.3.023056.

[164] Gabriel Cáceres-Aravena, Bastián Real, Diego Guzmán-Silva, Alberto Amo, Luis E. F. Foa Torres, and Rodrigo A. Vicencio. Experimental observation of edge states in SSH-Stub photonic lattices. *Phys. Rev. Res.*, 4:013185, Mar 2022. doi:10.1103/PhysRevResearch.4.013185. URL https://link.aps.org/doi/10.1103/PhysRevResearch.4.013185.

[165] S. Longhi. Probing one-dimensional topological phases in waveguide lattices with broken chiral symmetry. *Opt. Lett.*, 43(19):4639–4642, Oct 2018. doi:10.1364/OL.43.004639. URL https://opg.optica.org/ol/abstract.cfm?URI=ol-43-19-4639.

[166] Alexander Szameit, Dominik Blömer, Jonas Burghoff, Thomas Schreiber, Thomas Pertsch, Stefan Nolte, Andreas Tünnermann, and Falk Lederer. Discrete nonlinear localization in femtosecond laser written waveguides in fused silica. *Opt. Express*, 13(26):10552–10557, Dec 2005. doi:10.1364/OPEX.13.010552. URL https://opg.optica.org/oe/abstract.cfm?URI=oe-13-26-10552.

[167] F. D. M. Haldane and S. Raghu. Possible realization of directional optical waveguides in photonic crystals with broken time-reversal symmetry. *Phys. Rev. Lett.*, 100:013904, Jan 2008. doi:10.1103/PhysRevLett.100.013904. URL https://link.aps.org/doi/10.1103/PhysRevLett.100.013904.

[168] Inbar Hotzen Grinberg, Mao Lin, Wladimir A. Benalcazar, Taylor L. Hughes, and Gaurav Bahl. Trapped state at a dislocation in a weak magnetomechanical topological insulator. *Phys. Rev. Appl.*, 14:064042, Dec 2020. doi:10.1103/PhysRevApplied.14.064042. URL https://link.aps.org/doi/10.1103/PhysRevApplied.14.064042.

[169] Inbar Hotzen Grinberg, Mao Lin, Cameron Harris, Wladimir A. Benalcazar, Christopher W. Peterson, Taylor L. Hughes, and Gaurav Bahl. Robust temporal pumping in a magneto-mechanical topological insulator. *Nature Communications*, 11(1):974, Feb 2020. ISSN 2041-1723. doi:10.1038/s41467-020-14804-0. URL https://doi.org/10.1038/s41467-020-14804-0.

[170] Christian Pauly. *Weak Topological Insulator*. Springer Fachmedien Wiesbaden, Wiesbaden, 2015. doi:10.1007/978-3-658-11811-2_5. URL https://link.springer.com/chapter/10.1007/978-3-658-11811-2_5.

[171] Ji Seop Oh, Tianyi Xu, Nikhil Dhale, Sheng Li, Chao Lei, Chiho Yoon, Wenhao Liu, Jianwei Huang, Hanlin Wu, Makoto Hashimoto, Donghui Lu, Chris Jozwiak, Aaron Bostwick, Eli Rotenberg, Chun Ning Lau, Bing Lv, Fan Zhang, Robert Birgeneau, and Ming Yi. Ideal weak topological insulator and protected helical saddle points, 2023.

[172] Jierui Huang, Tan Zhang, Sheng Xu, Zhicheng Rao, Jiajun Li, Junde Liu, Shunye Gao, Yaobo Huang, Wenliang Zhu, Tianlong Xia, Hongming Weng, and Tian Qian. Electronic structure of the weak topological insulator candidate Zintl

$Ba_3Cd_2Sb_4$. *Chinese Physics Letters*, 40(4):047101, mar 2023. doi:10.1088/0256-307X/40/4/047101. URL https://dx.doi.org/10.1088/0256-307X/40/4/047101.

[173] Ying Ran, Yi Zhang, and Ashvin Vishwanath. One-dimensional topologically protected modes in topological insulators with lattice dislocations. *Nature Physics*, 5(4):298–303, Apr 2009. ISSN 1745-2481. doi:10.1038/nphys1220. URL https://doi.org/10.1038/nphys1220.

[174] Peng Zhang, Ryo Noguchi, Kenta Kuroda, Chun Lin, Kaishu Kawaguchi, Koichiro Yaji, Ayumi Harasawa, Mikk Lippmaa, Simin Nie, Hongming Weng, V. Kandyba, A. Giampietri, A. Barinov, Qiang Li, G. D. Gu, Shik Shin, and Takeshi Kondo. Observation and control of the weak topological insulator state in $ZrTe_5$. *Nature Communications*, 12(1):406, Jan 2021. ISSN 2041-1723. doi:10.1038/s41467-020-20564-8. URL https://doi.org/10.1038/s41467-020-20564-8.

[175] Zongjian Fan, Qi-Feng Liang, Y. B. Chen, Shu-Hua Yao, and Jian Zhou. Transition between strong and weak topological insulator in $ZrTe_5$ and $HfTe_5$. *Scientific Reports*, 7(1):45667, Apr 2017. ISSN 2045-2322. doi:10.1038/srep45667. URL https://doi.org/10.1038/srep45667.

[176] Pallavi Malavi, Arpita Paul, Achintya Bera, D. V. S. Muthu, Kunjalata Majhi, P S Anil Kumar, Umesh V. Waghmare, A. K. Sood, and S. Karmakar. Pressure-induced superconductivity in the weak topological insulator BiSe. *Phys. Rev. B*, 107:024506, Jan 2023. doi:10.1103/PhysRevB.107.024506. URL https://link.aps.org/doi/10.1103/PhysRevB.107.024506.

[177] Xun-Jiang Luo, Xiao-Hong Pan, and Xin Liu. Higher-order topological superconductors based on weak topological insulators. *Phys. Rev. B*, 104:104510, Sep 2021. doi:10.1103/PhysRevB.104.104510. URL https://link.aps.org/doi/10.1103/PhysRevB.104.104510.

[178] Ryo Noguchi, T. Takahashi, K. Kuroda, M. Ochi, T. Shirasawa, M. Sakano, C. Bareille, M. Nakayama, M. D. Watson, K. Yaji, A. Harasawa, H. Iwasawa, P. Dudin, T. K. Kim, M. Hoesch, V. Kandyba, A. Giampietri, A. Barinov, S. Shin, R. Arita, T. Sasagawa, and Takeshi Kondo. A weak topological insulator state in quasi-one-dimensional bismuth iodide. *Nature*, 566(7745):518–522, Feb 2019. ISSN 1476-4687. doi:10.1038/s41586-019-0927-7. URL https://doi.org/10.1038/s41586-019-0927-7.

[179] Ankita Anirban. Quantum anomalous layer Hall effect. *Nature Reviews Physics*, 5(5):271–271, May 2023. ISSN 2522-5820. doi:10.1038/s42254-023-00585-0. URL https://doi.org/10.1038/s42254-023-00585-0.

[180] Half quantum spin Hall effect on the surface of weak topological insulators. *Physica E*, 44(5):906–911, 2012. ISSN 1386-9477. doi:https://doi.org/10.1016/j.physe.2011.11.005. URL https://www.sciencedirect.com/science/article/pii/S1386947711004000.

[181] Luojun Du, Tawfique Hasan, Andres Castellanos-Gomez, Gui-Bin Liu, Yugui Yao, Chun Ning Lau, and Zhipei Sun. Engineering symmetry breaking in 2D

layered materials. *Nature Reviews Physics*, 3(3):193–206, Mar 2021. ISSN 2522-5820. doi:10.1038/s42254-020-00276-0. URL https://doi.org/10.1038/s42254-020-00276-0.

[182] Inti Sodemann and Liang Fu. Quantum nonlinear hall effect induced by berry curvature dipole in time-reversal invariant materials. *Phys. Rev. Lett.*, 115:216806, Nov 2015. doi:10.1103/PhysRevLett.115.216806. URL https://link.aps.org/doi/10.1103/PhysRevLett.115.216806.

[183] Ritajit Kundu, H. A. Fertig, and Arijit Kundu. Broken symmetry and competing orders in Weyl semimetal interfaces. *Phys. Rev. B*, 107:L041402, Jan 2023. doi:10.1103/PhysRevB.107.L041402. URL https://link.aps.org/doi/10.1103/PhysRevB.107.L041402.

[184] A. A. Zyuzin, Si Wu, and A. A. Burkov. Weyl semimetal with broken time reversal and inversion symmetries. *Phys. Rev. B*, 85:165110, Apr 2012. doi:10.1103/PhysRevB.85.165110. URL https://link.aps.org/doi/10.1103/PhysRevB.85.165110.

[185] Minkyung Kim, Zubin Jacob, and Junsuk Rho. Recent advances in 2D, 3D and higher-order topological photonics. *Light: Science & Applications*, 9(1): 130, Jul 2020. ISSN 2047-7538. doi:10.1038/s41377-020-0331-y. URL https://doi.org/10.1038/s41377-020-0331-y.

[186] Max Geier, Ion Cosma Fulga, and Alexander Lau. Bulk-boundary-defect correspondence at disclinations in rotation-symmetric topological insulators and superconductors. *SciPost Physics*, 10(4), 2021. ISSN 2542-4653. doi:10.21468/SciPostPhys.10.4.092.

[187] Takashi Oka and Sota Kitamura. Floquet engineering of Quantum materials. *Annual Review of Condensed Matter Physics*, 10(1):387–408, 2019. doi:10.1146/annurev-conmatphys-031218-013423. URL https://doi.org/10.1146/annurev-conmatphys-031218-013423.

[188] Kai Yang, Shaoyi Xu, Longwen Zhou, Zhiyuan Zhao, Tianyu Xie, Zhe Ding, Wenchao Ma, Jiangbin Gong, Fazhan Shi, and Jiangfeng Du. Observation of Floquet topological phases with large Chern numbers. *Phys. Rev. B*, 106:184106, Nov 2022. doi:10.1103/PhysRevB.106.184106. URL https://link.aps.org/doi/10.1103/PhysRevB.106.184106.

[189] Netanel H. Lindner, Gil Refael, and Victor Galitski. Floquet topological insulator in semiconductor quantum wells. *Nature Physics*, 7(6):490–495, Jun 2011. ISSN 1745-2481. doi:10.1038/nphys1926. URL https://doi.org/10.1038/nphys1926.

[190] L. E. F. Foa Torres, P. M. Perez-Piskunow, C. A. Balseiro, and Gonzalo Usaj. Multiterminal conductance of a Floquet topological insulator. *Phys. Rev. Lett.*, 113:266801, Dec 2014. doi:10.1103/PhysRevLett.113.266801. URL https://link.aps.org/doi/10.1103/PhysRevLett.113.266801.

[191] Abhishek Kumar, M. Rodriguez-Vega, T. Pereg-Barnea, and B. Seradjeh. Linear response theory and optical conductivity of Floquet topological insulators. *Phys. Rev. B*, 101:174314, May 2020. doi:10.1103/PhysRevB.101.174314. URL https://link.aps.org/doi/10.1103/PhysRevB.101.174314.

[192] Immanuel Bloch. Ultracold quantum gases in optical lattices. *Nature Physics*, 1(1):23–30, Oct 2005. ISSN 1745-2481. doi:10.1038/nphys138. URL https://doi.org/10.1038/nphys138.

[193] Youngkuk Kim, C. L. Kane, E. J. Mele, and Andrew M. Rappe. Layered topological crystalline insulators. *Phys. Rev. Lett.*, 115:086802, Aug 2015. doi:10.1103/PhysRevLett.115.086802. URL https://link.aps.org/doi/10.1103/PhysRevLett.115.086802.

[194] YuTing Qian, ZhiYun Tan, Tan Zhang, JiaCheng Gao, ZhiJun Wang, Zhong Fang, Chen Fang, and HongMing Weng. Layer construction of topological crystalline insulator LaSbTe. *Science China Physics, Mechanics & Astronomy*, 63(10): 107011, May 2020. ISSN 1869-1927. doi:10.1007/s11433-019-1515-4. URL https://doi.org/10.1007/s11433-019-1515-4.

[195] Jin-Yu Zou and Bang-Gui Liu. Floquet Weyl fermions in three-dimensional stacked graphene systems irradiated by circularly polarized light. *Phys. Rev. B*, 93:205435, May 2016. doi:10.1103/PhysRevB.93.205435. URL https://link.aps.org/doi/10.1103/PhysRevB.93.205435.

[196] Konstantinos Ladovrechis and Ion Cosma Fulga. Anomalous Floquet topological crystalline insulators. *Phys. Rev. B*, 99:195426, May 2019. doi:10.1103/PhysRevB.99.195426. URL https://link.aps.org/doi/10.1103/PhysRevB.99.195426.

[197] Shang Liu, Tomi Ohtsuki, and Ryuichi Shindou. Effect of disorder in a three-dimensional layered Chern insulator. *Phys. Rev. Lett.*, 116:066401, Feb 2016. doi:10.1103/PhysRevLett.116.066401. URL https://link.aps.org/doi/10.1103/PhysRevLett.116.066401.

[198] A. A. Burkov and Leon Balents. Weyl semimetal in a topological insulator multilayer. *Phys. Rev. Lett.*, 107:127205, Sep 2011. doi:10.1103/PhysRevLett.107.127205. URL https://link.aps.org/doi/10.1103/PhysRevLett.107.127205.

[199] Aayushi Agrawal and Jayendra N Bandyopadhyay. Floquet topological phases with high chern numbers in a periodically driven extended Su-Schrieffer-Heeger model. *Journal of Physics: Condensed Matter*, 34(30):305401, may 2022. doi:10.1088/1361-648x/ac6eac. URL https://doi.org/10.1088/1361-648x/ac6eac.

[200] J. K. Asbóth, B. Tarasinski, and P. Delplace. Chiral symmetry and bulk-boundary correspondence in periodically driven one-dimensional systems. *Phys. Rev. B*, 90:125143, Sep 2014. doi:10.1103/PhysRevB.90.125143. URL https://link.aps.org/doi/10.1103/PhysRevB.90.125143.

[201] Takashi Oka and Hideo Aoki. Photovoltaic Hall effect in graphene. *Phys. Rev. B*, 79:081406, Feb 2009. doi:10.1103/PhysRevB.79.081406. URL https://link.aps.org/doi/10.1103/PhysRevB.79.081406.

[202] Arnob Kumar Ghosh, Ganesh C. Paul, and Arijit Saha. Higher order topological insulator via periodic driving. *Phys. Rev. B*, 101:235403, Jun 2020. doi:10.1103/PhysRevB.101.235403. URL https://link.aps.org/doi/10.1103/PhysRevB.101.235403.

[203] P. M. Perez-Piskunow, Gonzalo Usaj, C. A. Balseiro, and L. E. F. Foa Torres. Floquet chiral edge states in graphene. *Phys. Rev. B*, 89:121401, Mar 2014. doi:10.1103/PhysRevB.89.121401. URL https://link.aps.org/doi/10.1103/PhysRevB.89.121401.

[204] Qi Chen, Liang Du, and Gregory A. Fiete. Floquet band structure of a semi-Dirac system. *Phys. Rev. B*, 97:035422, Jan 2018. doi:10.1103/PhysRevB.97.035422. URL https://link.aps.org/doi/10.1103/PhysRevB.97.035422.

[205] Takuya Kitagawa, Takashi Oka, Arne Brataas, Liang Fu, and Eugene Demler. Transport properties of nonequilibrium systems under the application of light: Photoinduced quantum Hall insulators without Landau levels. *Phys. Rev. B*, 84:235108, Dec 2011. doi:10.1103/PhysRevB.84.235108. URL https://link.aps.org/doi/10.1103/PhysRevB.84.235108.

[206] P. M. Perez-Piskunow, L. E. F. Foa Torres, and Gonzalo Usaj. Hierarchy of Floquet gaps and edge states for driven honeycomb lattices. *Phys. Rev. A*, 91:043625, Apr 2015. doi:10.1103/PhysRevA.91.043625. URL https://link.aps.org/doi/10.1103/PhysRevA.91.043625.

[207] Shouyuan Huang and Xianfan Xu. Optical chirality detection using a topological insulator transistor. *Advanced Optical Materials*, 9(10):2002210, 2021. doi:https://doi.org/10.1002/adom.202002210. URL https://onlinelibrary.wiley.com/doi/abs/10.1002/adom.202002210.

[208] J. Karch, P. Olbrich, M. Schmalzbauer, C. Zoth, C. Brinsteiner, M. Fehrenbacher, U. Wurstbauer, M. M. Glazov, S. A. Tarasenko, E. L. Ivchenko, D. Weiss, J. Eroms, R. Yakimova, S. Lara-Avila, S. Kubatkin, and S. D. Ganichev. Dynamic Hall effect driven by circularly polarized light in a graphene layer. *Phys. Rev. Lett.*, 105:227402, Nov 2010. doi:10.1103/PhysRevLett.105.227402. URL https://link.aps.org/doi/10.1103/PhysRevLett.105.227402.

[209] Takafumi Hatano, Teruya Ishihara, Sergei G. Tikhodeev, and Nikolay A. Gippius. Transverse photovoltage induced by circularly polarized light. *Phys. Rev. Lett.*, 103:103906, Sep 2009. doi:10.1103/PhysRevLett.103.103906. URL https://link.aps.org/doi/10.1103/PhysRevLett.103.103906.

[210] M. Tahir and P. Vasilopoulos. Off-resonant polarized light-controlled thermoelectric transport in ultrathin topological insulators. *Phys. Rev. B*, 91:115311, Mar 2015. doi:10.1103/PhysRevB.91.115311. URL https://link.aps.org/doi/10.1103/PhysRevB.91.115311.

[211] Denitsa Baykusheva, Alexis Chacón, Jian Lu, Trevor P. Bailey, Jonathan A. Sobota, Hadas Soifer, Patrick S. Kirchmann, Costel Rotundu, Ctirad Uher, Tony F. Heinz, David A. Reis, and Shambhu Ghimire. All-optical probe of three-dimensional topological insulators based on high-harmonic generation by circularly polarized laser fields. *Nano Letters*, 21(21):8970–8978, Nov 2021. ISSN 1530-6984. doi:10.1021/acs.nanolett.1c02145. URL https://doi.org/10.1021/acs.nanolett.1c02145.

[212] Aayushi Agrawal and Jayendra N. Bandyopadhyay. Cataloging topological phases of N stacked Su-Schrieffer-Heeger chains by a systematic breaking of symmetries. *Phys. Rev. B*, 108:104101, Sep 2023. doi:10.1103/PhysRevB.108.104101. URL https://link.aps.org/doi/10.1103/PhysRevB.108.104101.

[213] Xiao-Liang Qi, Yong-Shi Wu, and Shou-Cheng Zhang. Topological quantization of the spin Hall effect in two-dimensional paramagnetic semiconductors. *Phys. Rev. B*, 74:085308, Aug 2006. doi:10.1103/PhysRevB.74.085308. URL https://link.aps.org/doi/10.1103/PhysRevB.74.085308.

[214] Yasuhiro Hatsugai, Takahiro Fukui, and Hideo Aoki. Topological analysis of the quantum hall effect in graphene: Dirac-fermi transition across van hove singularities and edge versus bulk quantum numbers. *Phys. Rev. B*, 74:205414, Nov 2006. doi:10.1103/PhysRevB.74.205414. URL https://link.aps.org/doi/10.1103/PhysRevB.74.205414.

[215] Shun-Li Yu, X. C. Xie, and Jian-Xin Li. Mott physics and topological phase transition in correlated dirac fermions. *Phys. Rev. Lett.*, 107:010401, Jun 2011. doi:10.1103/PhysRevLett.107.010401. URL https://link.aps.org/doi/10.1103/PhysRevLett.107.010401.

[216] A. H. Castro Neto, F. Guinea, N. M. R. Peres, K. S. Novoselov, and A. K. Geim. The electronic properties of graphene. *Rev. Mod. Phys.*, 81:109–162, Jan 2009. doi:10.1103/RevModPhys.81.109. URL https://link.aps.org/doi/10.1103/RevModPhys.81.109.

[217] Kai Sun, Hong Yao, Eduardo Fradkin, and Steven A. Kivelson. Topological insulators and nematic phases from spontaneous symmetry breaking in 2d fermi systems with a quadratic band crossing. *Phys. Rev. Lett.*, 103:046811, Jul 2009. doi:10.1103/PhysRevLett.103.046811. URL https://link.aps.org/doi/10.1103/PhysRevLett.103.046811.

[218] Mark S. Rudner, Netanel H. Lindner, Erez Berg, and Michael Levin. Anomalous edge states and the bulk-edge correspondence for periodically driven two-dimensional systems. *Phys. Rev. X*, 3:031005, Jul 2013. doi:10.1103/PhysRevX.3.031005. URL https://link.aps.org/doi/10.1103/PhysRevX.3.031005.

[219] Suman Aich and Babak Seradjeh. Real-space multifold degeneracy in graphene irradiated by twisted light, 2023.

List of Publications

In peer reviewed journals:

- *Floquet topological phases with high Chern numbers in a periodically driven extended Su–Schrieffer–Heeger model*,
  Aayushi Agrawal and Jayendra N. Bandyopadhyay, Journal of Physics: Condensed Matter **34**, 305401 (2022).

- *Cataloging topological phases of N stacked Su-Schrieffer-Heeger chains by a systematic breaking of symmetries*,
  Aayushi Agrawal and Jayendra N. Bandyopadhyay, Physical Review B, **108**, 104101 (2023).

- *Laser induced Floquet topological phases with high Chern number in a two-dimensional weak topological insulator*,
  Aayushi Agrawal and Jayendra N. Bandyopadhyay, arXiv:2312.02474.

Under preparation :

- *N stacked SSH model with elliptical polarized light*,
  Aayushi Agrawal and Jayendra N. Bandyopadhyay, (2023).

- *N stacked SSH model irradiated with twisted light*,
  Aayushi Agrawal and Jayendra N. Bandyopadhyay, (2023).

Biography of the Supervisor

Dr. Jayendra Nath Bandyopadhyay is a Professor in the Department of Physics at Birla Institute of Technology & Science Pilani, Pilani Campus. He did his Ph.D. in 2004 from Physical Research Laboratory (PRL), Ahmedabad, and the degree was awarded by Mohanlal Sukhadia University, Udaipur, Rajasthan. This was followed by postdoctoral research work for a year at PRL, two and a half years at Max Planck Institute for the Physics of Complex Systems, Dresden, Germany, and close to 4 years at the National University Singapore most of which was at the Centre for Quantum Technologies. Finally, he joined the Department of Physics, BITS Pilani, Pilani Campus, in July 2012. He has published several highly cited papers in reputed international journals. His research interests are Quantum Floquet Systems, Attosecond Physics, and Quantum Chaos.

Biography of the Co-Supervisor

Dr. Tapomoy Guha Sarkar is a Professor in the Department of Physics at Birla Institute of Technology & Science Pilani, Pilani Campus. He received his Ph.D. degree from IIT Kharagpur, in 2011. He joined the Physics Department of BITS Pilani, Pilani Campus, in June 2012 after a year's postdoctoral research at HRI, Allahabad. He has published several highly cited papers in reputed international journals. His research interests are theoretical cosmology, specializing in the study of the diffuse intergalactic medium through the Lyman alpha forest spectra and redshifted 21-cm signal. Recently, his interest develops into the domain of driven systems in condensed matter physics.

Biography of the Student

Ms. Aayushi Agrawal received her Master's Degree from Mohanlal Sukhadiya University, Udaipur in 2017. She cleared CSIR-UGC NET exam in 2017. She joined BITS-Pilani, as a research scholar in the Department of Physics in January 2018. Her PhD research area is the theoretical condensed matter physics. Her research interests are aligned in theoretical study of Floquet topological insulators. Specifically in her PhD thesis, she presented a theoretical study of quasi-1D topological insulators with an external periodic driving and observed intriguing topological properties which are absent in the static systems. She has published some papers in international journals and few are under review. She also presented her work in various national conferences.